UNIVERSITY OF NAPLES "FEDERICO II"

SCUOLA POLITECNICA E DELLE SCIENZE DI BASE

PhD program in

INDUSTRIAL PRODUCTS AND PROCESS ENGINEERING

DEPARTMENT OF CHEMICAL, MATERIALS AND PRODUCTION ENGINEERING

Tumoral bioengineered microtissues in microfluidic platforms to investigate on chip Colorectal cancer liver metastasis

SUPERVISOR

Prof. Paolo Antonio Netti, PhD

CO-SUPERVISOR

Eng. Giorgia Imparato, PhD

Eng. Raffaele Vecchione, PhD

Dr. Vincenza De Gregorio, PhD

CANDIDATE

Alessia La Rocca

ACADEMIC YEARS 2018-2022

Summary

Acronyms list (alphabetic order)

Abbreviations	Expanded form
αSMA	α Smooth Muscle Actin
µTs	Microtissues
5-FU	5-Fluorouracil
AA	Ascorbic Acid
CaCo-2	Human colorectal adenocarcinoma cell line
CAD	Collagen Assembly Degree Computer-aided design
CAF	Cancer-Associated Fibroblasts
CRC	Colorectal cancer
CRC µTs	3D co-cultured Colorectal Cancer microtissues
CRC $_{Day\ 0}$ µTs	HCT-116 cells/NF co-cultured at Day 0
CRC $_{Day\ 4}$ µTs	HCT-116 cells/NF obtained by seeding the HCT-116 cells on NF µTPs at Day 4
CRC $_{Day\ 8}$ µTs	HCT-116 cells/NF obtained by seeding the HCT-116 cells on NF µTPs at Day 8
3D CRC $_{Day\ 4}$ µTs $_{w\ AA}$	HCT-116 cells/NF obtained by seeding the HCT-116 cells on NF µTPs at Day 4 with Ascorbic Acid
3D CRC $_{Day\ 4}$ µTs $_{w/o\ AA}$	HCT-116 cells/NF obtained by seeding the HCT-116 cells on NF µTPs at Day 4 without Ascorbic Acid
CRLM	Colorectal cancer Liver Metastasis
CSC	Colorectal cancer stem cells
CTCs	Circulating Tumor Cells
CT-NE-Curc	Curcumin-loaded Nanoemulsions
DMEM	Dulbecco's Modified Eagle's Medium
ECM	Extracellular Matrix
EMEM	Eagle's Minimum Essential Medium
EMT	Epithelial-Mesenchymal Transition

FAPα	Fibroblast Activation Protein α
FBS	Fetal Bovine Serum
FFT	Fast Fourier transform
GFP	Green Fluorescent Protein
GPMs	Gelatin porous microbeads
$_{co}$HCC µTs	3D co-cultured HCC µTs
$_{mo}$HCC µTs	3D mono-cultured HCC µTs
HCC	Hepatocellular Carcinoma
HCC µTs	3D Human Primary Hepatocellular carcinoma poorly-differentiated microtissues
HCT-116	Human colorectal carcinoma cell line
HCT-116 µTs	3D mono-cultured Colorectal Cancer microtissues
HepG2	Hepatocellular carcinoma cell line
HepG2 µTs	3D Target Organ microtissue 3D Human Hepatocellular carcinoma differentiated microtissues
MET	Metastasis
MMP	Matrix Metalloproteinase
MOC	Multi-Organ-on-a-chip
MSD	Mean Squared Displacement
NF	Normal human dermal fibroblasts
NF µTs	3D Stroma microtissues
O/W NE	Oil in Water Nano-emulsions
O/W/O	Oil/Water/Oil
PAF	Paraformaldehyde
PBS	Phosphate buffered saline
PDMS	Polydimethylsiloxane

PMNs	Premetastatic niches”
ROI	Region of Interest
RT	Room Temperature
SHG	Second harmonic generation
TME	Tumor Microenvironment
YAP	Yes-associated protein

Abstract

Colorectal cancer (CRC) is the third most common tumor and the second leading cause of cancer-related deaths in developed countries with liver metastasis as the main cause of CRC mortality. Therefore, there is a growing need to understand the mechanisms underlying liver metastases to improve drug screening. Several phenomena, which occur in the Tumor microenvironment (TME), such as the extracellular matrix (ECM) remodeling, activation of the host cells, and Epithelial-Mesenchymal Transition (EMT), play a key role in cancer progression and metastatic process. While 2D *in vitro* models lack at all the TME providing an oversimplified view of tumor biology, on the other side the animal model also presents several limitations linked with the difficulty of growing a human tumor subcutaneously in mice and of replicating the initiation of the metastatic cascade. Recently, *in vitro* 3D models of CRC and liver, and multi-organ-on-a-chip, have become potential tools to reproduce *in vivo* conditions, in which it is possible to mimic the cross-talk between primary tumor and the distant metastatic growth in secondary site of the human body. However, these models often do not correctly recapitulate the complexity of the TME and the mechanisms underlying the metastasis that occurs in native tissue, owing to the use of exogenous matrix as native ECM's surrogate. To address this dearth, this thesis focuses on the fabrication of new 3D *in vitro* colorectal cancer microtissues (3D CRC µTs), which reproduce more faithfully the TME *in vitro*. Specifically, 3D CRC µTs were fabricated using a 2-step dynamic tissue engineering strategy. Firstly, normal human dermal fibroblasts (NF) were seeded on porous biodegradable gelatin microbeads (GPMs) – in which the cells were continuously induced to synthesize and assemble their own ECM – to fabricate a 3D Stroma microtissues (3D NF µTs). Secondly, Human colon cancer cells (HCT-116 cells) were dynamically seeded on 3D NF µTs to achieve 3D CRC µTs. Deeply morphological characterization of the 3D CRC µTs was performed to assess the presence of complex different macromolecular components featuring *in vivo*-ECM. The results showed 3D CRC µTs recapitulated the complexity of the TME in terms of ECM production, remodeling, cell growth, and bidirectional cross-talk between cancer cells and fibroblasts. Moreover, the activation of normal fibroblasts toward activated phenotype was assessed. Moreover, the microtissues were used to evaluate the synergistic effect of Curcumin-loaded nanoemulsions (CT-NE-Curc) and 5 Fluorouracil (5-FU). The results of the combination treatments of CT-NE-Curc and 5-FU showed a protective effect of curcumin on 3D NF µTs and enhanced cytotoxic effect on 3D CRC µTs. Then, multi-organ-on-a-chip platforms to investigate the hepatic metastasis from colorectal cancer were developed. A microfabrication strategy was used to design and fabricate a platform – in which primary tumor-like (3D CRC µTs) and target organ (3D liver microtissues named 3D HepG2 µTs) were respectively loaded in a dedicated chamber, to monitor the migration of cancer cells from the primary tumor site towards the target organ site. The metastasis-on-a-chip platforms experiments proved the bidirectional cross-talk between cancer cells and fibroblasts during the cancer invasion and migration both when 3D CRC µTs were loaded alone and when 3D CRC µTs together with 3D HepG2 µTs were housed into the corresponding chambers. Furthermore, we observed the presence of few cancer cells in the target organ chamber when 3D HepG2 µTs were present. In summary, the results described the high capability of 3D CRC µTs to reproduce the TME of colorectal cancer and to be capable to be used as models for drug and/or nutraceuticals testing. Moreover, these models may be used to further investigate the metastatic cascade through metastasis-on-a-chip platforms aiming at addressing further research questions in cancer investigation and drug discovery.

1. State of the art

1.1 Colorectal cancer liver metastasis (CRLM)

Colorectal cancer (CRC), malignant cancer that arises from the mucosa of the colon and rectum (Akhtar, Chandel et al. 2014), is one of the most common cancers in the worldwide, ranking third in terms of incidence (10.2% of all cancer cases worldwide), and the second most common cause of cancer mortality, immediately behind lung, liver, and stomach cancer (9.2% of all cancer mortality) (Kow 2019). In the last decades, there has been a significant improvement in the survival of patients with CRC since advancements in chemotherapy treatments, improvements in surgical techniques for CRC metastasis have crucially allowed bettering outcomes in treating this condition (Kow 2019). Genetic and epigenetic factors have great relevance for the disease. The majority of CRC are sporadic (75% of the patients have a negative history), can have a positive familial history (15 to 20% of patients with CRC) characterized by the hereditary syndrome of CRC, such as Lynch syndrome (Hereditary Nonpolyposis Colon cancer or HNPCC), which is caused by a mutation in one of the following deoxyribonucleic acid (DNA) repair genes, named Mismatch repair (MMR) genes: MLH1; MSH2; MSH6; PMS2, or EPCAM. Other risk factors of CRC are age (Over 90% of people diagnosed with colorectal cancer are over age 50), tobacco consumption (20–50%), gender (men have a slightly higher risk of developing colorectal cancer than women), alcohol consumption (20–50%), overweight and obesity (2–3% for every unit in body mass index), diabetes mellitus, and the consumption of red meat and processed foods (1.16 times for each 100 gm increase in the daily diet). Population-based studies have shown that around 25–30% of patients diagnosed with CRC develop distant metastases during their disease. Although important advances have been made for cancer treatment, metastasis is the major cause of cancer-related mortality, accounting for approximately 90% of global cancer deaths. Previous clinical data has shown that more than 50% of the patients with CRC develop metastasis in the liver (Valderrama-Trevino, Barrera-Mera et al. 2017). Indeed, the liver is the most common site of metastasis in patients with CRC due to its anatomical situation regarding the portal circulation (Fig. 1.1). Several crucial reasons induce the colon cancer cells to migrate and colonize the liver. The first is the presence of a complex network of blood vessels that transport oxygen and nutrient-enriched blood through the hepatic artery and the portal vein.

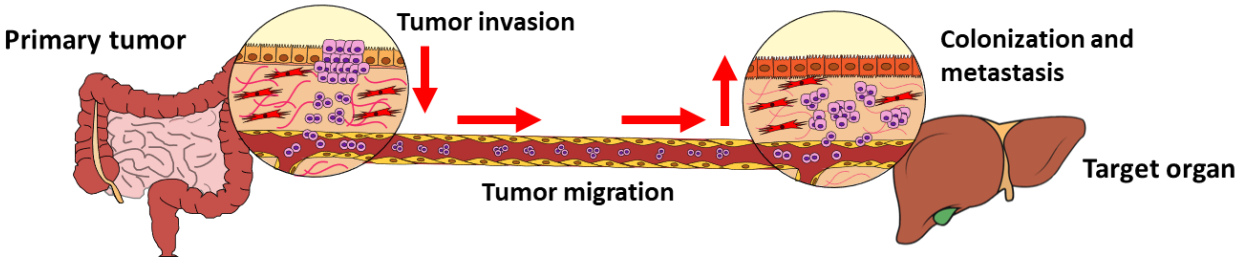

Figure 1.1 Schematic representation of Colorectal cancer liver metastasis.

Moreover, a slow hepatic microcirculation in the sinusoidal capillaries potentiates cancer cell retention in the liver. The second is the lack of the basement membrane of the hepatic endothelium, allowing cancer cells to interact easily with extracellular matrix proteins (ECM proteins) to establish micrometastases. Lastly, the surface molecules expressed by liver cells, including cell adhesion molecules, endocytic receptors, toll-like receptors, and oligosaccharides, can help the cancer cells migration from the lumen into the perisinusoidal space (or space of Disse) (Khazali, Clark et al. 2017). Recommended screening tests and standard treatments are needed to detect CRC that, if it is detected in the early stage, can be successfully treated. In addition, a multidisciplinary approach for the metastatic CRC has been fundamental in contributing to the improvement in OS (overall survival) of this disease, which depends on the presentation, number of sites and location of metastases, and potential for surgical resection. Currently, neoadjuvant chemotherapy agents, surgical resection followed by adjuvant chemotherapy is the gold standard treatment for colorectal liver metastases (CRLM), commonly known as the "Sandwich therapy" (Benson, Bekaii-Saab et al. 2013). But today there are more modifications to the treatment strategies for this disease. Recently, it is growing interest to investigate the interactions of cancer cells with the microenvironment in the liver parenchyma. Indeed, understanding the microenvironment in the liver parenchyma is extremely important to find the appropriate targets in preventing and treating metastatic disease in the case of CRLM (Kow 2019).

1.2 Metastasis and Tumor Microenvironment (TME)

To understand sufficiently the mechanisms underlying the CRLM, this section deals with the metastatic process and the key role of the TME. Metastasis is a dynamic and complex process that includes the cancer cells migration through different microenvironments, including stroma, blood vessel endothelium, the vascular system, and the tissue at a secondary site. This poorly understood process and its formation are inherently inefficient, in the sense that only a low percentage of cancer

cells (0.01% or less) that enter the circulation become metastatic cells and can complete the metastatic process (Massague and Obenauf 2016). When this process is successful, cancer usually becomes uncontrollable and incurable, and only in very early and localized stages the treatment is effective. Moreover, metastasis is a multifactorial process in which several genetic, epigenetic, and microenvironmental factors and signals derived from the tumor microenvironment (TME) induce the primary tumor cells to acquire the ability to migrate and establish themselves in distant organs. During metastasis, cancer cells undergo many driver mutations that allow them to develop a phenotypic selection capable of surviving all phases of the process, culminating in a metastatic phenotype. From these claims, it has become evident that TME has a pivotal role in modulating the aggressiveness, motility, dissemination, and colonization of cancer cells to distal organs. The TME is composed of different cell components such as T cells, macrophages, that interact with cancer cells and help them to overcome physical limits to disseminate the distant organs. In this direction, the metastasis can be described by a succession of individual steps (Fig. 1.2).

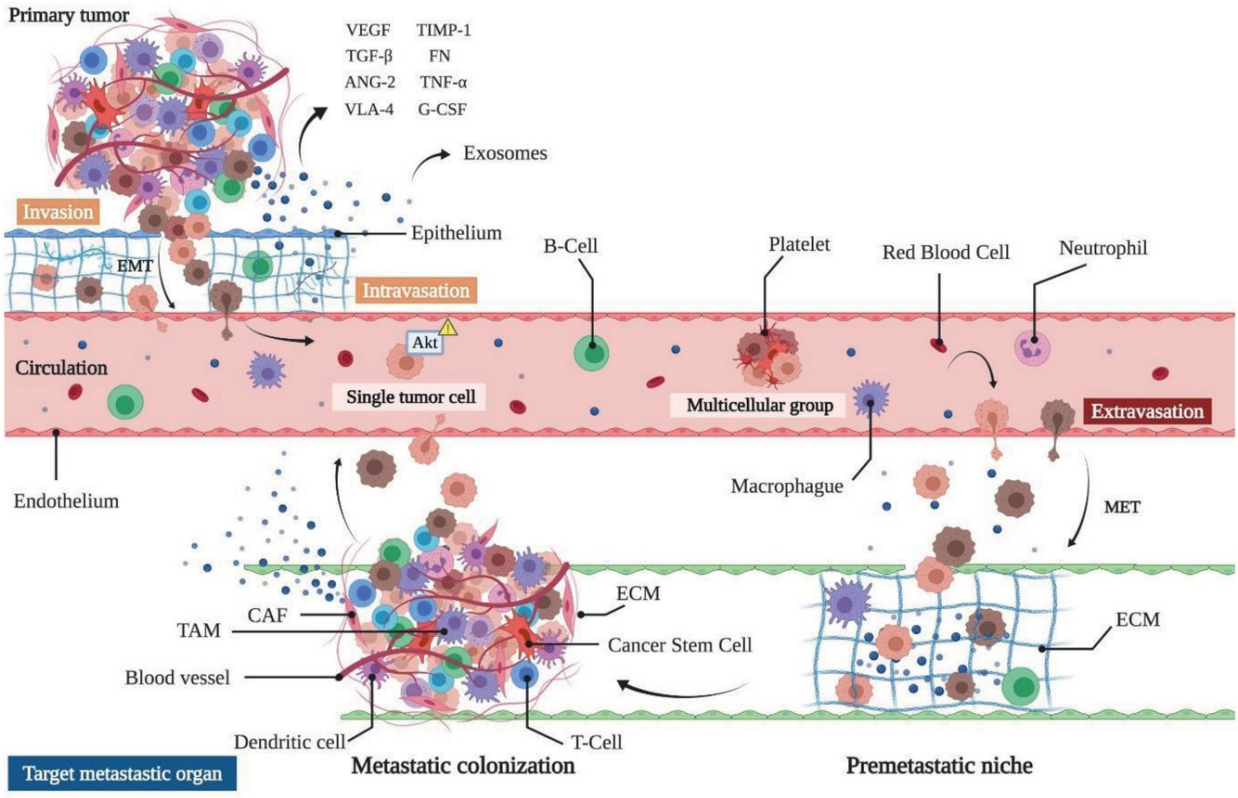

Figure 1.2 Graphic representation of the metastatic process (Ruiz-Espigares, Nieto et al. 2021)

The first step is the invasion of cancer cells of the primary tumor from the surrounding tumor to the adjacent normal stroma with the help of cancer-associated cells, such as cancer-associated fibroblasts (CAF), that secrete several factors that allow cancer cells to rupture the basement

membrane (BM) and to facilitate the invasion. During the invasion process, cancer cells acquire the ability to invade and migrate outside the primary tumor site thanks to Epithelial-Mesenchymal Transition (EMT) program. The EMT plays a key role in cancer processes, conferring epithelial-mesenchymal plasticity upon epithelial cells, both normal and neoplastic, which is crucial for invasion and metastatic spread, increasing mobility, invasiveness, and the ability to degrade the components of the ECM (Ribatti, Tamma et al. 2020). Interestingly, many studies support that a physical role for CAFs as leading cells at the front of the cancer cell collective migration exists. In detail, CAFs can contribute to the cancer cell collective migration by at least three mechanisms: (1) CAFs secreted factors can reprogram cancer cells, inducing epithelial/mesenchymal plasticity, which endows an invasive phenotype; (2) CAFs can exert mechanical forces on cancer cells that direct collective migration through the establishment of heterotypic cell-cell interactions. (3) CAFs can trigger structural modifications of the ECM, by generating ECM tracks or by applying mechanical pulling forces on ECM fibers that favor collective cancer cell invasion (Hurtado, Martinez-Pena et al. 2020) (Fig. 1.3).

The second step of the metastasis process is the intravasation of single cancer cells or cluster cells, designated as Circulating Tumor Cells (CTCs) to the blood and lymphatic vasculature of adjacent normal tissues to travel to distant sites. As animal models seem to suggest, CTCs exploit platelets and neutrophils to survive and form metastases. This seems to be one of the potential mechanisms which CTCs use to escape from the immune system, although shreds of evidence report that the success percentage in forming metastases is less than 0.01% (Ruiz-Espigares, Nieto et al. 2021). The last step of metastasis is the extravasation of CTCs into the distant tissue. This step is very critical and is affected by the microenvironment of the target organ which decides if the cancer cells colonization can occur. Much evidence suggests that a bidirectional cross-talk between primary tumor and target organ is found in which the exchange of factors secreted from both sites can convert the local microenvironment into compatible “premetastatic niches” (PMNs) (Liu, Zhang et al. 2017). The PMN is a tissue microenvironment that experiences a series of molecular and cellular changes to form the fertile “soil” for metastasis that is ready for the colonization of tumor cells, the “seeds” (Paget 1889). Once the target organ is ready to be seeded, cancer cells colonize it and undergo the Mesenchymal-Epithelial Transition process (MET) to acquire a sessile and proliferative phenotype (Ruiz-Espigares, Nieto et al. 2021).

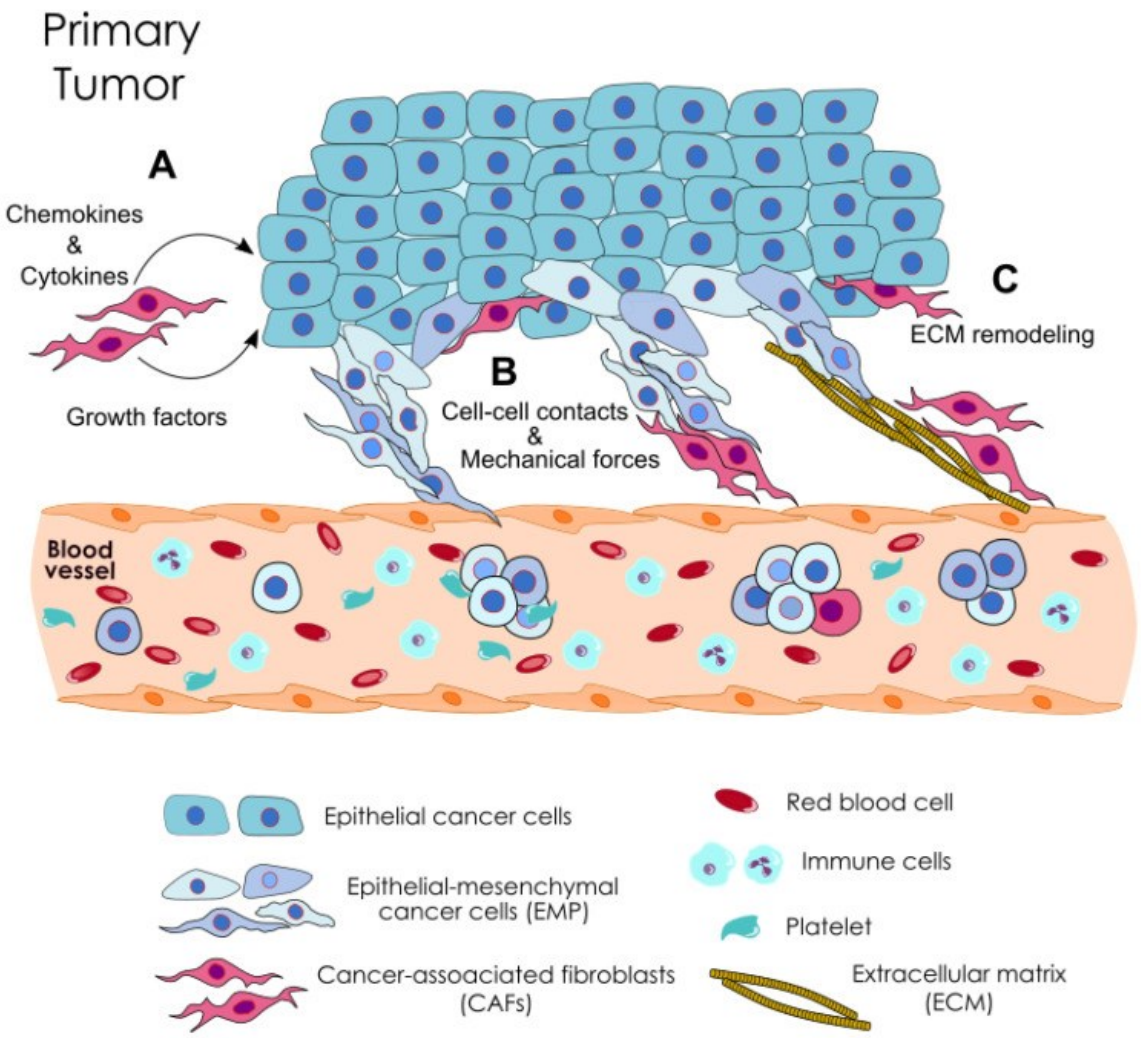

Figure 1.3 Role of the CAF on the invasion and migration of cancer cells (Hurtado, Martinez-Pena et al. 2020).

1.3 Activation of normal fibroblasts to CAFs in TME

Many therapeutic strategies for CRC treatment fail when the metastatic process exhibit quick progression, e.g. cancer cells become resistant to several chemotherapeutic agents. One of the major causes of failure of cancer therapies is the poor knowledge of many mechanisms that are present in TME. Therefore, among research groups is growing much interest in understanding all the phenomena underlying TME. In this context, one of the most important phenomena is the irreversibility transition from normal fibroblasts in CAFs and its frequency is correlated with the worse prognosis in patients affected by CRC. (Liu, Liu et al. 2016). This irreversibility transformation could be caused by a variety of inputs (Fig. 1.4).

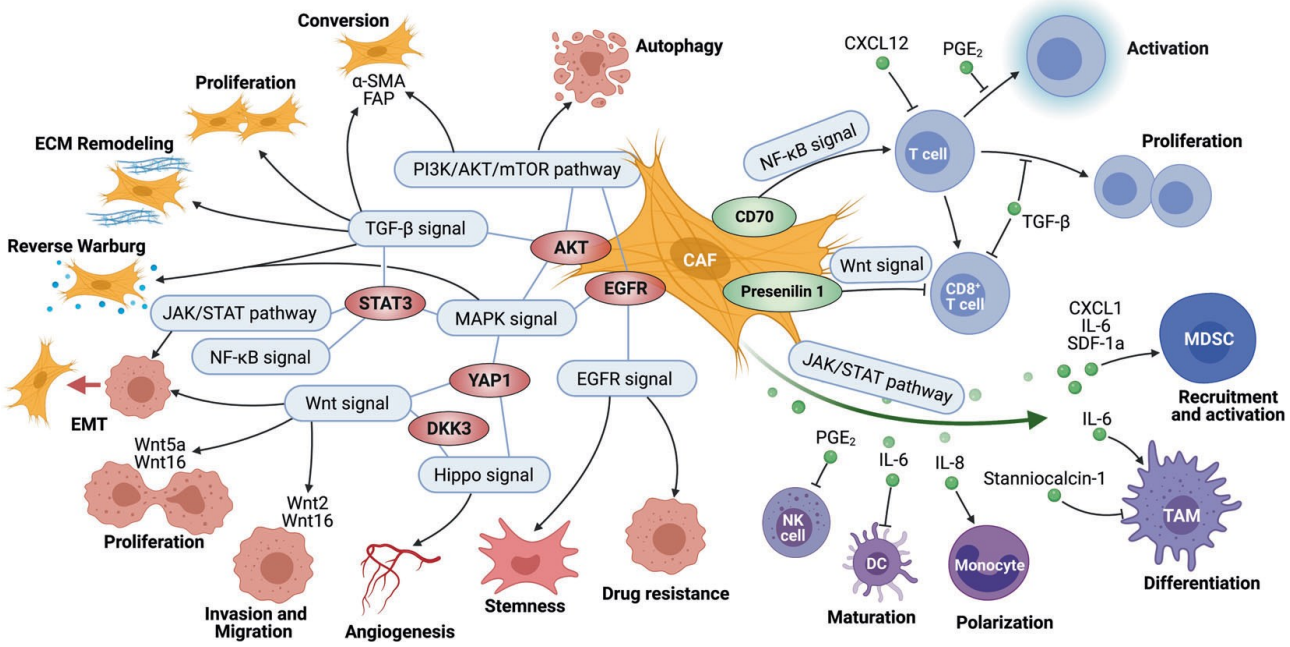

Figure 1.4 Crosstalk of different signaling pathways among CAFs, cancer cells, and immune cells (Wu, Yang et al. 2021).

First, many growth factors, cytokines and other factors signals – including Tumor Growth Factor-β1 (TGF-β1), osteopontin (OPN) and interleukin-1β (IL-1β), and others, released from cancer cells and/or immune cells in TME – can induce the activation of resident fibroblasts in CAFs by regulating the TGF-β and nuclear factor kappa-light-chain-enhancer of activated B cells (NF-κB) signaling pathways. In addition, much evidence has showed that exosomes also play a crucial role in promoting the transition of fibroblasts, acquiring new receptors or even genetic material from the cancer cells (Goulet, Bernard et al. 2018). Another way to induce the conversion of normal fibroblasts into CAFs is the shift in energy metabolism (such as aerobic glycolysis), which is potentially considered as a pivotal event in the conversion of normal fibroblasts into CAFs. In detail, cancer cells are able to promote the aerobic glycolysis of fibroblasts by activating the hypoxia-inducible factor-1α (HIF-1α) pathway; caveolin-1 (CAV-1) downregulation or cancer cell-derived mitochondrial transfer (Orang, Petersen et al. 2019). In recent years, many studies have demonstrated that the conversion of normal fibroblasts into CAFs is accompanied by changes in the self-expression of certain components, for example Yes-associated protein 1 (YAP1). The latter is a downstream transcriptional coactivator of the Hippo pathway and its abnormal expression causes malignant proliferation and metastasis, induces the EMT process and produces possible cancer drug resistance (Zhao, Wei et al. 2007). In addition, since YAP1 is active in cancer cells, it can regulate a variety of cancer genes or form complexes with them and then, jointly regulate the downstream

target genes. In detail, it has been proved that YAP-1 in normal fibroblast modulates the transcription of SRC by forming a protein compound with TEA domain transcription factor-1 (TEAD1), resulting in the activation of the cytoskeletal protein and, ultimately, the conversion into CAFs. In this respect, Shen et al. demonstrated that the expression level of YAP1 in the prostate cancer stroma was significantly higher than that in benign prostatic hyperplasia (BPH), and the amount of CAF in the prostate cancer stroma increased with the increase in the YAP1 expression level (Shen, Li et al. 2020). Therefore, all these mechanisms induced by cancer cells, other cellular and non-cellular components, and immune components of TME through direct and/or indirect physical interactions promote the activation of normal fibroblasts in CAFs. Differently from quiescent fibroblasts, CAFs experience enhanced proliferative and secretory capabilities, which contribute to ECM remodeling, autocrine activation, and immunomodulatory function. Indeed, CAFs are characterized by different markers that are expressed at low levels or not expressed in normal fibroblasts. Among these markers, the most commonly used to identify CAFs are α-smooth muscle actin (α-SMA), fibroblast activation protein (FAP), S100A4 (also known as fibroblast specific protein 1 or FSP1), platelet-derived growth factor receptor-α (PDGFR-α) and PDGFR-β (Wu, Yang et al. 2021). This variety of biological markers demonstrates that CAFs are a heterogeneous population of cells and they can be originated from several potential cellular precursors located in different organs/tissues. However, it is difficult to identify the cellular origins of CAFs because, currently, there is no available means to track the conversion between cell states directly or to collect longitudinal samples from the same lesion in human tissue. Mouse models with well-characterized disease progression have been created to shed light on the origin of CAFs (Luo, Young et al. 2018). Taken together, much evidence shows that the discovery of the heterogeneity of CAFs revealed a remarkably complex and diverse portrait.

1.4 The interaction of Nutraceuticals with Chemotherapy against cancer

Despite the development of new technologies and advanced clinical trials have improved drug discovery, cancer research continues to suffer from extremely low success rates in translating preclinical discoveries into clinical practice (Olgen 2018, Somarelli, Boddy et al. 2020). Many factors are responsible for the high failure rate, including a little understanding of the detailed mechanisms and elucidation of complicated intracellular processes of cancer, which are able to contribute more choices and strategies in the development of potent drugs with lower side effects. Indeed, cancer

cell growth, proliferation, apoptosis, invasion, survival and angiogenesis are major pathways in the development of anti-cancer drugs. Surgery and radiation therapy remain the common treatment modalities for local control of primary tumors while systemic therapy is mostly used to treat metastatic disease and as an essential adjuvant for some cancer types (Vodenkova, Buchler et al. 2020). Among chemotherapy drugs, 5-Fluorouracil (5-FU) is the most commonly used to treat different malignant tumors, including breast, pancreatic, skin, stomach, esophageal, and head and neck cancers. In CRC, intravenous and oral 5-FU or other fluoropyrimidines (FPs) have become the mainstay of systemic treatment since the 1990s. 5-FU is an antimetabolite drug that works by inhibiting essential biosynthetic processes, or by being incorporated into macromolecules, such as DNA and RNA, and inhibiting their normal function. In detail, 5-FU is an analogue of uracil with a fluorine atom at the C-5 position in place of hydrogen. It rapidly enters the cell using the same facilitated transport mechanism as uracil. 5-FU is converted intracellularly to several active metabolites: fluorodeoxyuridine monophosphate (FdUMP), fluorodeoxyuridine triphosphate (FdUTP) and fluorouridine triphosphate (FUTP) — these active metabolites disrupt RNA synthesis and the action of Thymidylate Synthase (TS), an enzyme that catalyzes the conversion of deoxyuridine monophosphate (dUMP) to deoxythymidine monophosphate (dTMP). The rate-limiting enzyme in 5-FU catabolism is dihydropyrimidine dehydrogenase (DPD), which converts 5-FU to dihydrofluorouracil (DHFU). More than 80% of administered 5-FU is normally catabolized primarily in the liver, where DPD is abundantly expressed (Fig. 1.5) (Longley, Harkin et al. 2003). 5-FU is widely used alone or in combination with other anticancer drugs for the treatment of CRC, However, the efficacy of 5-FU is severely limited in clinic application due to dose-limiting toxicity to the patients, including myelosuppression, gastrointestinal toxicity, cardiotoxicity, hepatotoxicity, neurotoxicity, ototoxicity, etc. (Liu, Huang et al. 2018) and development of multidrug resistance (MDR) in cancer cells, related to the overexpression of several molecules which take apart in many crucial signaling pathways, involved the cancer survival, proliferation and metastasis, e.g. nuclear transcription factor (NF-κβ) (Suetsugu, Mori et al. 2021). Moreover, accumulating evidence suggests that cancer recurrence is due to genetic and epigenetic alterations that are the result of complex interactions of transformed cells with their TME (Pin, Houle et al. 2011). Thus, there is growing

interest to investigate and identify the effective adjuvant strategies to reduce the chemotherapy-induced side effects and to suppress the crosstalk between cancer and stromal cells in the TME.

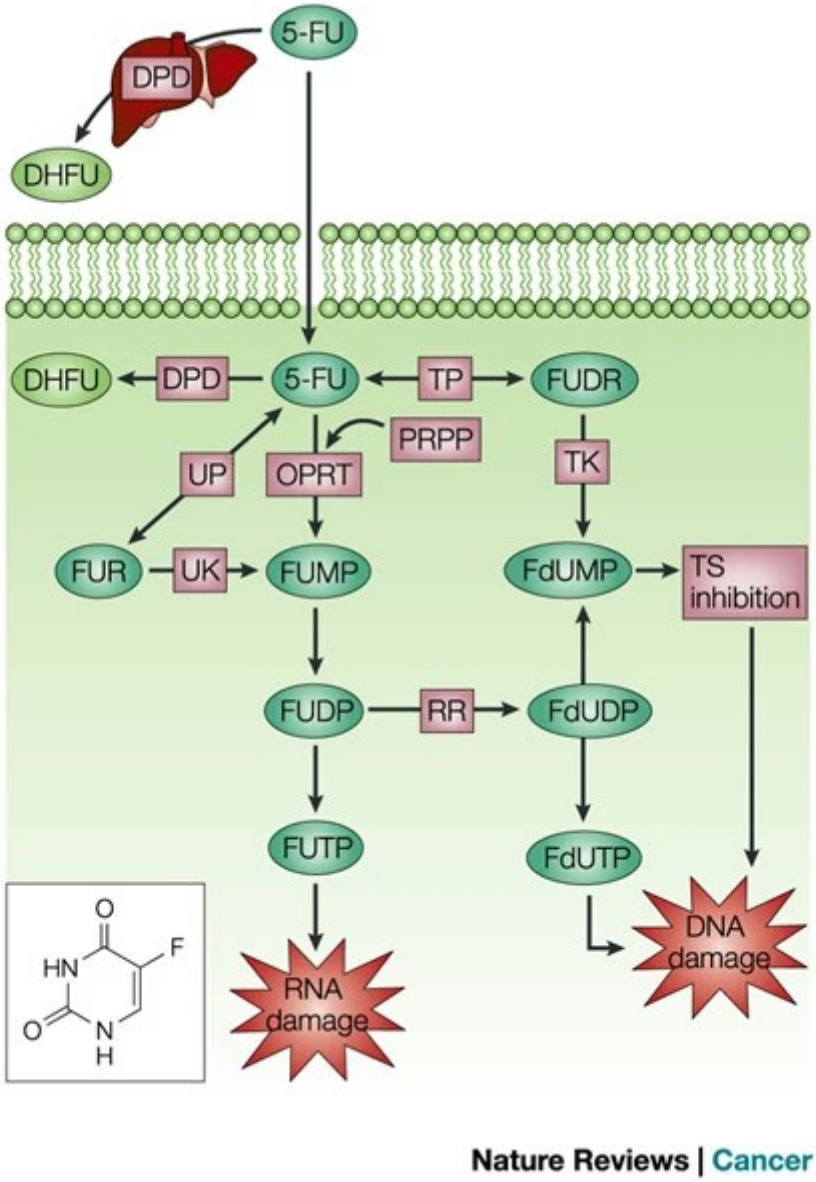

Figure 1.5 Mechanism of action of 5-FU (Longley, Harkin et al. 2003).

Natural compounds, or Nutraceuticals, offer themselves as ideal candidates to prevent and reduce the chemotherapy-induced side effects and modulate the TME, supporting chemotherapy. Curcumin is an active compound from the natural plant Curcuma longa, which has strong antioxidative, anti-microbial, anti-inflammatory, and anticancer activities. Growing evidence shows that curcumin is nontoxic in humans (10.1002/biof.1068), can prevent carcinogenesis, and enhances clinical efficacy of chemotherapy through sensitizing cancer cells to the commonly used chemotherapy, protecting the normal cells from chemotherapy-induced damages (Khurana, Jain et al. 2018). Recent studies have focused on the investigation of the mechanisms of action of curcumin.

Shakibaei et al. examine the chemosensitization potential of curcumin in 5-FU based chemotherapy in MMR-deficient and -proficient CRC cells: HCT116 (MMR-deficient, due to hypermethylation of MLH1 gene) and HCT116+ch3 (MMR-proficient, due to stable transfer of chromosome 3 bearing wild type copy of the MLH1 gene). They observed that the combination treatment with curcumin and 5-FU caused significantly more anti-proliferative effects and apoptosis in HCT116+ch3 and HCT116 cells compared to the individual drugs, demonstrating that curcumin sensitizes the 5-FU surviving CRC cells to treatment (Shakibaei, Mobasheri et al. 2013) (Fig. 1.6 a). Many efforts have demonstrated that curcumin is able to modulate the activity of various cell types within TME (Fu, He et al. 2021). In detail, Buhrmann et al. investigated the modulating effects of curcumin in combination with 5-FU, especially on CRC stem cells and EMT in an *in vitro* cancer microenvironment co-culture, composed of HCT116 cells and normal human fibroblast cells (MRC-5) which simulates the *in vivo* tumor microenvironment. In detail, HCT116 cells were placed on a nitrocellulose filter on top of a steel net bridge and the cells are nurtured by diffusion, whereas MRC-5 cells are grown in a monolayer on the bottom of the petri dish. They observed that these TME co-cultures supported the intensive crosstalk between cancer cells and fibroblasts, reproducing the up-regulation of metastatic active adhesion molecules (b1-integrin, ICAM-1), transforming growth factor-β signaling molecules (TGF-b3, p-Smad2), proliferation-associated proteins (cyclin D1, Ki-67), EMT factor (Vimentin, Slug up-regulated and E-Cadherin down-regulated) and CRC stem cells (CSC) factors (characterized by up-regulation of CD133, CD44, ALDH1) in HCT116 compared with mono-cultures of HCT-116 cells. Moreover, they observed that this synergistic crosstalk was even more pronounced in the presence of 5-FU, but dramatically decreased when the combinational treatment of curcumin and 5-FU was used, inducing biochemical changes to mesenchymal-epithelial transition (MET), thereby sensitizing CSCs to 5-FU treatment (Buhrmann, Kraehe et al. 2014) (Fig. 1.6 b). Despite promising results have been obtained, these *in vitro* models lacked an appropriate *in vitro* biocompatible microenvironment that can create and mimic a 3D in vivo TME. To overcome this limitation, Shakibaei et al. investigated the potentiation effects of curcumin on 5-FU against proliferation and metastasis of HCT116 cell and its corresponding isogenic 5-FU-chemoresistant cells (HCT116R) in a Three Dimensional (3D)-alginate tumor model.

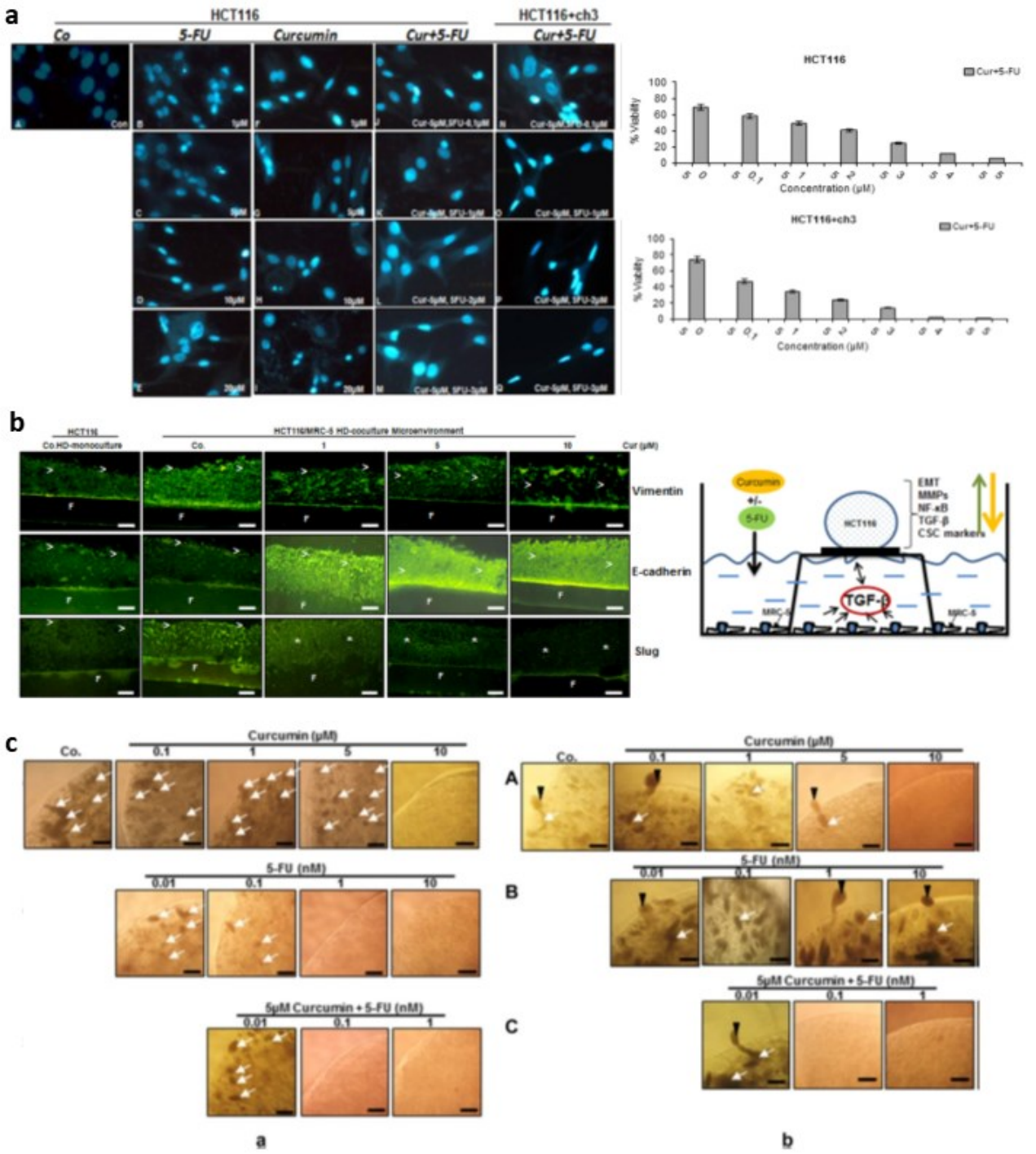

Figure 1.6 The combination treatment with Curcumin and 5-FU from *in vitro* 2D models to 3D models. Effect of curcumin and/or 5-FU on apoptosis, cell viability and proliferation in HCT116 and HCT116+ch3 colon cancer cells (a) (Shakibaei, Mobasheri et al. 2013); Effect of curcumin and/or 5-FU on EMT factors in *in vitro* TME co-cultures with CRC cells and fibroblasts, and schematic model of co-cultures (b) (Buhrmann, Kraehe et al. 2014); Curcumin increases 5-FU to block the proliferation and viability of HCT116 'a' and HCT116R 'b' cells cultured in alginate beads (c) (Shakibaei, Kraehe et al. 2015).

Such alginate-based 3D CRC model increased proliferation, vitality, and metastatic ability of Human Colon cancer cells (HCT116), reproducing the tumor microenvironment that mimics the *in vivo* situation. The authors observed that, in alginate, curcumin potentiated 5-FU-induced decreased capacity for proliferation, invasion and increased more sensitivity to 5-FU of HCT116R compared to the HCT116 cells. Their results demonstrated that the presence of curcumin made the CRC cells sensitive to 5-FU, at least in part by suppressing of NF-κβ signaling pathway, suggesting that the combination of curcumin and 5-FU may be useful to overcome 5-FU resistance in CRC patients (Shakibaei, Kraehe et al. 2015) (Fig. 1.6 c). Although the free form of curcumin can inhibit the survival of cancer cells, it has several limitations to be used as an effective complementary compound for the treatment of cancer: molecular instability, poor solubility in water, rapid conjugation to hydrophilic molecules (like glucuronic acid and sulphate) in the liver with biliary excretion and poor enteral absorption (Anand, Kunnumakkara et al. 2007). These limitations cause a low serum level of curcumin and fast clear of it following administration of it. This means that if a safe dose of curcumin is used, it may not maintain the sufficient concentration within the tumor to affect cancer cells effectively. To overcome these problems, scientists have developed new formulations of curcumin with high bioavailability and sufficient absorption by the intestine. Curcumin encapsulated in nanoparticles and other carriers such as liposomes, micelles, solid lipid nanoparticles, nanogel, have shown interesting results to increase bioavailability and abruption of curcumin. An example of nanocarriers, in which curcumin has been encapsulated, is 'oil in water nano-emulsions' (O/W NE). Recent studies have demonstrated that the curcumin-loaded food-grade nano-emulsions can control the interface properties and therefore the interaction with the intestinal barrier by easy deposition of functionalized biopolymers. Moreover, these formulations were high performed by adding a coating with thiol-modified chitosan, and it was demonstrated that they were able to load and protect curcumin from degradation and to enhance its bioavailability by using an *in vivo* model (Vecchione, Quagliariello et al. 2016). However, while *in vivo* studies provide a direct proof of the validity of a drug delivery system, appropriate *in vitro* studies are needed to specifically elucidate and investigate the mechanism of passage through the intestinal barrier. In this regard, Langella et al. investigated the route of these curcumin-loaded nanoemulsions and the biochemical effect of the nutraceutical release using an Air-Liquid Interface (ALI) of Caco2 cells in Transwell, as an *in vitro* testing platform. This platform allows the polarization and then, differentiation of Caco2 cells forming monolayers of mature intestinal enterocytes capable of reproducing *in vitro* the intestinal barrier to study intestinal drug absorption transport and toxicology. By using this model, the authors

demonstrated the interaction and the biosafety of these formulations – in terms of cell viability and tight junction integrity- as well as the curcumin bioavailability and its antioxidant effect on intestinal mucosa treated with Lipopolysaccharide (LPS). Taken together, the results suggested that these curcumin-loaded nanoemulsions are very promising tools for the effective release of unstable and poorly water-soluble drugs (Langella, Calcagno et al. 2018) (Fig. 1.7).

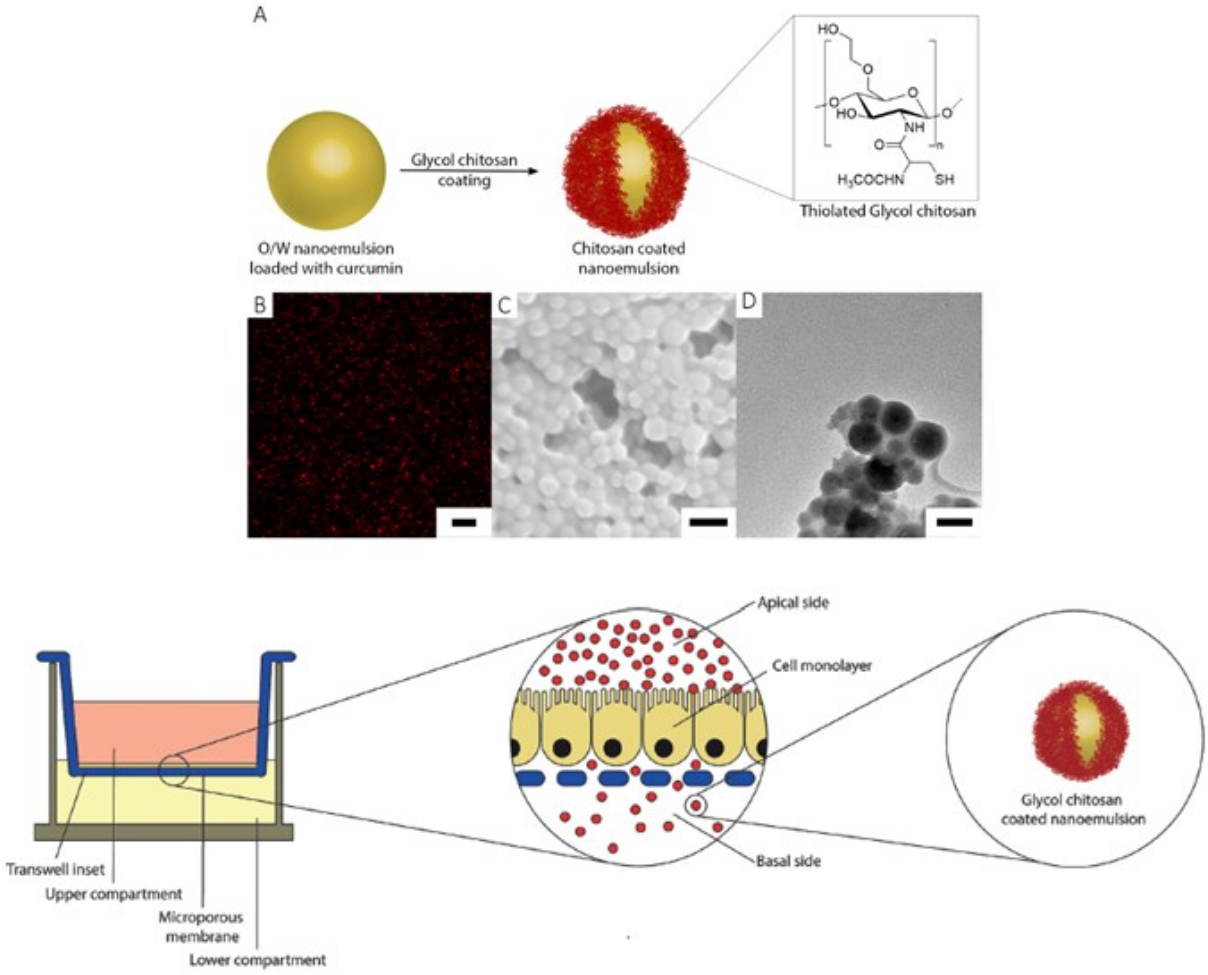

Figure 1.7 Enhanced bioavailability of curcumin using nanocarriers. Imaging characterization of O/W nanoemulsion loaded with Curcumin and schematic illustration of air-liquid interface of CaCo-2 equivalent epithelium in Transwell system treated with nanoemulsions (Langella, Calcagno et al. 2018).

Although the Caco2 cells in Transwell, as an *in vitro* testing platform, has been useful to explore the intestinal drug absorption transport of curcumin-loaded nanoemulsions, this model is not able to reproduce the complex 3D tissue microenvironment which plays a key role in regulating the drug uptake and diffusion and assessing drug toxicity/efficacy.

1.5 Three-dimensional (3D) *in vitro* tumor-on-a-chip models

Despite the extended research is being carried out to investigate the crucial phenomena underlying tumor growth and dissemination with a view to develop new anti-cancer drugs, the mechanisms of cancer and metastasis are still poorly understood. This is due to the lack of models that better mimic the cancer initiation and the TME, including the dynamic cross-talk between cancer cells with their microenvironment consisting of stromal and immune cells and ECM components (Wu and Swartz 2014). To obtain significant improvements in cancer therapy, it is needed to develop more advanced technologies that allow screening new anti-cancer drugs more efficiently and to a better understanding of the different steps of cancer progression (Esch, Bahinski et al. 2015). While on the one hand, *in vivo* models of cancer are very costly and are not accurately represent what happens in humans (Begley and Ellis 2012), on the other hand *in vitro* two- and three-dimensional (2D and 3D) cell models are not able to reproduce the complex spatial organization, the homotypic and heterotypic cell interactions that regulate the organ functions and, especially, the dynamic flow conditions generated by blood flow (Ehsan, Welch-Reardon et al. 2014). To overcome these limitations, 'organ-on-a-chip' technologies have been developed to reproduce the biological phenomena that depend on tissue microarchitecture and perfusion, as well as physiopathological processes (Bhatia and Ingber 2014) (Fig. 1.8). The integration of microfluidics, microfabrication, tissue engineering and biomaterials research makes this new technology capable of providing the basis for preclinical assays with greater predictive power and developing therapeutics for personalized medicine (Albanese, Lam et al. 2013). These systems are microfluidic platforms composed of optically clear plastic, glass, or flexible polymers, such as PDMS, which contain perfused hollow microchannels continuously perfused in which living cells are cultured to recreate *in vitro* structures and functions of tissues and organs. Several types of organ-on-a-chip platforms have been developed: the simplest systems, composed of a single microfluidic channel containing mono-cultured cells that simulate the functions of a tissue/organ, and more complex systems, compartmentalized chips or membrane chips-based systems, thus recreating interfaces between different tissues, such as an endothelial barrier, to investigate specific organ responses, including recruitment of circulating immune cells, by the drugs, toxins, or other environmental disturbances (Albanese, Lam et al. 2013) (Fig. 1.9). In addition, these devices are typically a few cm in size and made up of optically accessible plastic, glass, or flexible polymers which can incorporate hollow side chambers for the cyclic tensile strain to generate the stretch and relax the organotypic tissue

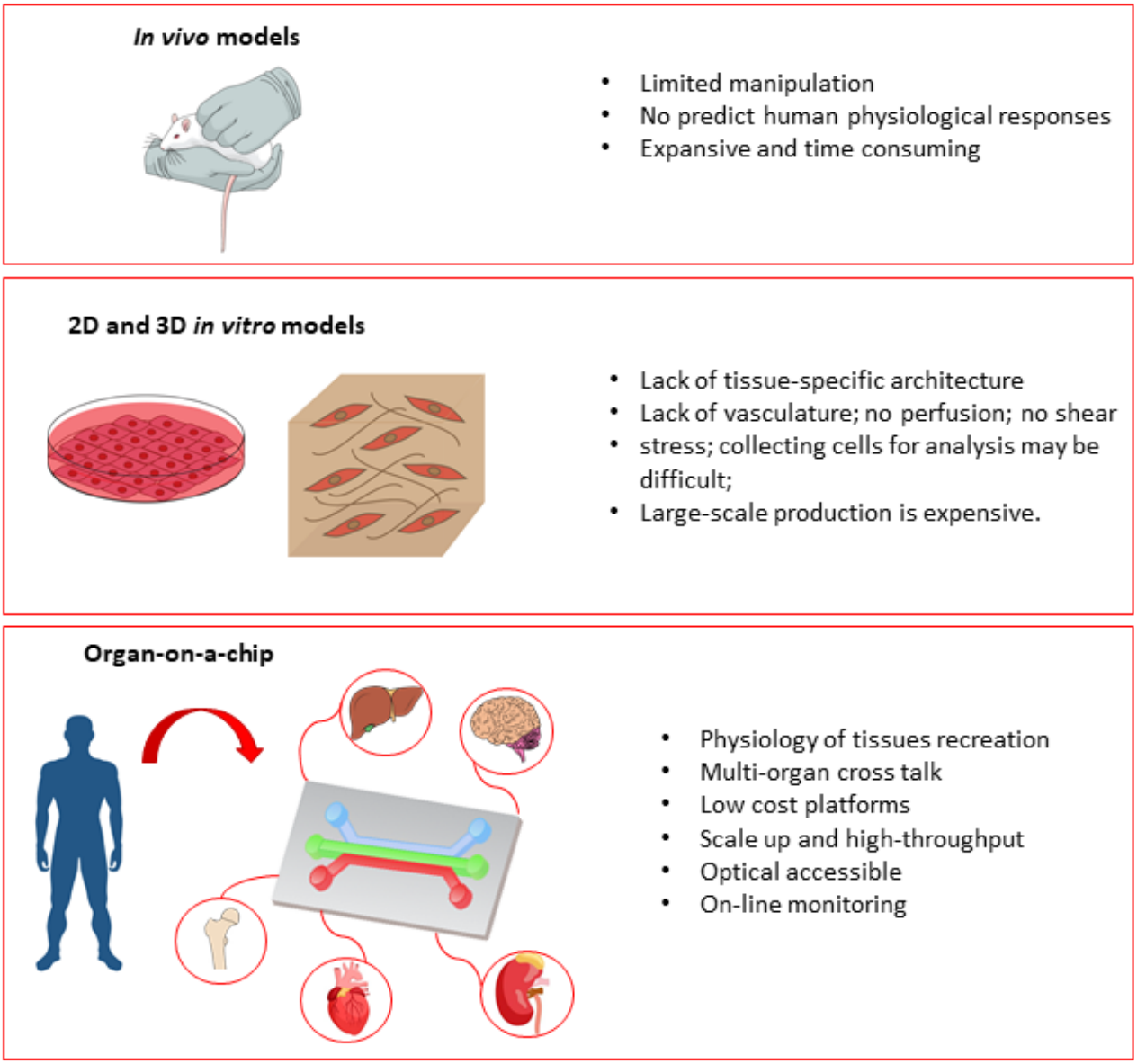

Figure 1.8 Schematic representation of *in vivo* and *in vitro* models.

interfaces, for example, mimicking lung epithelial stretch while breathing into a lung-on-a-chip device is crucial to obtaining a physiological inflammatory response (Huh, Matthews et al. 2010). In addition, different cell types are used in Organ-on-a-chip devices, including cell lines, primary cells from human donors, and human-induced pluripotent stem cells (hiPSCs), able to model and reproduce the functional tissue/organ. Hence, organ-on-a-chip platforms are potential tools to investigate and recapitulate the basic mechanisms and the complex structure of organ physiology and disease. Thanks to the evolution of these models, it has been possible to develop the 'tumor-on-a-chip' devices that reproduce *in vitro* the complexity of TME for the study of the tumor process (Sontheimer-Phelps, Hassell et al. 2019). Several tumor-on-a-chip devices often use cell lines for their easy handling, but they are not able to model the complexity of native tumors. To solve this

issue, PDX-tumor on-chip models, generated by the use of patient biopsies, represent more powerful models to reproduce the tumor (Huo, D'Arcangelo et al. 2020).

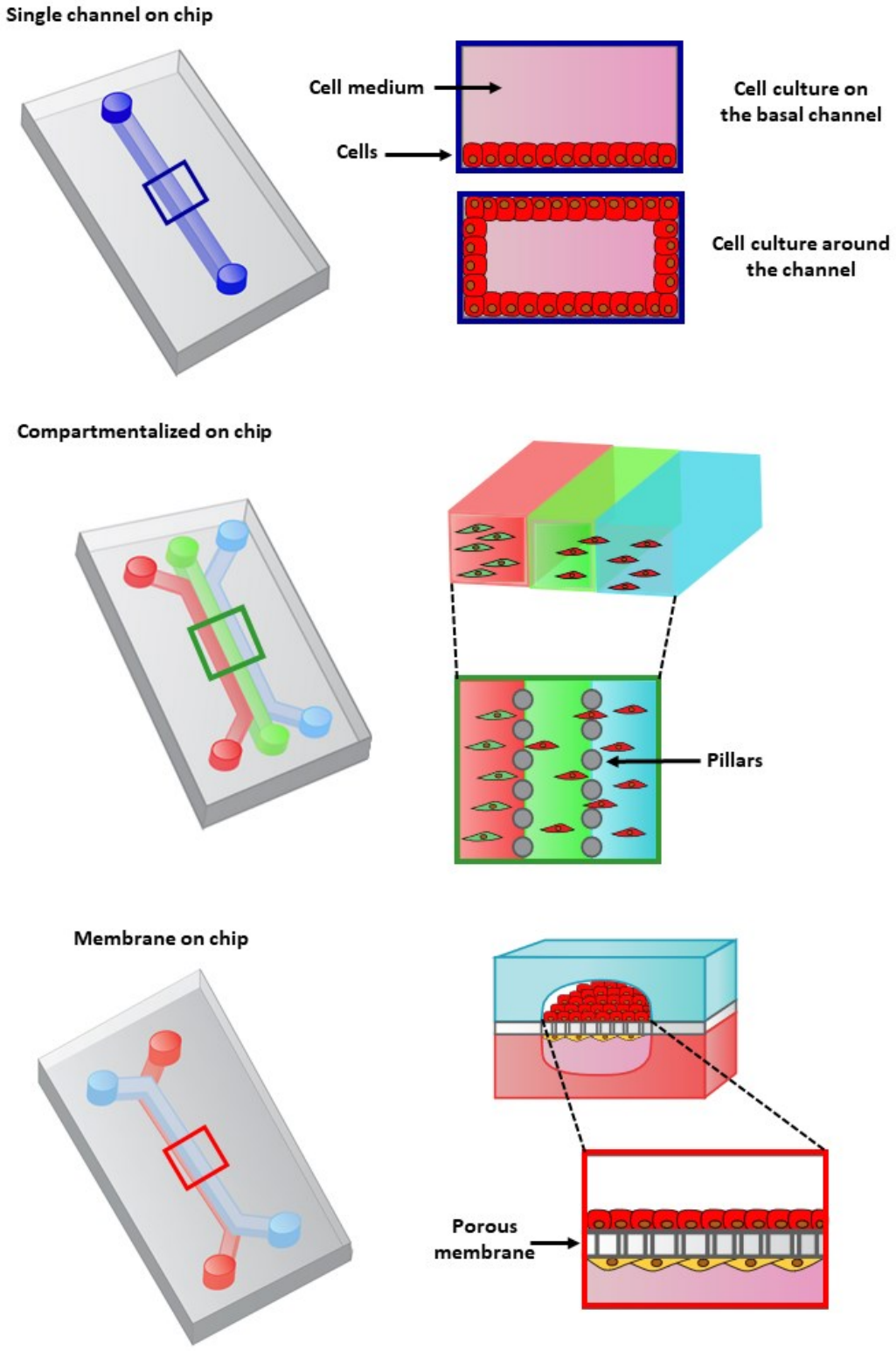

Figure 1.9 Schematic illustration of different types of organ-on-a-chip platforms.

Although the use of hiPSC is the most promising to mimic the functions and the complex structure of TME, the crucial limitation is the low efficiency of reprogramming cancer cells, suggesting that there only a minority of tumor cells could be successfully reprogrammed into pluripotent cancer cells (Gong, Yan et al. 2019). In recent years, several tumor-on-a-chip devices have been used for the study of the specific steps of the cancer cascade, such as growth and expansion of the tumor, angiogenesis, progression of lesions from early stage to late stage involving EMT, invasion, and metastasis of tumor cells (Ruiz-Espigares, Nieto et al. 2021). In detail, some of them are used to investigate the cancer-cell–ECM interactions during tumor growth and invasion, focusing on the role of the biophysical properties of ECM in guiding the pathological tumoral process. Indeed, many tumor-on-a-chip models have been developed to manipulate the TME with a view to studying the cell behavior under specific metabolic gradients conditions (Ayuso, Virumbrates-Munoz et al. 2019) or to study the changes of TME owing to CAF interaction and vice versa (Tsai, Trubelja et al. 2017). Moreover, several tumor-on-a-chip devices are often used to investigate the ECM components and remodeling. Indeed, thanks to their optical accessibility, different microscopy, and imaging techniques can be used, such as second harmonic generation (SHG), confocal reflectance microscopy, and immunofluorescence (Skardal, Devarasetty et al. 2016), allowing the simultaneous interrogation of ECM composition and structure. To investigate the bidirectional cross-talk between cancer cells and stromal cells in TME, compartmentalized tumor-on-a-chip models are potential tools for studying their communication during disease onset and progression (Imparato, Urciuolo et al. 2022). In detail, several compartmentalized tumor-on-a-chip models have been developed and they differ from each other for the use of a different ECM. Exogenous ECM-based compartmentalized tumor-on-a-chip devices include the use of injectable hydrogels, such as collagen I and Matrigel, used as 3D matrices to support cell growth and migration in microfluidic devices (Truong, Puleo et al. 2016). To investigate cancer-cell–ECM interactions in tumor-on-a-chip devices, many studies, on which hydrogels or hydrogel mixtures are more appropriate to reproduce the ECM *in vivo*, have been carried out (Anguiano, Castilla et al. 2017). In this aspect, Sung et al. developed a simple microfluidic 3D compartmentalized system, 'Y' shaped channel, in which mammary epithelial cells (MCF-DCIS) are co-cultured with human mammary fibroblasts (HMFs), which promotes a transition from (ductal carcinoma in situ) DCIS to (invasive ductal carcinoma) IDC *in vitro*. They demonstrated that the 1:1 mixed gel (Matrigel and collagen I) did support both cell types and the invasive transition (Sung, Yang et al. 2011) (Fig. 1.10 a).

Relevant research developed a compartmentalized microdevice to investigate the role of heterogeneous cancer cell subpopulations and of cancer fibroblasts in tumor progression and invasion correlated to ECM used. In this direction, Shin et al. developed an *in vitro* breast tumor model to mimic intratumor heterogeneity in a microfluidic system with ECM scaffolds. They co-cultured two different breast cancer cell types, highly invasive and aggressive breast cancer cells with the capacity of proteolytic ECM remodeling (MDAMB- 231) and non-aggressive, low-invasive phenotype and epithelial-like cancer cells (MCF-7). The ability of MDA-MB-231 to promote MCF-7 invasion in the heterogeneous tumor mass was strongly dependent on the ECM type. They observed that MCF-7 cells only follow the invasion path of MDA-MB-231 cells when grown in Matrigel, but not when grown in collagen I (Shin, Kim et al. 2013, Shin, Han et al. 2014) (Fig. 1.10 b). In another work, Noo Li Jeon et al. designed a microfluidic 3D cell culture platform to examine cancer-stromal cell interaction with a 3D ECM, composed of collagen and fibrin. This device consisted of an array of micro-posts that enabled straightforward micropatterning of the hydrogel which allowed flexible experimental configurations. They co-cultured SK-OV-3, MKN-74, and SW620 cancer cell lines, representing ovarian adenocarcinoma, stomach, and colorectal cancer, respectively, with normal human lung fibroblasts to explore the role of fibroblast in inducing morphological changes in cancer cells and how these changes are affected by the 3D ECM. The authors observed that fibroblasts induced marked morphological changes in all cancer cell types within 48 h in terms of increase in cytoplasmic volume and clustered nuclei. Moreover, they found differences between co-culture cell growth in collagen–fibrin mixed and in fibrin alone: strong morphological changes were observed using the collagen–fibrin mixed ECM, compared to the fibrin alone, indicating the synergistic effects of fibroblasts and ECM composition on cancer morphogenesis. The results underlined the key role of ECM structure and organization in promoting cancer cells proliferation and aggressiveness (Chung, Ahn et al. 2017) (Fig. 1.10 c). Another example of a compartmentalized device is that proposed by Huh and co-workers to replicate the early stages of breast cancer. They developed a co-culture of breast tumor spheroids with human mammary ductal epithelial cells and mammary fibroblasts, embedded in a mixture of Matrigel and fibronectin, in a compartmentalized 3D microfluidic device to replicate microarchitecture of breast ductal carcinoma in situ (DCIS). Prolonged culture in the microfluidic device resulted in the enlargement of spheroids, indicating the ability of the model to support the proliferation of DCIS cells. In addition, the authors explored the potential of this device as a drug screening platform by evaluating the efficacy and toxicity of an anticancer drug (paclitaxel). They observed that the growth of DCIS spheroids was inhibited

compared with the significantly increased tumor volume without the drug, and any toxic effects on the normal mammary epithelium (Choi, Hyun et al. 2015) (Fig. 1.10 d). A similar compartmentalized tumor-on-a-chip platform was proposed by Ingber et al. who developed *in vitro* human orthotopic models of non-small-cell lung cancer (NSCLC) that recapitulate organ microenvironment-specific cancer growth, tumor dormancy, and responses to tyrosine kinase inhibitor (TKI) therapy observed in human patients *in vivo*. They demonstrated that the rapid growth of NSCLC cells was correlated with some specific local microenvironmental factors produced by normal lung epithelial and endothelial cells put in contact across a porous ECM- coated synthetic membrane. Differently, the same cancer cells were not able to grow if cultured in 2D conditions with the same medium (Hassell, Goyal et al. 2017) (Fig. 1.10 e).

Some compartmentalized tumor-on-a-chip devices use decellularized extracellular matrices to mimic the properties and functions of organ-specific ECM. Indeed, Yi and co-workers produced a tumor-on-a-chip platform for recapitulating the pathological features of glioblastoma (GBM), combining a compartmentalized cancer-stroma structure, an oxygen-gradient-generating system and brain decellularized ECM (BdECM) (Yi, Jeong et al. 2019). This microfluidic system is composed of innermost cancer cells, surrounding vascular endothelial cells, and an outermost chamber filled with culture medium. The tumor tissue was surrounded by microvessels to induce the formation of central hypoxia because the device was composed of selectively gas-permeable parts. They observed not only the GBM-on-a-chip device developed various pathological features of GBM, but also a high level of SOX2, a marker for neural stem cells implicated in the maintenance of cancer stem cells and therapeutic resistance of cancer cells. In addition, they also observed that the cells proliferated faster in BdECM than within collagen gel. Further, glioblastoma cells in BdECM showed also different drug sensitivities, compared to cells within collagen gel (Fig. 1.10 f).

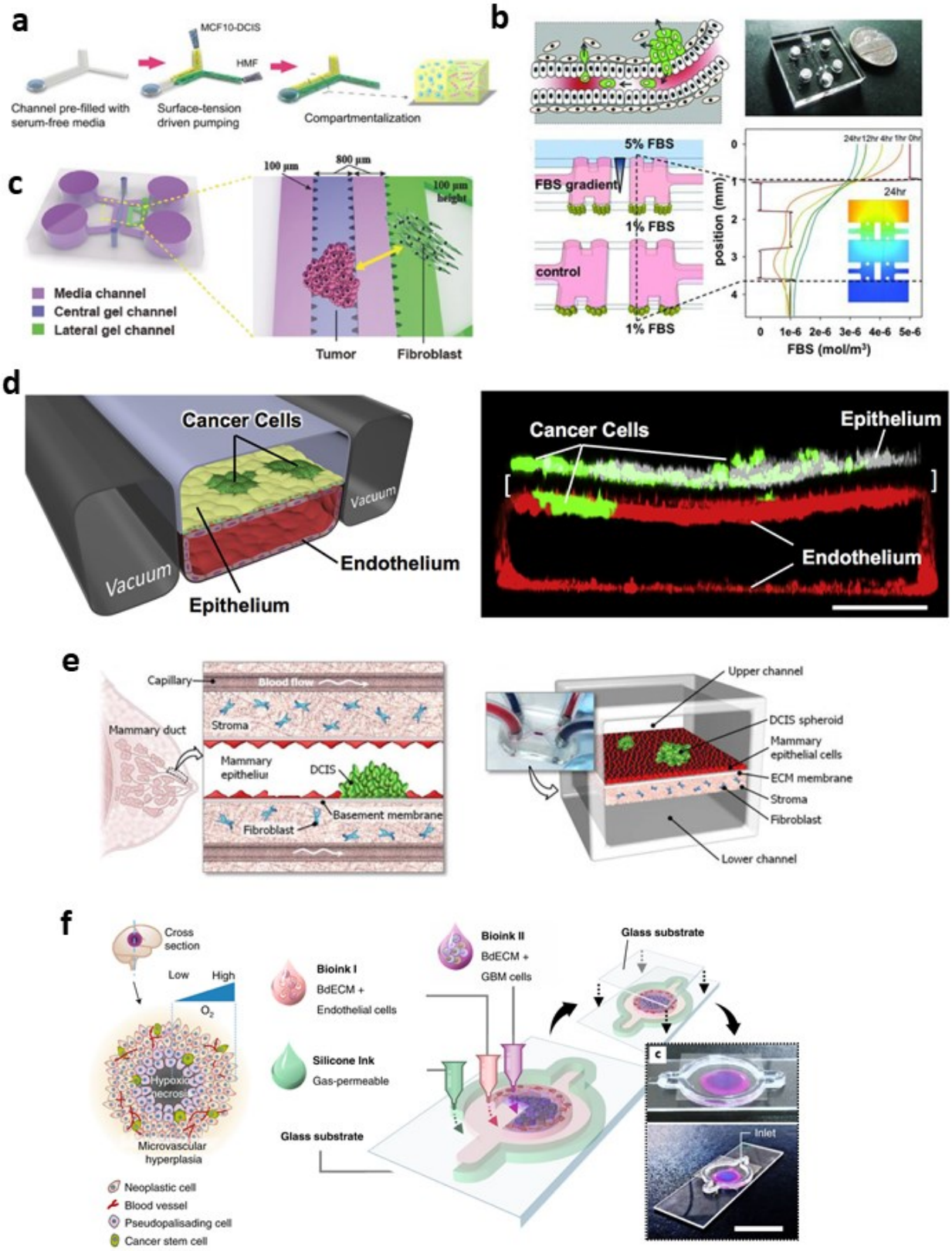

Figure 1.10 Exogenous ECM-based compartmentalized tumor-on-a-chip devices. Schematic illustration of 3D compartmentalization and the invasive transition of MCF-DCIS cells (a) (Sung, Yang et al. 2011). Schematic depiction of microfluidic device and simulation of diffusion of 67KDa of serum albumin protein gradient in 5% FBS through the hydrogel scaffolds to compare MDA-MB-231

and MCF-7 cells phenotypes (b) (Shin, Kim et al. 2013, Shin, Han et al. 2014); Schematic of microfluidic device and coculture experiment to examine tumor-stromal interactions (c) (Chung, Ahn et al. 2017); Human Orthotopic Lung Cancer-on-a-Chip Models (d) (Hassell, Goyal et al. 2017); Schematic depiction of DCIS reproduced in the breast cancer-on-a-chip microdevice (e) (Choi, Hyun et al. 2015); Schematic illustration of a cross-sectional view of a native GBM and the process for printing with various bioinks and other materials to construct a compartmentalized structure (Yi, Jeong et al. 2019) (f).

Despite the results obtained by these exogenous ECM-based compartmentalized are very promising, they barely reproduce the complex molecular composition of the native ECM. An alternative to these models, several endogenous ECM-based compartmentalized tumor-on-a-chip devices have been developed to reproduce specific human ECM *in vitro*, inducing the cells to produce their own ECM composition and organization. In this perspective, Gioiella et al. (Gioiella, Urciuolo et al. 2016) developed breast cancer models in which cells are embedded in their own ECM tissue. Different from the previously mentioned works in which cells are embedded in a 3D exogenous matrix, in this work 3D stromal tissue consisted of engineered tissue micromodules formed by fibroblast-assembled ECM. Previous works demonstrated that these engineered tissue micromodules mimic the tumor physiology *in vitro* including functional and morphological changes (Brancato, Comunanza et al. 2017, Brancato, Gioiella et al. 2018). These micromodules were integrated into the tumor-on-a-chip device to replicate the interactions of breast cancer cells with stromal cells as well as ECM activation during tumor progression. The authors fabricated an optically accessible microfluidic device, composed of two compartments for hosting stromal tissue and epithelial tumor, separated by pillars, replicating the tissue–tissue interface. The results showed that the stroma tissue was activated both at the cellular level and the ECM level: activation of normal fibroblasts and overexpression of some no-cellular components of ECM (fibronectin and hyaluronic acid) (1.11 a). Moreover, analysis of collagen fiber remodeling showed a change from collagen fibers orderly organized, which featured healthy stromal tissue, toward thick, coarser, and randomly orientated collagen fibers, as showed in human tumor biopsies (Despotovic, Milkcvic et al. 2020). Moreover, the authors studied the diffusivity and trafficking of macromolecules within the stromal compartment. It is known that diffusivity represents one of the key factors affecting drug delivery in biological tissues. Thus, the authors monitored in real time the Fluorescein isothiocyanate (FITC)-dextran diffusion coefficient, combining multiphoton and fluorescence recovery after photobleaching (FRAP) technique (1.11 b). They observed a significantly lower diffusion coefficient for the activated stroma, compared to the healthy one, hypothesizing that this result was correlated with the increased interaction between dextran and the ECM because of coarser collagen fibers,

suggesting that anticancer drugs relying on diffusion to reach cancer tissue might have poor penetration and limited therapeutic efficacy.

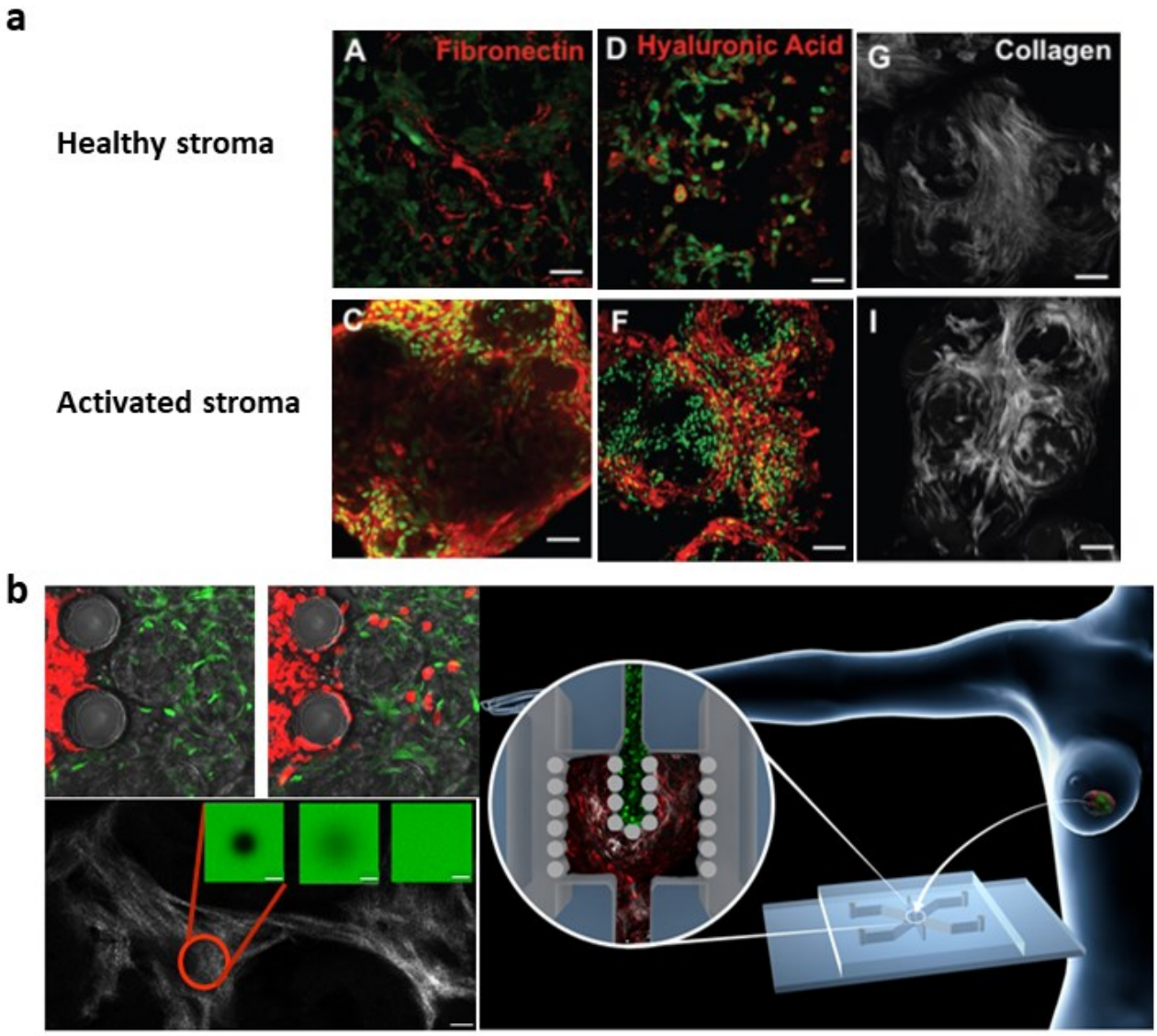

Figure 1.11 Endogenous ECM Compartmentalized tumor-on-a-chip device. ECM components overexpression in the activated stroma (a); Schematic representation of Engineered Breast cancer model on a chip, confocal images of cancer cells invasion into the healthy stroma and SHG and FRAP techniques to investigate transport properties (b) (Gioiella, Urciuolo et al. 2016).

1.6 Existing models for studying colorectal cancer liver metastasis

1.6.1 *In vitro* 3D colorectal cancer models

It is widely accepted that ECM remodeling is the key component of TME and the bidirectional cross-talk between CRC cells and stromal components, having a key role in cancer progression and metastatic process. Current *in vivo* models and *in vitro* 2D cell culture models do not faithfully reproduce the complex interaction between cancer cells and ECM. Instead, human resected tumors implanted in immunocompromised mice, named Patient-Derived Xenograft (PDX) models, are clinically relevant to better reproduce the TME, maintaining a high degree of genomic complexity. However, they present a low grafting rate, and the site and frequency of PDX CRC may vary from that seen in the patient. In recent years, *in vitro* 3D CRC models have been developed to closely mimic the complexity of human cancer tissues. 3D cell culture models have also been used to investigate cell-cell and cell-ECM interactions that occur in the TME of CRC. In this direction, Rios de la Rosa et al. described a novel approach of modeling and biofabricating the early stage of CRC and its TME, comparing it with the gold standard *in vitro* models, Tissue Culture Plastic (TCP) monolayer cells and 3D spheroids, respectively. In this work, the human colorectal cancer cell line, HCT-116, was encapsulated in an alginate solution to produce the *in vitro* 3D CRC model. Their approach allowed better control of the alginate beads dimension and the number of HCT-116 cells, to compare the two 3D *in vitro* models and to address the generation of early-stage models for CRC, where angiogenesis and stromal response are not yet involved. They observed that encapsulated HCT-116 demonstrated high viability, increase in stem-like cell populations (increased expression of CD44), and reduced hypoxic regions (lower HIF-1a expression) compared to spheroid cultures (de la Rosa, Wubetu et al. 2018) (Fig. 1.12 a). More complex *in vitro* 3D co-culture models of CRC were used to prove the interactions of the cancer-stromal cells. As it is reported in the literature, the fibroblasts were considered the major drivers of the tumor development, progression, and induction of metastasis due to the secretion of several molecules that mediate this crosstalk (Fig. 1.12 a). In this direction, Cattin et al. reported a 3D matrigel-based spheroid of CRC *in vitro* to investigate multicellular interactions between CRC cell lines (SW620 and HCT116) and tumor microenvironment cell types (fibroblasts and endothelial cells). Their model demonstrated that fibroblasts induced cancer cell motility and invasion through interaction between fibroblasts surface-associated-FGF-2 and -FGFR on cancer cells, activating Src family kinase, as shown *in vivo* (Fig. 1.12 b) (Cattin, Ramont et al. 2018). In addition, it has been previously demonstrated normal fibroblasts seem to be attracted into tumor sites by cancer cells; when fibroblasts remain in the TME

become activated fibroblasts, or named CAF, in response to cancer cell signaling. In this context, Park et al. developed a scaffold-free coculture spheroid model of colonic adenocarcinoma cells (CACs) and normal colonic fibroblasts (NCFs). They proved the co-culture of CACs and NCFs resulted in synergistic effects on CAC and NCF spheroid formation, in which NCFs acquired characteristics that resembled those of CAFs, with the expression of the Fibroblast Activated Protein α (FAP α) (Fig. 1.12 c) (Park, Lee et al. 2016).

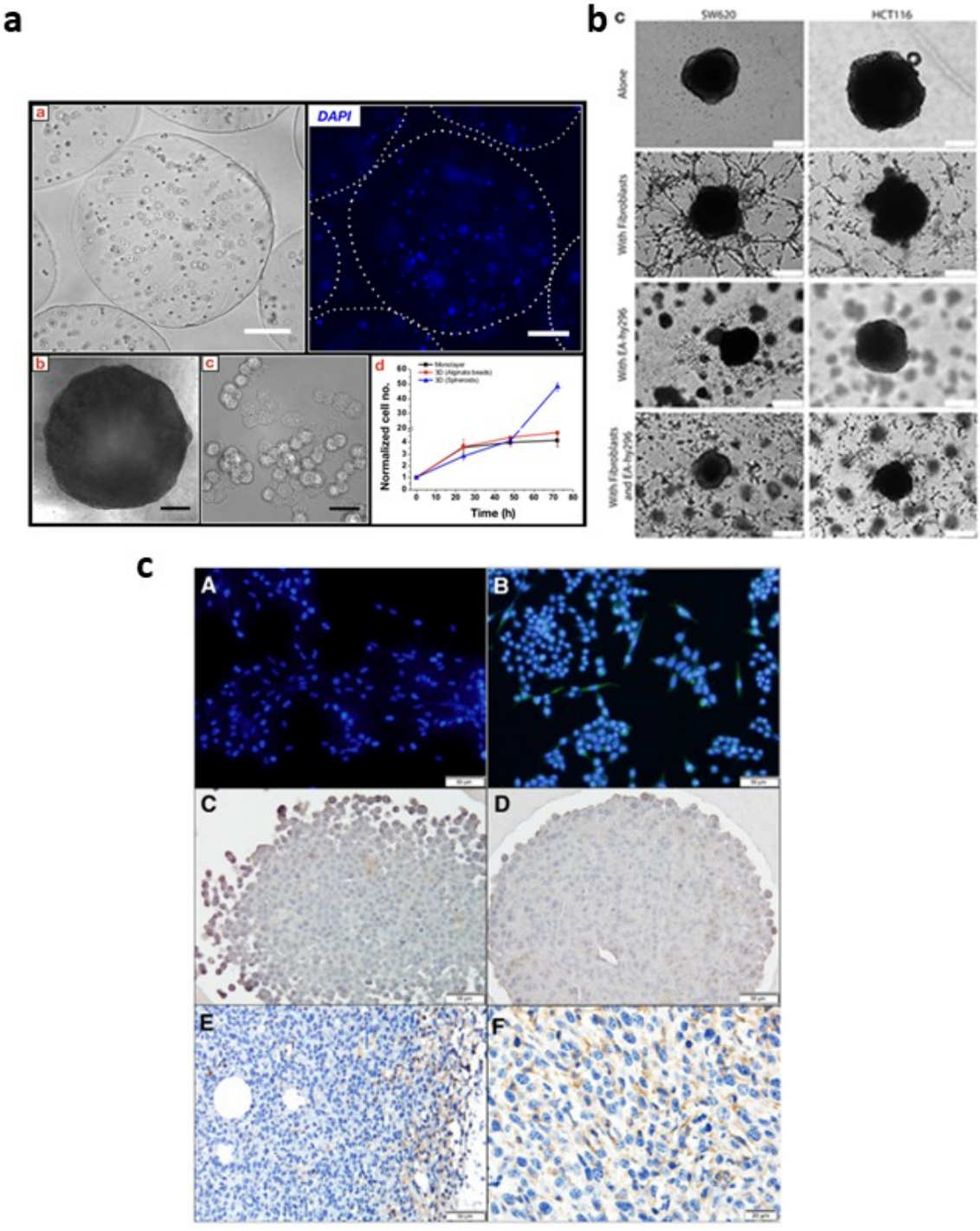

Figure 1.12 Currents *in vitro* 3D CRC models. Alginate beads encapsulating HCT-116 cells and comparison between *in vitro* CRC models (a) (de la Rosa, Wubetu et al. 2018); Representatives brightfield images of SW620 and HCT116 colon cancer cells cultured for 7 days under 3D conditions

in presence or absence of fibroblasts ± Ea.hy296 endothelial cells (b) (Cattin, Ramont et al. 2018); FAP-α expression in cocultures of CCD-18Co fibroblasts and colonic adenocarcinoma cells and the xenograft tumors in nude mice (Park, Lee et al. 2016).

1.6.2 *In vitro* 3D liver models

The liver is a key organ in the detoxification of chemicals and drugs, performing a multitude of metabolic reactions which ultimately result in clearance and excretion. Current 2D *in vitro* liver cell cultures have been widely applied in preclinical liver studies. However, they have failed to provide critical hepatocellular phenotype due to the lack of complex architecture and physiology of the liver and the loss of many liver-specific gene expressions and functions of primary human hepatocytes, such as albumin secretion, viral infectivity, and cytochrome P450 (CYP) enzyme activity. For this reason, *in vitro* 3D liver models have been developed to reproduce the complex structure of the liver with hepatocyte organization and cell-matrix contacts, as shown *in vivo* tissue. In addition, *in vitro* 3D liver models are promising to replicate morphological and functional features of *in vivo* hepatic tissue and keep cellular phenotypes in a relatively long-term culture for repetitive time-course measurement and sampling of various endpoints (Xu 2021). Thanks to these advantages, *in vitro* 3D liver models are widely applied in fields of drug development, disease modeling, and metabolic studies. Among various *in vitro* 3D liver culture models, hepatic spheroids which are formed by aggregation of cells, have been the focus of several studies. To this aim, Bell et al. fabricated 3D co-culture spheroids comprising primary human hepatocytes (PHH) and non-parenchymal cells (NPC) to investigate the acetaminophen-induced toxicity. The authors developed this hepatic spheroid culturing both the hepatocytes, which are the predominant cell of the liver, and non-parenchymal cells (NPCs) – which include Kupffer cells, stellate cells, and liver sinusoidal endothelial cells – in order to achieve *in vitro* models which can potentially be both physiologically and toxicologically relevant (Fig. 1.13 a) (Bell, Chouhan et al. 2020). However, multicellular spheroids sometimes suffer necrosis in the central areas of the relatively larger multicellular spheroids can because of oxygen/nutrient limitation, causing a decline in the spheroid functions. Other types of hepatic spheroids consisted in the use of alginate hydrogel beads into spheroids to improve oxygen/nutrient supply) and to preserve the morphology and function of the murine epithelial hepatic cells (Fig. 1.13 b) (Motoyama, Sayo et al. 2016). In addition, other spheroids can be further modified by the addition of artificial or natural micro- or nanoparticles to control the internal structure, act as carriers for various factors, or present different functional groups to the

aggregating cells. To this aim, Gentile et al. integrated PEG microparticles into liver progenitor spheroids to obtain 3D models of liver microtissues with controllable physical and biochemical signals. These methods of spheroids production have been used extensively to study cancer formation and to model *in vivo* cancer conditions (Fig. 1.13 c) (Gentile, Kourouklis et al. 2020).

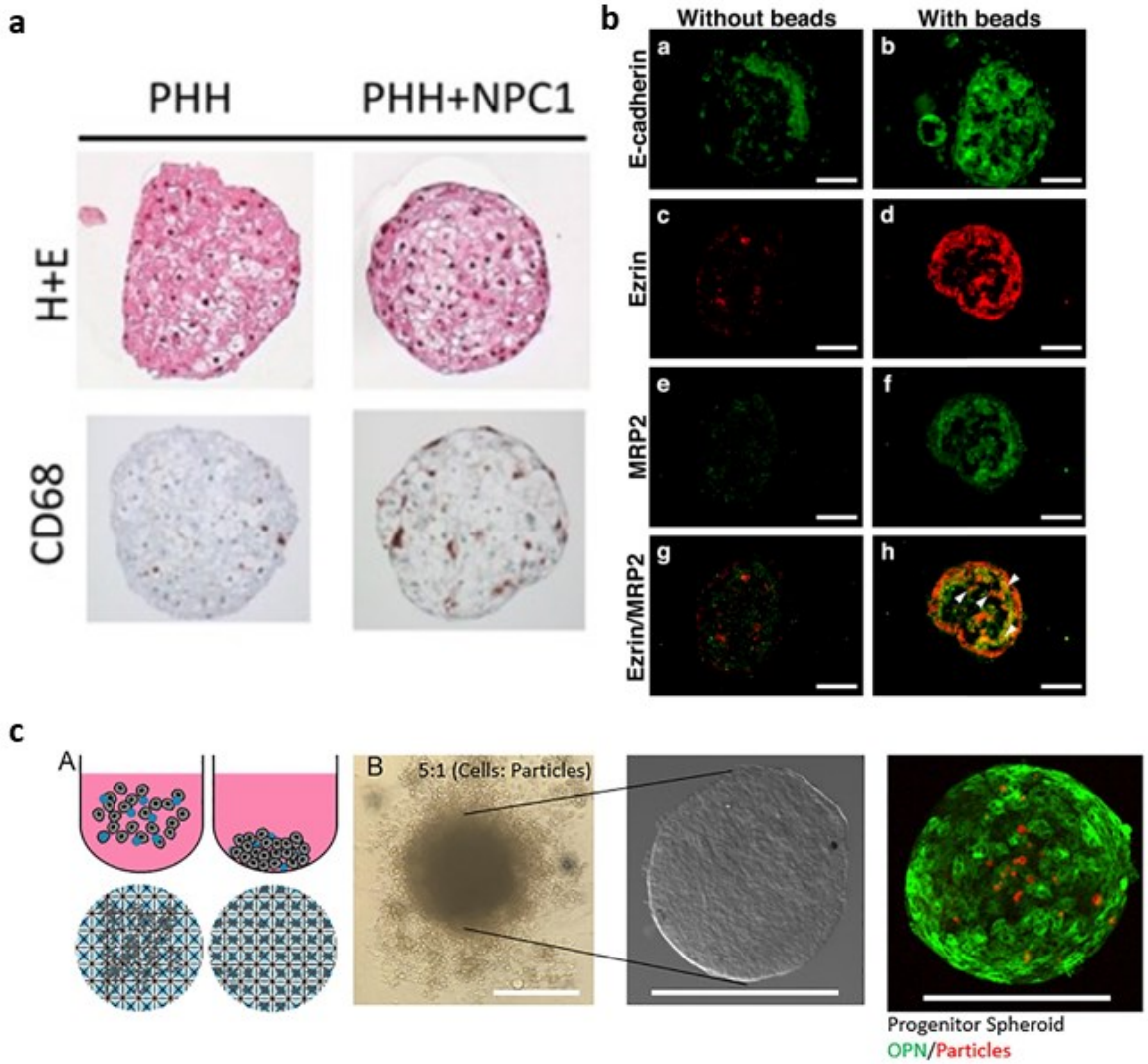

Figure 1.13 Currents *in vitro* Liver models. Characterization of primary human hepatocyte spheroids supplemented with non-parenchymal cells which express CD68 (a) (Bell, Chouhan et al. 2020); Multicellular spheroids with or without alginate beads stained with anti-E-cadherin, anti-ezrin, and anti-MRP2 (cell polarity-related proteins) (b) (Motoyama, Sayo et al. 2016); Engineering liver differentiation through hydrogel microparticles (a marker for differentiation Osteopontin-OPN) (c).

1.6.3 Microfluidic *in vitro* models of colorectal cancer and liver

Albeit previous studies indicated that *in vitro* 3D CRC models and 3D liver models proved promising solutions, since e.g. these are able to recapitulate the complexity of *in vivo* ECM of two models, other scientists focused on developing models even capable of mimicking the dynamic conditions existing in the tumor microenvironment, one of the "Achilles heels" of models previously discussed. To this aim microfluidic platforms that reproduce colorectal cancer (CRC-on-a-chip) and liver (Liver-on-a-chip) were developed. The microfluidic technologies allow accurate control over small fluid/liquid volumes and compartmentalization and combinatorial factors/ materials in a single platform, in which cells coexist in a 3D complex microenvironment. Similar to previous subsections, CRC-on-a-chip devices, and Liver-on-a-chip devices will be described following the same order.

Carvalho et al. established a complex 3D microfluidic system with a viable co-culture of HCT116 cells and Human Colonic Microvascular Endothelial Cells (HCoMECS) to assess the efficiency of the delivery of the anticancer drug, Gemcitabine, that was encapsulated in nanoparticles through a dynamic controllable gradient. Their microfluidic model consisted of three compartments: a central core for the HCT116 cells loaded in Matrigel supplemented with VEGF, and two perfused lateral channels for the HCoMECS cells seeding. The authors observed the invasion of endothelial cells from lateral channels to the central chamber through the pillars, in response to the VEGF treatment as well as the interconnected branches production, as shown in the early staged of tumor development (Fig. 1.14 a) (Carvalho, Barata et al. 2019). Another example of the CRC-on-a-chip platform was adapted from the "Intestine Chip" replacing Caco2 cells with, respectively, CRC cell lines or patient-derived tumor organoids and patient-derived CAFs into the top channel, and endothelial cells (HUVEC) into the bottom channel. Two compartments were separated by a thin and porous membrane and were coated with a tissue-specific ECM before cell seeding. In addition, a fluid flow and cyclic, peristalsis-like mechanical deformations were introduced to complete the physiologically relevant epithelial:endothelial tissue:tissue interface and create a CRC-on-Chip system. The authors demonstrated that this CRC-on-a-chip platform was suitable to investigate early stages of the CRC metastatic process, mimicking the intravasation of tumor cells into a blood vessel, monitoring via on-chip imaging and mass spectrometry-based metabolomics (Fig. 1.14 b) (Strelez, Chilakala et al. 2021).

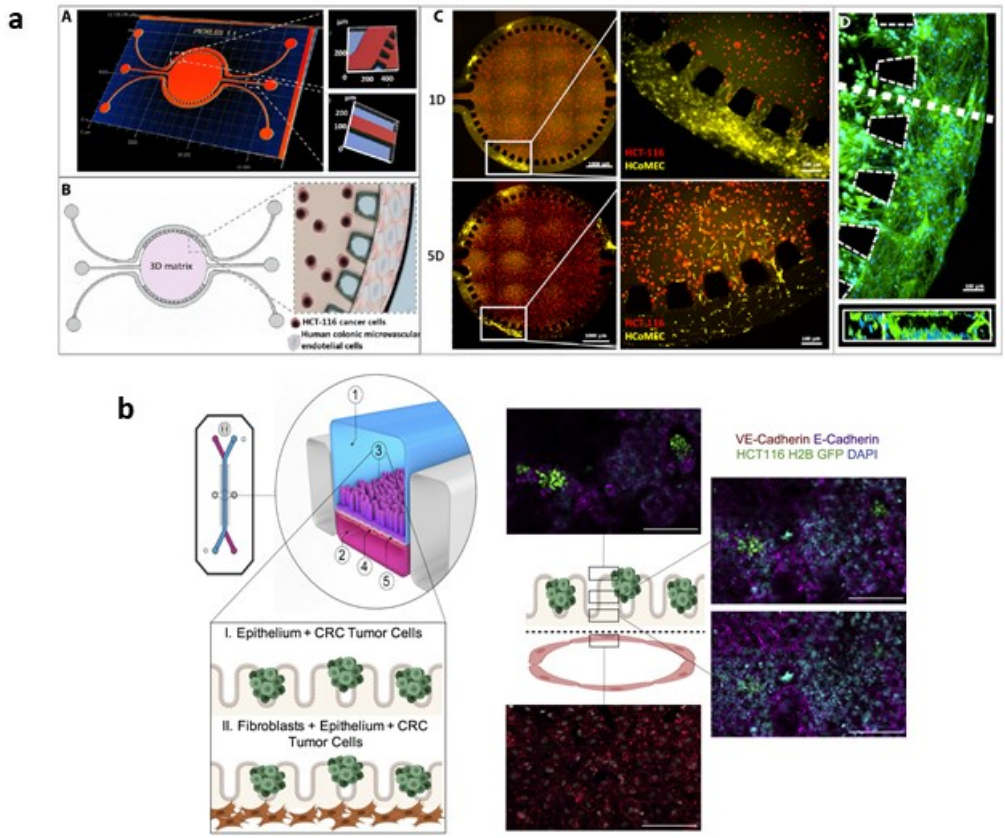

Figure 1.14 Currents CRC-on-a-chip platforms. Design and characterization of Human Colonic Microvascular Endothelial Cells (HCoMECS) (a) (Carvalho, Barata et al. 2019); Development and characterization of CRC-on-chip with the presence of fibroblasts (b) (Strelez, Chilakala et al. 2021).

Regarding Liver-on-a-chip platforms, Domansky et al. realized a perfused multiwell plate containing 12 fluidically isolated bioreactors in which co-culture of hepatocytes and non-parenchymal cells (NPC) (1:1) was seeded on the collagen-coated scaffolds (Fig. 1.15 a) (Domansky, Inman et al. 2010). The authors demonstrated that this microfluidic system was amenable to long-term maintenance of differentiated hepatocytes and NPC, however, the system didn't allow to physically monitor tissue formation during the culture period. In addition, the Liver Acinus Microphysiology System (LAMPS) provides a microfluidic platform in which was recapitulated the liver acinus structures (Fig. 1.15 b). This platform is an extension of the SQL-SAL (Vernetti, Senutovitch et al. 2016) by incorporating not only fresh or cryopreserved human hepatocytes but also human endothelial, immune and stellate cells. Moreover, the endothelial cells were separated from the hepatocytes by a thin porcine liver extracellular matrix (LECM) to mimic the Space of Disse. This system could be used to study oxygen Zones in the liver, investigate zone-specific liver metabolism and disease, and replace the NPCs with either primary human cells or IPSC-derived cells (Lee-Montiel, George et al. 2017). However, low flow rates of the microfluidic devices and the small volumes limit the oxygen

and nutrient supply, reducing cell viability during long-term culture. An evolution of the Liver on a chip platform consists in combining a 3D tissue model and a microfluidic system to improve the tissue-specific functions by mimicking the *in vivo* environment with blood flow, which supplies oxygen and nutrients.

In detail, Corrado et al developed a 3D liver tissue model integrated into a microfluidic system to better recapitulate liver morphological and functional properties. Briefly, liver-like microtissue precursors, consisting of liver hepatocellular carcinoma cell line (HepG2), were seeded on gelatin micro-carries (HepG2-µTPs), and cultured in a microfluidic device opportunely designed to mimic the hepatic sinusoids. The authors have demonstrated that µTPs configuration into the biochip allowed a long-term culture of HepG2 cells, a long-lasting metabolic activity, and the investigation of the mechanisms underlying alcoholic disease after ethanol administration compared to liver spheroids (Fig. 1.15 c) (Corrado, De Gregorio et al. 2019).

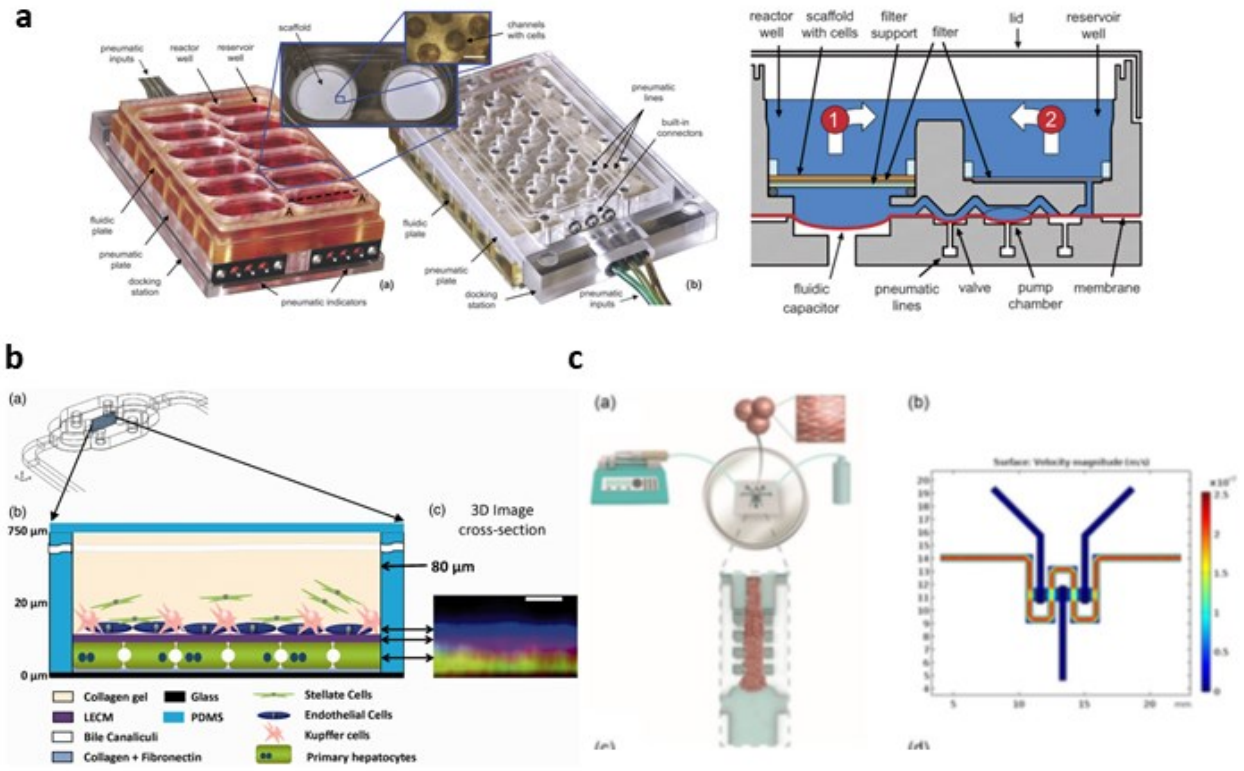

Figure 1.15 Currents Liver-on-a-chip platforms. The perfused multiwell with an array of 12 bioreactors and cross-section of the bioreactor (a) (Domansky, Inman et al. 2010); Structure of LAMPS (b) (Lee-Montiel, George et al. 2017); Representation of the HepG2-µTPs loading procedure and fluid dynamic simulation (c) (Corrado, De Gregorio et al. 2019).

1.6.4 Multi-organ-on-chip for investigating the metastasis process

Although CRC-on-a-chip and Liver-on-a-chip mimic the architecture and function of an organ by combining 3D bioengineered constructs, however, they are based on a single cell type or tissue and lack both a systemic dimension and cross-organ communication. In recent years, the different organ-on-a-chip platforms have been connected in a single device as multiorgan platforms which promote cross-organ communication, allowing the investigation of multiorgan processes and modeling of systemic diseases. In particular, cross-organ communication is the fundamental feature to induce the metastatic process, which is driven by CTC intravasation and their colonization of distant organs, in preferred niches. In the last years, Multi-Organ-on-a-chip platforms (MOC) have been employed, to mimic the migration of metastatic tumors from the primary to secondary tumor sites existing in native tumor tissues. Currently, the link between tissue engineering and microfluidic platforms has resulted in a potential tool to understand myriad parameters involved in cancer metastasis, predict, and control this cancer progression mechanism. One such microfluidic platform includes separate compartments for primary and secondary tumor sites enabling control over parameters affecting tumor cell migration and real-time monitoring of the cancer invasion process. For example, cancer cell migration from Colon cancer-based hydrogel construct to liver-based hydrogel construct was investigated under constant perfusion, and results were compared to non-metastatic colon cancer. The authors proved the formation of metastatic clusters in the liver, as well as the importance of the mechanical properties of the liver microenvironment for cancer spreading (Fig. 1.16 a) (Skardal, Devarasetty et al. 2016). Additional functionality was to expand from a single downstream colon cancer construct site to three downstream potential sites of metastasis, liver, lung, and endothelial constructs, demonstrating the preferential attitude of CRC cells of homing to the liver and lung constructs, in agreement with the clinical situations in human patients (Fig. 1.16 b) (Aleman and Skardal 2019). Another example of MOC was the hepatocellular carcinoma (HCC)–bone metastasis on-chip that reproduce the metastasis process from the liver to bone tissue to investigate the inhibitory effect of an herb-based compound, thymoquinone (TQ) (in free form or encapsulated in chitosan nanoparticle) which is known to block the cancer cell migration and invasion processes. The microfluidic device was made up of two compartments: a liver-based hydrogel construct that mimics the primary tumor site and a bone-based hydrogel construct, in which is present mineral hydroxyapatite (HAp), that simulates the secondary tumor site. A microporous polymer membrane that mimics the physical vascular barrier was sandwiched in between the two lower compartments and a common vascular chamber on top, with a cell medium

circulating during the culture period. The authors proved the presence of liver cancer cells that migrated, proliferated, and colonized from their site to the bone chamber, especially when Hap was present in bone-based hydrogel construct, indicating that the calcium ions released by bone construct affect the liver cancer cells. In addition, they demonstrated that TQ-encapsulated nanoparticles could inhibit the metastasis process for a longer duration differently from the free composition. The results proved the potential use of the HCC–bone metastasis-on-a-chip platform to reproduce the behavior of the metastatic process and to test several anti-metastatic drug candidates (Fig. 1.16 c) (Sharifi, Yesil-Celiktas et al. 2020). In another work, a breast cancer-to-bone metastasis on a chip was developed. It consisted of an endothelial cell monolayer that acts as a vascular barrier to a chamber containing a collagen gel in which are embedded osteo-differentiated human bone marrow-derived mesenchymal stem cells (hBM-MSCs) and breast cancer cells. The results showed how the molecular pathway involving breast cancer cell surface receptor CXCR2 and bone-secreted chemokine CXCL5 plays a pivotal role in the extravasation process of breast cancer cells (Fig. 1.16 d) (Bersini, Jeon et al. 2014). These MOC platforms, previously described, used a simplistic architecture of organoids formed by cell encapsulation in the hydrogel which is not suitable to recapitulate organ-specific extracellular matrix (ECM) *in vivo*-like function. To this aim, Wang et al. developed a MOC platform to mimic the progression of metastatic kidney cancer in the liver (Wang, Wu et al. 2020). Within this model, kidney cancer cells and a hepatic cell line were co-cultured in decellularized liver extracellular matrix (DLM)/GelMA-based 3D biomimetic liver microtissue via continuous perfusion. By changing the ratio from 1:9 to 9:1 in a liver-specific ECM, they observed that there was a linear anticancer relationship between the concentration of 5-FU and the number of kidney cancer cells and that the 5-FU-loaded PLGA-PEG nanoparticles showed a stronger killing efficacy than free 5-FU at the same concentration. This MOC platform could be used to evaluate the progression of kidney cancer cells and to predict therapeutic effects, assessing rapidly the anti-cancer efficiency and optimizing dosage regimes (Fig. 1.16 e).

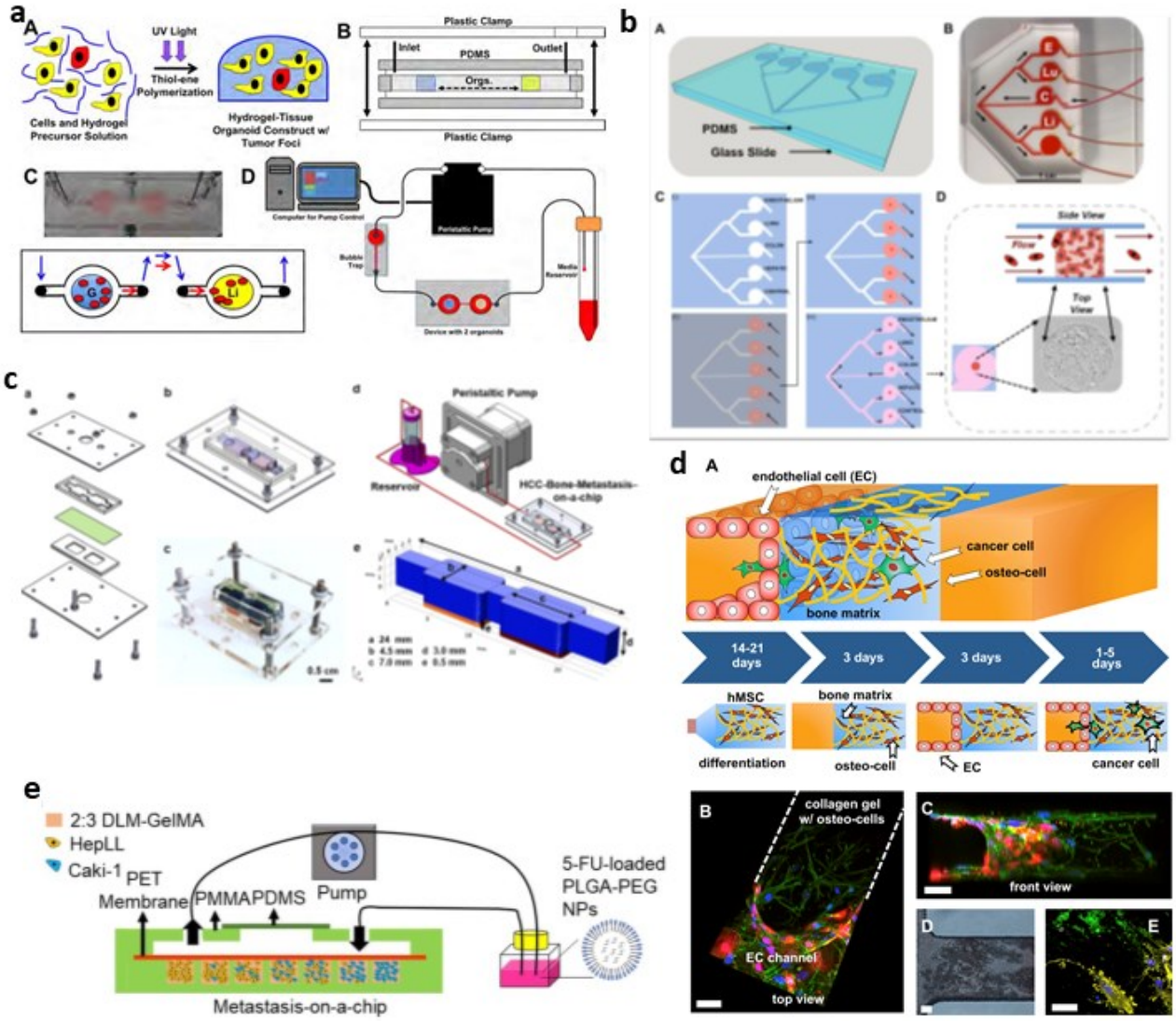

Figure 16 Currents Multi-Organ-on-a-chips (MOCs). metastasis-on-a-chip device mimicking colon carcinoma metastasis from the gut to the liver (a) (Skardal, Devarasetty et al. 2016); A multi-site metastasis-on-a-chip device (b); HCC–bone metastasis model (c) (Sharifi, Yesil-Celiktas et al. 2020); Generation of the osteo-cell-conditioned microenvironment using a MOC device to simulate breast cancer metastasis to bone (d) (Bersini, Jeon et al. 2014); Schematic of the progression of kidney cancer in the liver (e)

1.7 Limitations of current models and study purposes

In the final section of this chapter, the limits of previously described models are discussed. *In vitro* 3D CRC models and 3D liver models, developed and widely described in the literature, resemble the *in vivo* architecture and complexity of cell microenvironment, combining multiple cell types. Although they are models highly advanced compared with *in vitro* 2D models, however, they do not reproduce the microstructure, dynamic mechanical properties, and biochemical functionalities of whole living organs. CRC-on-a-chip and Liver-on-a-chip overcome these limits and allow to recapitulate not only the *in vivo* physiology of CRC and liver tissues but also the cross-organ communication, multi-organ on a chip (MOC), fundamental to investigate the metastasis process. These MOC platforms are highly reproducible and have showed promising results; nevertheless, these platforms either use cell monolayers seeded on microporous membranes coated by natural matrix (collagen, fibronectin, matrigel, etc.) or use simplified models, e.g. hydrogel, to resemble the *in vivo* ECM. In addition, others MOC platforms use decellularized matrices to reproduce the organ-specific ECM; nevertheless, similarly even these platforms are not able to faithfully mimic the human cell microenvironment because they use decellularized matrix-derived animal models. Therefore, to potentially overcome these limitations, this thesis proposes, on the one hand, to fabricate complex multicellular *in vitro* 3D CRC microtissues (3D CRC μTs) composed of CRC cells embedded in a fibroblast-assembled ECM and, on the other hand, to implement a metastasis-on-a-chip platform (MET-on-a-chip) composed by two chambers in which 3D CRC μTs and 3D liver μTs are cultured to reproduce the metastatic process from Colorectal cancer toward liver. Simultaneously, another aim was to investigate the synergistic effect of the curcumin-loaded nanoemulsion (CT-NE-Curc) in 3D CRC μTs treated with 5-FU.

The remainder of this thesis is organized as follows. Chapter 2 describes the fabrication and characterization of 3D CRC μTs and the combination treatments of NE-Curc and 5-FU on 3D CRC μTs. Chapter 3 focuses on the study of cancer cells migration in two different scenarios, considering both the presence and the absence of the target organ (i.e., 3D liver μTs); specifically, the cancer cell migration was firstly investigated using transwell inserts and later using custom-made MET-on-a-chip platforms. Supplementary Chapters 4 and 5 show both the preliminary results of combination treatments of NE-Curc and 5-FU on 2D cell cultures and the fabrication and characterization of different 3D liver μTs. Finally, chapter 6 summarizes the results of this work and draws conclusions.

2. Development of *in vitro* 3D Colorectal cancer and investigation of the synergistic effect of Curcumin

2.1 Introduction

It is known that TME plays a crucial role in cancer initiation, progression, and metastatic process. As described in the previous chapter, current *in vitro* 3D CRC models are limited in reproducing the crucial bidirectional cross-talk between cancer cells and the surrounding stromal tissues in which the extracellular matrix (ECM) orchestrates the signaling among different cell types (fibroblasts, endothelial cells, immune and inflammatory cells). Therefore, there is a growing necessity to develop accurate *in vitro* models able to replicate the TME in order to identify new agents that target specific molecular pathways. Several *in vitro* cancer models have been proposed in the literature, among those our research group developed a 3D tumor model, which we referred to as 3D tumor microtissues, characterized by a cell instructive microenvironment able to recapitulate the *in vivo* characteristics of TME. Here I exploited and slightly modified this previously established approach to develop 3D colon cancer tumor models and investigate the role of TME in cancer progression. In the first instance, I explored several configurations of 3D CRC µTs, 3D mono-cultured CRC µTs (3D HCT-116 µTs), and 3D co-cultured CRC µTs (3D HCT-116/Normal fibroblasts µTs), and assessed the difference in terms of cell growth, matrix deposition, ECM remodeling, bidirectional cross-talk between cancer cells and fibroblasts. Once established the better configuration of 3D CRC µTs, they were used as potential 3D models for drug and/or nutraceutical testing. In this context, 5 Fluorouracil (5-FU) is widely used as a chemotherapeutic agent for the treatment of metastatic colorectal cancer. It acts by blocking cancer cell proliferation and induces apoptosis by incorporation of its metabolites into DNA and RNA as a thymidylate synthase inhibitor to block dTMP synthesis (De Angelis, Svendsrud et al. 2006). Even though 5-FU is the most widely used to treat colorectal cancer, 5-FU is associated with several adverse risks, such as cardiotoxicity (Sara, Kaur et al. 2018), owing to the high dosage needed because of the progressive resistance of cancer cells.

Nutraceuticals are promising candidates to modulate the TME and thus support chemotherapy in Colorectal cancer (CRC), preventing the adverse risks on different organs. Curcumin has exhibited potential preventive and therapeutic effects such as anti-inflammatory, antioxidant, and, especially, anticancer (Wei, Yang et al. 2018). It has been shown that Curcumin enhances the cytotoxic effects of several chemotherapeutic agents such as 5-FU in colon cancer cells. However, as it is known many nutraceuticals, including Curcumin, are unstable or poorly water-soluble affecting their efficacy upon oral administration (Langella, Calcagno et al. 2018). Langella et al. developed oil in water nano-

emulsions in which Curcumin was encapsulated to enhance its bioavailability and anticancer activity (Langella, Calcagno et al. 2018). In conclusion, in the last parts of the next sections, I will describe the experiments carried out on 3D CRC µTs and 3D Stroma microtissues (3D NF µTs) to evaluate the synergistic effect of curcumin with 5-FU.

2.2 Materials and Methods

2.2.1 Cell types

Normal human dermal fibroblasts (NFs), extracted from healthy biopsies, were cultured in Eagle's Minimum Essential Medium (EMEM, Microgem) supplemented with 20% Fetal Bovine Serum (FBS, Sigma Aldrich), 200 mM L-Glutamine (Sigma Aldrich), 100 IU ml $^{-1}$ Streptomycin/Penicillin (Himedia), 100X Non-Essential Amino Acid (Euroclone). The seeding density of NF was 10 000 cells/cm^2 and the culture medium was changed every 2 days. For sub-culture, NFs were detached using Trypsin/EDTA 0,05% (Himedia) and centrifuged at 1000 rpm for 5 min.

Human colorectal carcinoma cell line (HCT-116 cells), transfected with pLVX-ZsGreen1-N1 (λex 493 nm, λem 505 nm) viral vector purchased from Clontech (USA), as indicated in (DOI: 10.1016/j.actbio.2016.11.072) and sub-cultured in Dulbecco's Modified Eagle's Medium (DMEM, Microgem) supplemented with 10% FBS (Sigma Aldrich), 200 mM L-Glutamine (Himedia), 100 IU ml $^{-1}$Streptomycin/Penicillin (Himedia). The recommended seeding density of HCT-116 cells was 20 000 cells/cm^2. HCT-116 cells were sub-cultured every 2-3 Days, were detached using Trypsin/EDTA 0,05% (Himedia), and centrifuged at 1000 rpm for 5 min. The change of culture medium was carried out every 2 Days.

All cell lines were incubated at 37°C in a humidified atmosphere with 5% CO_2.

2.2.2 Microscaffold production

Gelatin porous microbeads (GPMs) have been produced according to a modified double emulsion technique (O/W/O). In detail, Gelatin (type B Sigma Aldrich Chemical Company, Bloom 225, Mw¼176,654 Da) was dissolved into 10 ml of water containing TWEEN 85 (6% w/v) (Sigma Aldrich Chemical Company). The solution was kept at 40 °C. Toluene containing SPAN 85 (3% w/v) (Sigma Aldrich Chemical Company) was continuously added to the aqueous gelatin solution (8% w/v) to obtain primary oil in water (O/W) emulsion forming droplets in the gelatin solution until saturation.

Microbeads of gelatin containing droplets of toluene were produced through the addition of excess toluene (30 ml) that allowed for a double emulsion (O/W/O). After cooling below 5 °C, 20 ml of ethanol were added to extract toluene and stabilize GPMs. The resulting microspheres were filtered and washed with acetone and then dried at room temperature. GPMs were separated selectively by using commercial sieves (Sieves IG/3-EXP, Retsch, Germany). GPMs with 75-150 µm size range were recovered and further processed. GPMs have been stabilized using chemical treatment with 4% glyceraldehyde (GAL), to make them stable in an aqueous environment at body temperature. GPMs were dispersed into an acetone/water solution containing different amounts of GAL and mixed at 4 °C for 24 h. Then microbeads were filtered and washed with acetone and dried at room temperature. To use them for cell culture, the microbeads were sterilized in absolute ethanol and washed in Phosphate Buffered Saline 1X Solution (PBS) (Sigma).

2.2.3 *In vitro* 3D Colorectal cancer microtissue fabrication

Different 3D Colorectal Cancer microtissues were performed:

- 3D mono-cultured Colorectal Cancer microtissues, formed by HCT-116 cells (3D HCT-116 µTs), and 3D Stroma microtissues, that consisted of Normal Fibroblasts (3D NF µTs);
- 3D co-cultured Colorectal Cancer microtissues (3D CRC µTs), consisting of HCT-116 cells and Normal Fibroblasts.

All 3D CRC µTs were produced in 6-well Clear Flat Bottom Ultra-Low Attachment Multiple Well Plates (Corning ® Costar ®), monitored and analyzed for different time points.

In vitro 3D Stroma microtissues (3D NF µTs) and 3D mono-cultured Colorectal Cancer Microtissues (3D HCT-116 µTs) production

To fabricate the 3D NF µTs and 3D HCT-116 µTs, 24 mg of sterile GPMs were loaded together with 1.2 x 10^6 HCT116 cells (10 cell/microbeads ratio) or 2.4 x 10^6 NFs (20 cell/microbeads ratio). To promote NF or HCT-116 cells seeding on GPMs, an intermittent stirring regime (30 min at 0 rpm, 5 min at 30 rpm) for 6 h was carried out. Then, 3D NF µTs were kept under continuous stirring (dynamic condition) at 80 rpm for up to 12 Days. On the contrary,3D HCT-116 µTs were left in static condition overnight. The culture medium used for 3D NF µTs was Eagle's Minimum Essential

Medium (EMEM, Microgem) supplemented with 20% Fetal Bovine Serum (FBS, Sigma Aldrich), 200 mM L-Glutamine (Sigma Aldrich), 100 IU ml $^{-1}$ Streptomycin/Penicillin (Himedia), 100X Non-Essential Amino Acid (Euroclone). Instead, for 3D moCRC µTs, Dulbecco's Modified Eagle's Medium (DMEM, Microgem) supplemented with 10% FBS (Sigma Aldrich), 200 mM L-Glutamine (Himedia), 100 IU ml $^{-1}$ Streptomycin/Penicillin (Himedia) was used. The culture medium was changed on the first day and every 2 days until the end of the experiments. For 3D NF µTs, 50 µg/ml of Ascorbic Acid was added into the culture medium every 2 days. All cultures were maintained at 37°C in a humidified 5% CO_2 incubator.

***In vitro* 3D co-cultured Colorectal Cancer Microtissues (3D CRC µTs) production**

To fabricate the 3D CRC µTs, 24 mg of GPMs were mixed with HCT-116 cells/NF (1:2 cell ratio). To promote cell seeding on GPMs, an intermittent stirring regime (30 min at 0 rpm, 5 min at 30 rpm) for 6 h was carried out. Then, dynamic cultures were kept under continuous stirring at 30 rpm for up to 12 Days. Moreover, different 3D CRC µTs were performed and growth with Dulbecco's Modified Eagle's Medium (DMEM, Microgem) supplemented with 10% FBS (Sigma Aldrich), 200 mM L-Glutamine (Himedia), 100 IU ml $^{-1}$ Streptomycin/Penicillin (Himedia): HCT-116 cells/NF 1:2 co-cultured seeded at Day 0 (3D CRC $_{Day\ 0}$ µTs); HCT-116 cells/NF 1:2 obtained by seeding the HCT-116 cells on 3D NF µTs at Day 4 (3D CRC $_{Day\ 4}$ µTs); HCT-116 cells/NF 1:2 obtained by seeding HCT-116 cells on 3D NF µTs at Day 8 (3D CRC $_{Day\ 8}$ µTs). The Medium was changed on the first day and every 2 Days until the end of the experiments, by adding or not 50 µg/ml of Ascorbic Acid. In detail, the medium without Ascorbic Acid was changed at Days 4 and 8 in order to seed HCT-116 cells. Moreover, other 3D CRC µTs were produced by adding Ascorbic Acid also when HCT-116 cells were seeded at 4 Days, in order to induce ECM production. All cultures were maintained at 37°C in a humidified 5% CO_2 incubator.

2.2.4 Characterization of 3D Colorectal cancer microtissue

***In vitro* 3D Colorectal Cancer microtissues (3D CRC µTs) analyses**

To monitor cell growth on GPMs, aliquots of 1 ml were collected for each sample. Briefly, 200 µl of microtissues suspension were transferred to a cell culture dish (w/2 mm grid Nunc) for GPMs counting, after that the microtissues suspension was collected in a 2 ml Eppendorf tube and washed

twice with PBS. To detach cells from GPMs, microtissues were digested by collagenase A (Roche Life sciences, Italy) for 50 min at 37 °C, centrifuged 5 min at 2000 rpm, and incubated 5 min in Trypsin (Lonza, Italy). The detached cells were, then, counted using a hemocytometer. For morphological characterization of cell distribution, 3D NF µTs, 3D CRC µTs and 3D HCT-116 µTs aliquots (500 µl) were collected during microtissue assembling time at Days 1, 4, 8, and 12 and then fixed with 4% paraformaldehyde (PFA). Live monitoring of the collagen amount and assembly, as well as immunofluorescence analyses, were carried out employing Confocal Leica TCS SP5 II combined with a Multiphoton Microscope where the NIR femtosecond laser beam was derived from a tunable compact mode-locked titanium:sapphire laser (Chamaleon Compact OPO-Vis, Coherent). Therefore, moCRC and coCRC µTs were observed by using a laser that excited GFP, expressed by HCT-116 cells (λex= 488 nm and λem=510 nm), simultaneously with a laser that induced second harmonic generation (SHG) (λex = 840 nm and λem = 420 ± 5) on unstained neo-synthesized collagen structures. HCT-116 cells maintained the GFP expression during the experimental phase and also after PFA fixing procedure that is useful for online monitoring and histotypical characterization, respectively.

Colorectal cancer cells counting

In order to evaluate the tumor cells proliferation in 3D CRC µTs, Colorectal cancer cells nuclei - that preserved the GFP expression- were counted from images acquired by Confocal Leica TCS SP5 II combined with a Multiphoton Microscope. In detail, cell counting analysis was carried out by using the Fiji plugin “Cell Counter”: 4 images were selected for each time point and the counting was carried out by selecting 5 ROI in each image. The results of cell counting were expressed as the ratio between the total cell number and ROI area. Statistical comparisons were performed with the Friedman test for a non-parametric statistical test. P-values of <0.05 denote statistically significant differences. For all data sets, experiments were repeated in independent studies.

Collagen fraction and Degree of collagen assembly analysis

Two-photon excited fluorescence was used to induce second harmonic generation (SHG) and obtain high-resolution images of unstained collagen structures of the endogenously produced ECM into 3D coCRC µTs. The samples were observed under Confocal Leica TCS SP5 II combined with a

Multiphoton Microscope where the NIR femtosecond laser beam was derived from a tunable compact mode-locked titanium: sapphire laser (Chamaleon Com- pact OPO-Vis, Coherent). The unstained collagen of samples was observed (SHG, λex = 840 nm, λem = 420 ±5 nm). Then, SHG images of HCT-116/NF µTPs were analyzed by using Fiji software. Collagen fraction (CF) analysis was carried out by measuring the collagen portion in the ECM space in a selected ROI. The collagen portion in the ECM corresponds to bright pixels, named Number of pixels from the collagen (Nc), with respect to black pixels, which represent the non-collagen portion, named Number of pixels non-collagen portion (Nb). For each time point, the collagen fraction was expressed as the ratio between bright pixels (Nc) and the total of bright pixels and black pixels (Nb) in the selected ROI, as reported in Eq:

$$CF = \frac{Nc}{Nc + Nb} \quad (1)$$

Moreover, the degree of collagen assembly (CAD) was evaluated by analysing the intensity of the SHG signal. SHG images were analysed in order to calculate the average intensity, as described by Eq:

$$CA \propto \bar{I} = \frac{\sum_{i=1}^{255} I_i p_i}{\sum_{i=1}^{255} p_i} \quad (2)$$

Where $\bar{I}$ is the average intensity, is I_i the intensity corresponding to the pixel p_i while the index i=xi, yi runs in the gray value interval from 1 to 255. The intensity $\bar{I}$ of the collagen network is known to be proportional to both mechanical properties and to the degree of assembly of the newly synthesized collagen. Statistical comparisons were performed with the ANOVA test followed by the Tukey HSD test. P-values of <0.05 denote statistically significant differences. For all data sets, experiments were repeated in independent studies.

Collagen fiber Orientation and Alignment analysis

To determine the changes in the orientation of individual collagen fibers in the 3D CRC µTs and mo NF µTs, a quantitative analysis of collagen fiber orientation was performed by using the Fiji plugin “Orientation J”. “Orientation J” measures the Coherency, which indicates the degree to which the collagen fibers were oriented. The eccentricity of ellipses demonstrates the Coherency Value: the

narrower the ellipse indicates a higher coherency value (= 1), in which the collagen fibers are perfectly aligned, while a perfect circle indicates a lower coherency value (= 0), in which the collagen fibers have a completely random distribution. The analysis was carried out on 4 images at 12 Days by measuring the alignment of collagen fibers in the ECM with HCT-116 cells in a ROI (38,3 x 38,3 μm^2). The mean of three measurements collected in different zones of each section was calculated and the results were expressed as the ratio between the Coherency index and ROI area. Two-dimensional Fast Fourier transform (FFT) of images acquired with SHG and confocal microscopy was used for the evaluation of HCT-116 cells alignment along collagen fibers. Grayscale 8-bit of single-channel images, represented by green channel for HCT-116 cells and gray channel for SHG signal, were obtained and processed using ImageJ software as follows: Select Process-Subtract Background-Image calculator. Then, the images were cropped in both 1024 x 1024 pixels and 256 x 256 pixels in order to carry out analysis from the global to a specific area. For FFT alignment, ImageJ software (NIH, http://rsb.info.nih.gov/ij) supported by an oval profile plug-in (authored by William O'Connnell) was used, as described in detail in the studies of Ayres et al. (Ayres, Jha et al. 2008). Briefly, single fluorescent or SHG images were analyzed by Process-FFT for FFT transformation. The resulting frequency plot contained a cluster of white pixels placed in a symmetrical, circular pattern around the origin. Then, a circular ROI was placed on the frequency plot and the oval profile plug-in was used, in which the pixel intensities were summed up along the radius for each angle of the circular projection (0-360°). As result, a 2D FFT alignment plot characterized by the summed pixel intensities for each radius against the corresponding degrees was obtained. All Statistical comparisons were performed with the ANOVA test followed by the Tukey HSD test. P-values of <0.05 denote statistically significant differences. For all data sets, experiments were repeated in independent studies.

Immunofluorescence procedure

For the immunofluorescence procedure, 3D CRC µTs and 3D NF µTs were withdrawn from the dynamic culture at the end of culture time, washed twice with PBS, and then fixed with 4% PFA for 20 min. After washing, the samples were incubated with the permeabilizing solution (PBS-Triton X-100 0.1%) for 10 min, blocked with PBS-BSA 3% and 1% solutions, and incubated with primary antibody MMP-9 (ab119906), α-SMA 1:100 (5694, Abcam), FAPα (PA5-99313) and YAP-1 1:250 (PA1-46189, Invitrogen) for 2 hours at RT, respectively. Then, the samples were incubated with

secondary antibody 1:500 (Alexa fluor 546) for 1 hour at RT and the nuclear stain was performed by applying a diluted suspension (1:1000) of 1, 5-bis (Ruiz-Espigares, Nieto et al.)-4, 8-dihydroxyanthracene-9, 10-dione (DRAQ-5) for 15 min at RT. The images were obtained using confocal laser scanning microscopy (CLSM). The samples were observed to highlight the simultaneous excitation of the two different fluorophores used (DRAQ5 λex= 488/647nm, λem= 647/681nm; α-SMA and YAP-1 λ_{ex} 540–545 nm, λ_{em} 570–573 nm).

Histology of 3D CRC µTs on paraffin sections

3D CRC µTs, fixed in 4% PAF, were dehydrated in Ethanol from 75% to 100% and treated with Xylene (A9982 ROMIL) before the Paraffin inclusion. Microtissue slices thick 7µm were cut using a microtome, were laid in the warm water, and left in the oven at 30-40°C to dry them overnight. Then, the sections were deparaffinized using xylene, hydrated in ethanol from 100% to 75%, washed in water, and stained using Hematoxylin/Eosin (Bio Optica W01030708). The sections were mounted with Histomount Mounting Solution (Bio Mount HM 05-BMHM500 Bio-Optica) on coverslips and the morphological features of µTPs were observed with a light microscope (Olympus, BX53).

2.2.5 Treatments with CT-CT-NE-Curc and 5-FU on 3D CRC µTs, 3D NF µTs, and 3D HCT-116 µTs

Nanoemulsions preparation (CT-NE-Curc)

The nanoemulsion consisted of an oil-in-water (O/W) core coated with a mucoadhesive chitosan derivative, namely chitosan. Oil in water nanoemulsion was obtained by using a high-pressure homogenizer (Microfluidics M110PS), as previously described (Langella, Calcagno et al. 2018). Briefly, 5.8 g of surfactant (egg lecithin) in 24 ml of oil (soybean oil) were used and the oil phase was loaded with 100 mg of curcumin. To promote dissolution, the oil phase containing surfactant and curcumin was mixed by alternating a high-speed blender (RZR 2102 control, Heidolph) at 60 °C and 500 rpm to room temperature sonication with an immersion sonicator (Ultrasonic Processor VCX500 Sonic and Materials), according to a process protocol previously reported. Then, to obtain the pre-emulsion, the oil phase was added dropwise to 90 g of Milli-Q water and mixed using the immersion sonicator under temperature control in order to avoid overheating. The pre-emulsions were finally passed at 2000 bar through the high-pressure valve homogenizer (Microfluidics M110PS) according to the same previous protocol. Primary nanoemulsion with Curcumin loaded

was then coated with Chitosan exploiting their positive charge for the deposition around the oil droplets stabilized with lecithin, which is negative. Chitosan solution was prepared in 0.1Macetic acid Milli-Q water bringing the pH to 4 with a small addition of NaOH 6 M solution. The two phases were mixed 1:1 (v:v) quickly under vigorous stirring and kept under stirring for 15 min to allow uniform Chitosan deposition, thus obtaining secondary emulsions. The final concentration of oil was 10 wt%, whereas chitosan was 0.1 wt% to guarantee saturation of Chitosan around emulsion. The emulsions coated with Chitosan were passed through a high-pressure valve homogenizer at 700 bar for 100 continuous steps and re-processed after a few days in the same conditions on the same systems (at 700 bar for 100 continuous steps) having found benefit in terms of stability by the double re-dispersion process. Nanoemulsions exhibited a size of 94.87 nm in diameter, a Z-potential of +21.5, and a Polydispersity index (PDI) of 0.08.

Preparation of 5-FU and CT-NE-Curc treatments

For drug treatments, the 5F-U stock solution in DMSO [384 mM] was diluted at different concentrations in DMEM high glucose supplemented with 10% FBS (Sigma Aldrich), 200 mM L-Glutamine (Himedia), 100 IU ml^{-1} Streptomycin/Penicillin (Himedia): 0 µM; 10 µM; 100 µM; 1 mM; 10 mM. The final concentration of DMSO was less than 1% of drug treatment. Following, CT-NE-Curc was sterilized using PVDF filters (Millicell) and diluted 1:8 into the cell medium. Then 3D CRC µTs and 3D NF µTs were pre-treated with CT-CT-NE-Curc and incubated at 37◦C in a humidified 5% CO2 for 2 h. After 2 h, 3D CRC µTs and 3D NF µTs were washed two times with sterile PBS and were treated with 5-FU at 0 µM; 10 µM; 100 µM; 1 mM; 10 mM. The effects were observed after 24 h and 48 h.

Cell vitality assay

To evaluate the cell viability after 5-FU and CT-NE-Curc combination treatment in 2D cell culture models as well as in 3D CRC µTs, 3D NF µTs, and 3D HCT-116 µTs, 3-(4,5-dimethylthiazol-2-yl)-2,5-diphenyltetrazolium bromide (MTT) assay was used according to the manufacturer's instructions (Sigma). Briefly, after 24 and 48 h of treatment, both 3D CRC µTs and 3D NF µTs were washed two times with PBS, 200 µl of the MTT solution (5mg/ml) was added in each well incubating at 37◦C in a humidified 5% CO_2 for 3 h in the dark. Then, MTT solution was removed from each well and the

remaining crystals (formazan precipitates) were solubilized with 200 µl of DMSO, and the cells were incubated for an additional 30 min at 37 °C with gentle shaking. In the end, the optical density of each well sample was measured with a microplate spectrophotometer reader at 570 nm, and the cell viability (%) was calculated by the following equation:

$$Cell\ Viability\ (\%) = \frac{OD\ treated}{OD\ control}\ x\ 100 \quad (3)$$

All statistical comparisons were performed with the ANOVA test followed by the Tukey HSD test. P-values of <0.05 denote statistically significant differences. For all data sets, experiments were repeated in independent studies.

2.3 Results and Discussions

2.3.1 Time evolution of *in vitro* 3D Colorectal Cancer microtissues

Two configurations of *in vitro* 3D Colorectal Cancer microtissues was produced:

- 3D *in vitro* mono-cultured Colorectal Cancer microtissues (3D HCT-116 µTs);
- 3D *in vitro* Stromal microtissues (3D NF µTs);
- 3D *in vitro* co-cultured Colorectal Cancer microtissues (3D CRC µTs).

3D HCT-116 µTs and 3D NF µTs were composed of HCT-116 cells and NFs, respectively. Different configurations of 3D CRC µTs were developed: HCT-116 cells/NF co-cultured at Day 0 (3D CRC $_{Day\ 0}$ µTs); HCT-116 cells/NF obtained by seeding the HCT-116 cells on 3D NF µTPs at Day 4 (3D CRC $_{Day\ 4}$ µTs); HCT-116 cells/NF obtained by seeding HCT-116 cells on 3D NF µTPs at Day 8 (3D CRC $_{Day\ 8}$ µTs). The evolution of 3D CRC µTs, 3D HCT-116 µTs, and 3D NF µTs was monitored during 12 Days of culture. Confocal images of 3D CRC $_{Day\ 0}$ µTs (Fig. 2.1 a-c) showed an increase of HCT-116 cell proliferation (GFP green signal) from Day 4 to Day 12, compared to 3D CRC $_{Day\ 4}$ µTs where the cell proliferation was more pronounced at Day 12, as reported in the graph (Fig. 2.1 j). However, the SHG signal indicating the ECM production in 3D CRC $_{Day\ 0}$ µTs was shown at Day 8 (Fig. 2.1 b), while it was reduced at Day 12 (Fig. 2.1 c), probably due to the increased HCT-116 cell proliferation that has determined high rate of ECM degradation. In addition, the Collagen Fraction (CF) in 3D CRC $_{Day\ 0}$ µTs and 3D CRC $_{Day\ 4}$ µTs was observed by evaluating unstained collagen from SHG images obtained using multi-photon microscopy. The CF increased from Day 4 to Day 12 in 3D CRC $_{Day\ 4}$ µTs (Fig. 2.1 d-f), as reported in the graph (Fig. 2.1 k) in which a linear production overtime of the ECM was

displayed for 3D CRC $_{Day\ 4}$ µTs, differently than 3D CRC µTs $_{Day\ 0}$. Moreover, the CAD analysis was carried out in order to assess the assembly of ECM using the SHG images of 3D CRC $_{Day\ 0}$ µTs and 3D CRC $_{Day\ 4}$ µTs (Fig. 2.1 l). CAD analysis showed an increased assembly degree of collagen in 3D CRC $_{Day\ 0}$ µTs over time, but these values sharply decrease at Day 12, due to the proteolytic action of HCT-116 cells that promote ECM degradation. In contrast, the assembly degree of collagen in 3D CRC $_{Day\ 4}$ µTs was increased from Day 4 to Day 8, without changing over time. Based on preliminary results, 3D CRC $_{Day\ 4}$ µTs was chosen for the following analyses having a homogeneous distribution of HCT-116 cells into the ECM, unlike 3D CRC $_{Day\ 8}$ µTs (Fig. 2.1 g-i) which showed a heterogeneous distribution of HCT-116 cells into the surrounding ECM at Day 12, as shown in Fig. 2.1 i. However, 3D CRC $_{Day\ 4}$ µTs showed a reduction in collagen production that endured over time. This behavior should be attributable to the proteolytic action of HCT-116 cells that increase the ECM degradation during the dynamic culture. In this direction, to increase collagen production from Day 0 of culture, Ascorbic Acid at a concentration of 50 µg/ml was added during all duration of dynamic culture. Ascorbic acid concentration does not affect the cancer cells viability (Lee, Jeong et al. 2019). In this perspective, a comparison between 3D CRC $_{Day\ 4}$ µTs with Ascorbic Acid (w AA) and without Ascorbic Acid (w/o AA) was performed through confocal characterization employing multi-photon microscopy. SHG signal of unstained collagen fibers and GFP signal of HCT-116 cells were analyzed (Fig. 2.2). Our results showed that there were no relevant differences in cancer cell proliferation from Day 4 to 8 between the two configurations analyzed (3D CRC $_{Day\ 4}$ µTs $_{w\ AA}$, Fig. 2.2 a, b and 3D CRC $_{Day\ 4}$ µTs $_{w/o\ AA}$, Fig. 2.2 d and e). An increased cancer cell proliferation in 3D CRC $_{Day\ 4}$ µTs $_{w\ AA}$ at Day 12 (Fig. 2.2 c) compared to 3D CRC $_{Day\ 4}$ µTs $_{w/o\ AA}$ (Fig. 2.2 f), was reported in the graph (Fig. 2.2 g). Therefore, it has been shown that Ascorbic Acid did not affect the cancer cells viability at the concentration used. Furthermore, the ECM production in 3D CRC $_{Day\ 4}$ µTs $_{w/o\ AA}$ increase slightly from Day 4 to Day 8, as shown in 3D CRC $_{Day\ 4}$ µTs $_{w\ AA}$, but there was a strong SHG signal in 3D CRC $_{Day\ 4}$ µTs $_{w\ AA}$ at Day 12, unlike 3D CRC $_{Day\ 4}$ µTs $_{w/o\ AA}$, as reported in the graph of collagen fraction analysis (Fig. 2.2 k). Moreover, CAD analysis was carried out analyzing the SHG images of 3D CRC $_{Day\ 4}$ µTs $_{w\ AA}$ and 3D CRC $_{Day\ 4}$ µTs $_{w/o\ AA}$. The images highlighted a slight increase of SHG intensity signal from Day 4 to Day 8 and strong signal in 3D CRC Day 4 µTs $_{w\ AA}$ at Day 12, compared to 3D CRC $_{Day\ 4}$ µTs $_{w\ AA}$ (Fig. 2.2 i). CF and CAD analyses (Fig. 2.2 h, i) not showed a relevant signal between Day 4 and Day 8. It could be due to a continuous ECM remodeling in which the action of metalloproteases, produced and released by cancer cells, to degrade the ECM was balanced by new ECM formation

(Said, Raufman et al. 2014). On Day 12, 3D CRC $_{Day\ 4}$ µTs $_{w\ AA}$ samples displayed good quality of ECM without significant degradation, due to the addition of Ascorbic Acid (Phillips, Combs et al. 1994).

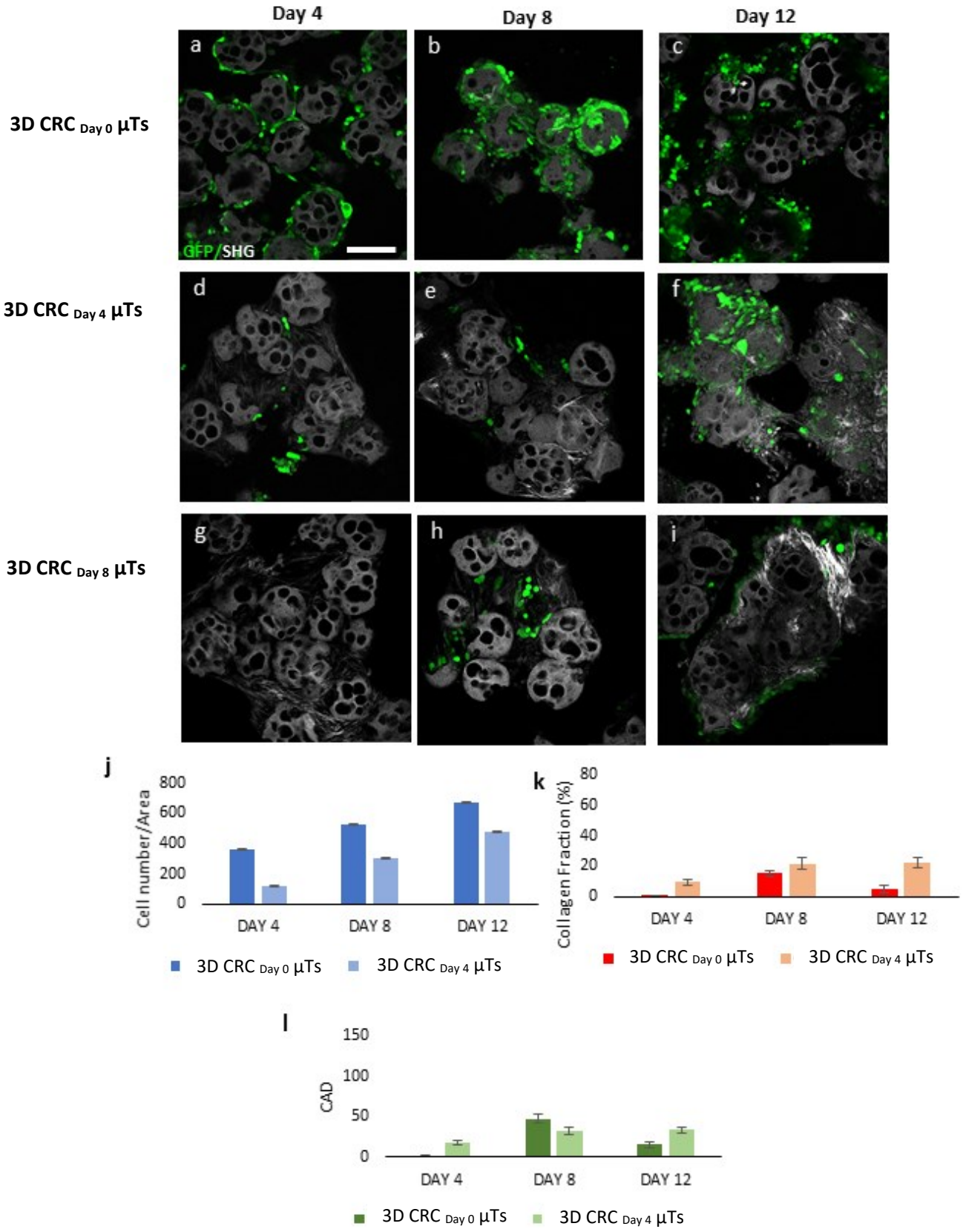

Figure 2.1 Morphology and cell distribution comparison between 3D CRC $_{Day\ 0}$ µTs (a, b, c), 3D CRC $_{Day\ 4}$ µTs (d, e, f), and 3D CRC $_{Day\ 8}$ µTs (g, h, i) at 4, 8 and 12 Days. Confocal images of GFP (green) signal revealing the dissemination of CRC cells (HCT-116 cells) into the ECM neo-formation, shown by the SHG, signal scale bar 155 µm; Comparative analysis of HCT-116 cells proliferation (j), Collagen fraction (k), and Collagen assembly degree (l) between 3D CRC $_{Day\ 0}$ µTs and 3D CRC $_{Day\ 4}$ µTs. All the experiments were performed in triplicate (n = 3), values represent the mean and the standard deviation (g) (p ∗< 0.05; p ∗∗< 0.05).

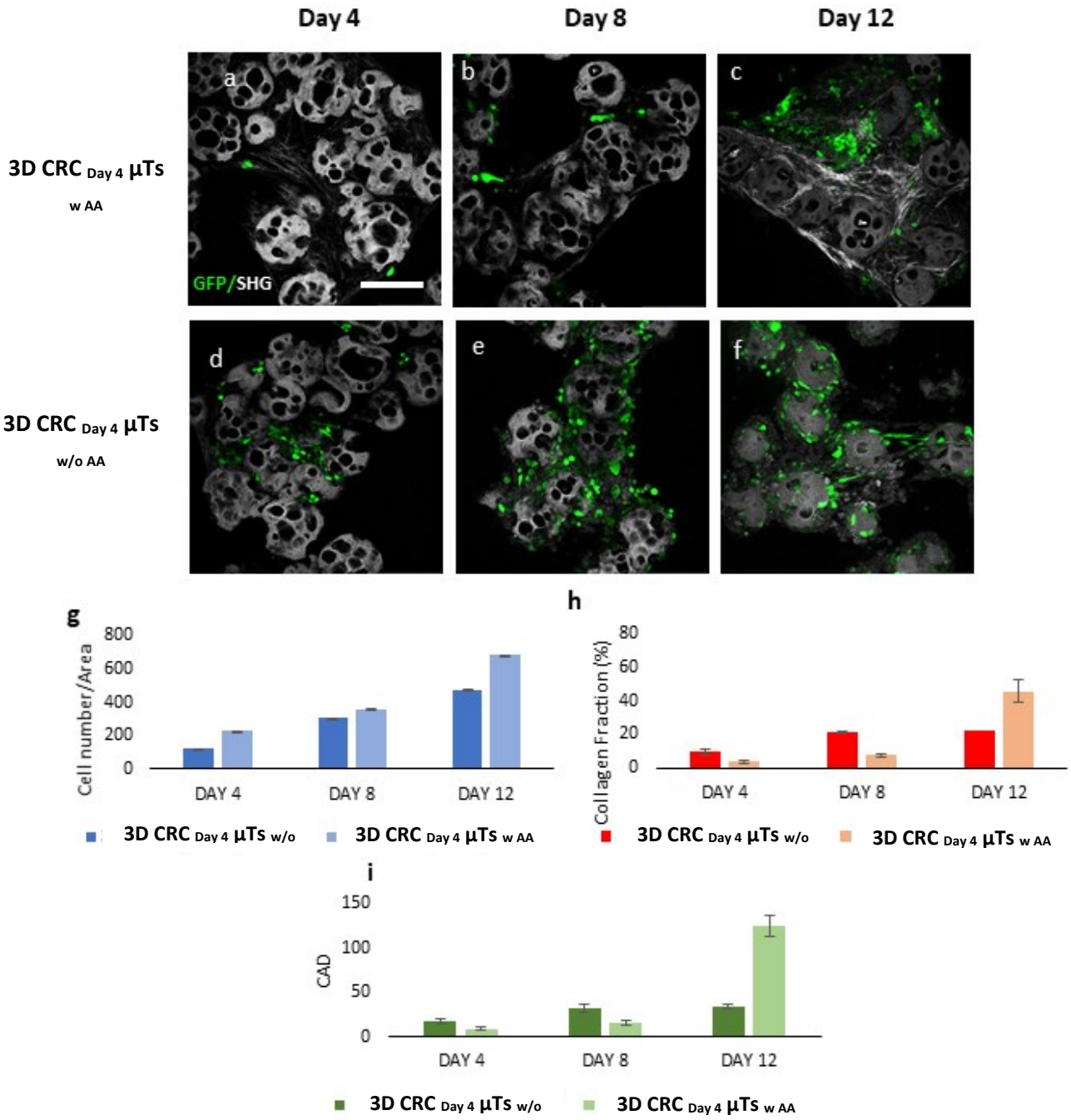

Figure 2.2 Morphology and cell distribution between 3D CRC $_{Day\ 4}$ µTs $_{w\ AA}$ and 3D $_{Day\ 4}$ CRC µTs $_{w/o\ AA}$ at different culture times (4, 8, and 12 Days). Confocal images of GFP (green) signal revealing the dissemination of CRC cells (HCT-116 cells) into the ECM neo-formation, shown by the SHG signal,

scale bar 155 µm; Comparative analysis of HCT-116 cells proliferation (g), Collagen fraction (h), and Collagen assembly degree (i) between 3D CRC $_{Day\ 4}$ µTs $_{w\ AA}$ and 3D CRC $_{Day\ 4}$ µTs $_{w/o\ AA}$. All the experiments were performed in triplicate (n = 3), values represent the mean and the standard deviation (g) ($p * < 0.05$; $p ** < 0.05$).

Moreover, 3D CRC $_{Day\ 4}$ µTs $_{w\ AA}$ was compared with 3D HCT-116 µTs, considered as controls. The confocal images showed a low rate of tumor cell proliferation, displayed in 3D CRC $_{Day\ 4}$ µTs $_{w\ AA}$ at Day 4 and 8 (Fig. 2.3 a, b respectively), compared to 3D HCT-116 µTs (Fig. 2.3 d, e). Whereas the tumor cell proliferation was increased at Day 12 both 3D CRC $_{Day\ 4}$ µTs $_{w\ AA}$ (Fig. 2.3 c) and 3D HCT-116 µTs (Fig. 2.3 f). Cell proliferation graph (Fig. 2.3 j) displayed a linear increase of HCT-116 cell number in 3D CRC $_{Day\ 4}$ µTs $_{w\ AA}$ compared to 3D HCT-116 µTs in which the tumor cell proliferation kept constant over time. Concerning the ECM production, 3D CRC $_{Day\ 4}$ µTs $_{w\ AA}$ was compared with 3D NF µTs. Confocal images showed a significant increase of ECM production in 3D NFµTs from Day 4 to 12 (Fig. 2.3 g-i), compared to 3D CRC $_{Day\ 4}$ µTs $_{w\ AA}$ (Fig. 2.3 a-c), probably due to the continuous degradation of ECM by cancer cells, as shown in the graph of collagen fraction analysis (Fig. 2.3 k). In addition, CAD analysis described a linear increase of SHG signal in 3D NF µTs from Day 4 to 12, while a significant increase was shown in 3D CRC $_{Day\ 4}$ µTs $_{w\ AA}$ at Day 12, compared to Day 4 and 8 (Fig. 2.3 l). High intensity of SHG signal in 3D CRC $_{Day\ 4}$ µTs $_{w\ AA}$ could be due to the collagen fibers network that was well-assembled showing dense structures when cancer cells were in contact with ECM (Winkler, Abisoye-Ogunniyan et al. 2020). Finally, among the configurations of 3D CRC µTs produced, 3D CRC $_{Day\ 4}$ µTs $_{w\ AA}$ was the best and was used for several experiments.

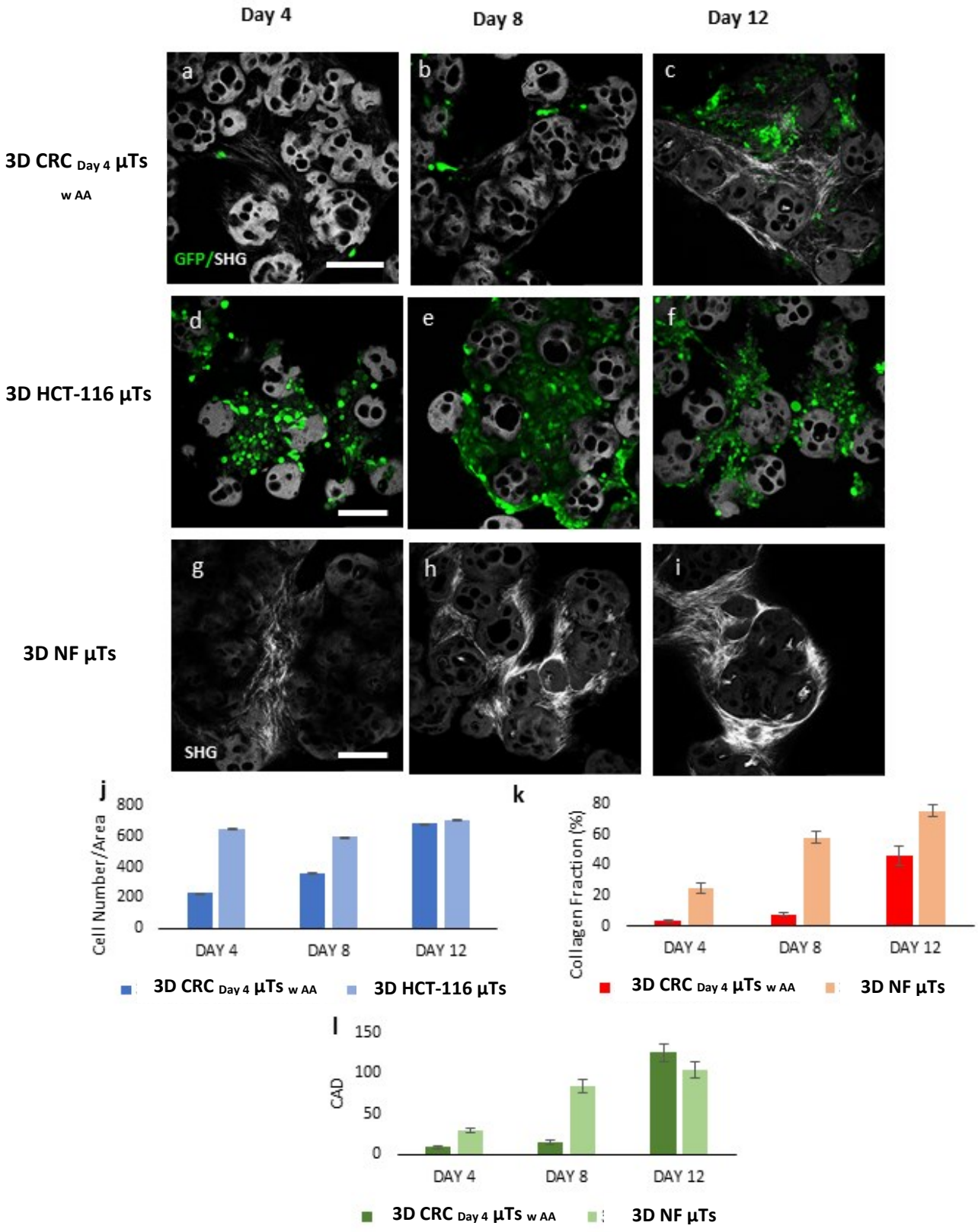

Figure 2.3 Morphology and cell distribution comparison of 3D CRC $_{Day\ 4}$ µTs $_{w\ AA}$ (a, d, g) with 3D HCT-116 µTs (b, e, h) and 3D NF µTs (c, f, i) at 4, 8 and 12 Days. Confocal images of GFP (green) signal revealing the dissemination of HCT-116 cells into the ECM neo-formation, shown by the SHG signal, scale bar 155 µm; Comparative analysis of HCT-116 cells proliferation between 3D CRC $_{Day\ 4}$ µTs $_{w\ AA}$ and 3D HCT-116 µTs (j); Comparative analysis of Collagen fraction (k) between and Collagen assembly degree (l) between 3D CRC $_{Day\ 4}$ µTs $_{w\ AA}$ and 3D NF µTs. All the experiments were

performed in triplicate (n = 3), values represent the mean and the standard deviation (g) (p ∗< 0.05; p ∗∗< 0.05).

2.3.2 Colorectal cancer cells action in ECM remodeling in 3D CRC µTs

The histological cross-sections stained with H/E showed a decrease of ECM in 3D CRC µTs at Day 12 (Fig. 2.4 a, b) compared with 3D NF µTs in which a complex, endogenously produced ECM was displayed (Fig. 2.4 c, d). H/E displayed a low amount of ECM in 3D CRC µTs due to continuous proteolytic action of cancer cells that induce ECM degradation promoting their invasion in other sites. In addition, some HCT-116 cells were embedded in the residual ECM, changing their shape from round (white arrows) to spindle (black arrows), as shown in Fig. 2.4 b. This changing in morphology is a topical event occurring during Epithelial-Mesenchymal Transition (EMT), a process that takes place in the first steps of cancer progression (Ribatti, Tamma et al. 2020).

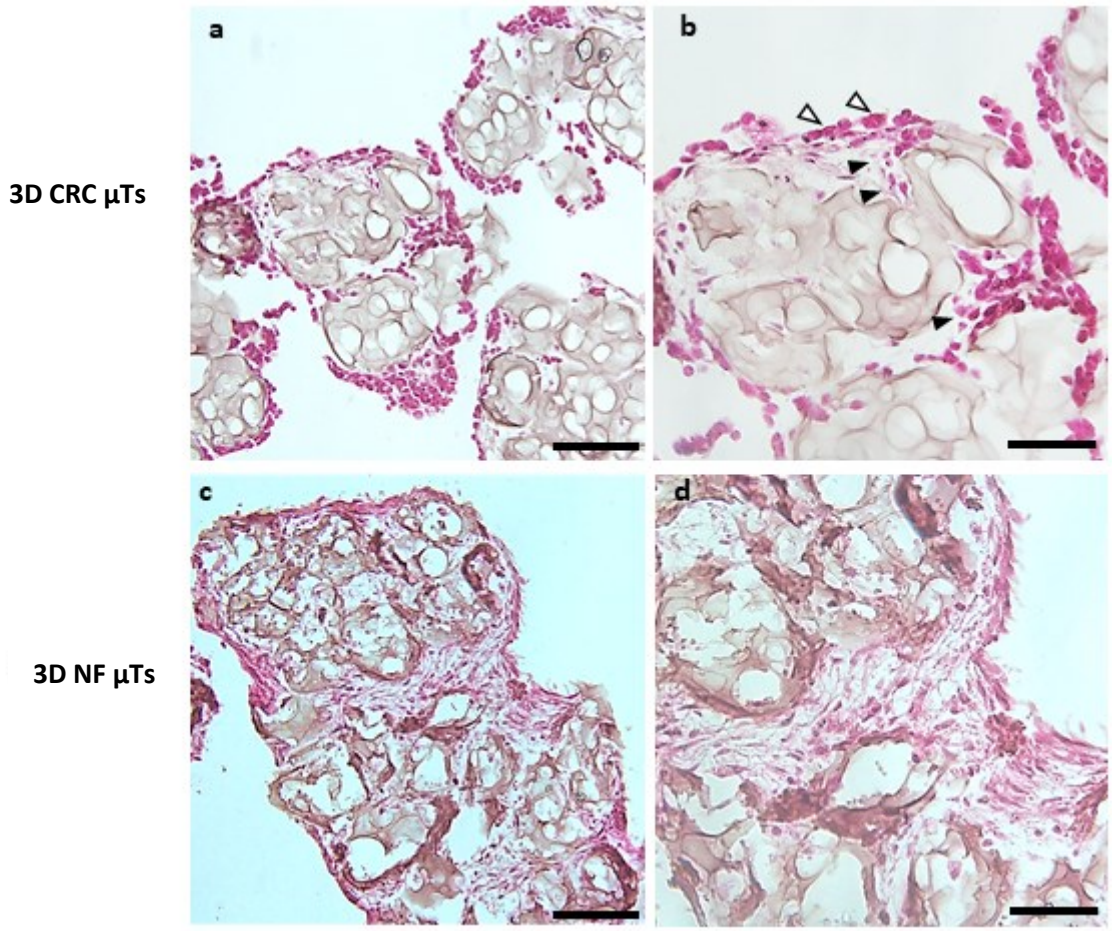

Figure 2.4 Histological features of 3D CRC µTs and 3D NF µTs at Day 12 of culture. An ECM remodeling was displayed in 3D CRC µTs (a) compared to 3D NF µTs (c); scale bar 100 µm. High magnification insets showed the ECM degraded by HCT-116 cells (b) compared to ECM of 3D NF µTs (d); White and black arrows indicated the change of HCT-116 cells from round to spindle shape when they invaded the ECM surrounding; scale bar 50 µm.

Moreover, we investigated the proteolytic action of cancer cells, shifting the focus towards Matrix Metalloproteinases (MMPs) expression. This specific group of proteolytic enzymes is involved in the ECM remodeling, degrading various cell adhesion molecules, thereby modulating cell–cell and cell–ECM interactions. Many studies have demonstrated that increased MMPs expression and activation are found in a variety of different cancers, promoting hallmarks of tumor progression including angiogenesis, invasion, and metastasis, and correlate with shortened survival (Said, Raufman et al. 2014). MMP-9, also named type IV collagenase or gelatinase B, is one of the key proteolytic enzymes in the breakdown and reconstruction of ECM in CRC invasion and metastasis (Jonsson, Hjalmarsson et al. 2018). From the pictures, we found high levels of MMP-9 expression in 3D CRC µTs (Fig. 2.5 c, e), compared with 3D NF µTs (Fig. 2.5 d, f) represented by a weak signal, as known in literature in which the MMP-9 expression is low or absent in normal quiescent tissues. Furthermore, we observed that the MMP-9 signal is localized in the cytoplasm in both fibroblasts and HCT-116 cells in 3D CRC µTs, especially in the cell protrusions of the plasma membrane (Fig.2.5 c, e white arrows for fibroblasts and yellow arrows for HCT-116 cells). This evidence is in line with previous studies that found the localization of MMP-9 to specialized cell surface structures, called 'invadopodia', to promote the cancer cells invasion. These structures represent the site where active ECM degradation takes place (Gialeli, Theocharis et al. 2011). All results show an increase of ECM remodeling in 3D CRC µTs, indicating the strong activity of cancer cells to degrade a variety of ECM macromolecules, facilitating their invasion and migration through the surrounding tissue.

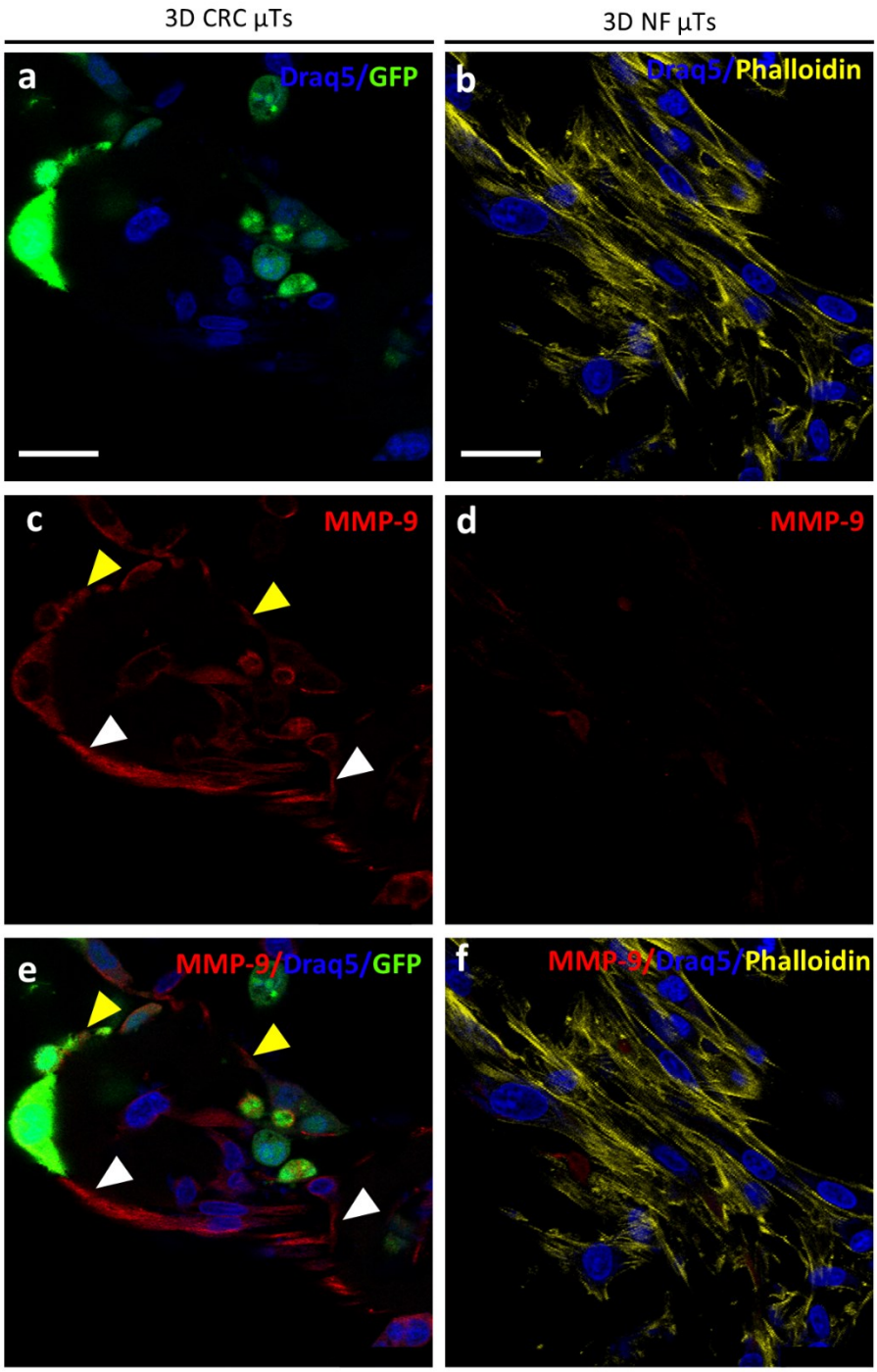

Figure 2.5 Marker for ECM remodeling in CRC: MMP9. High magnification insets show the expression level and location of MMP-9 in 3D CRC µTs (c) and 3D NF µTs (d) at Day 12. A strong signal of MMP-9 in 3D CRC µTs (c), unlike the 3D NF µTs (d). White and yellow arrows indicate the localization of MMP-9 in fibroblasts and HCT-116 cells in 3D CRC µTs (c, e). The nuclei of NF and HCT-116 cells are stained with Draq5 (blue) (a, b, e, f), HCT-116 cells expressed GFP signal (green) (a, e) and filamentous actin are stained with Phalloidin (yellow) (b and f); scale bar 50 µm.

2.3.3 Changes in morphology and organization of collagen fibers in 3D CRC µTs and 3D NF µTs

During cancer development and progression, a continuous ECM remodeling takes place: synthesis, degradation, changes in collagen fibers orientation, and interaction of cancer cells with collagen fibers. These changes supply a microenvironment that is favorable for the growth, migration, and polarization of cancer cells. It is known that Cancer-Associated Fibroblasts (CAF) modify the surrounding ECM, by generating ECM tracks or by applying mechanical pulling forces on collagen fibers that allow the collective cancer cell invasion. In our study, the image of 3D CRC µTs (Fig. 2.6 a) showed some areas in which HCT-116 cells preserved a significant alignment along the collagen fibers compared with 3D NF µTs (Fig. 2.6 b). In addition, the collagen fiber orientation analysis at 12 Day depicted a higher alignment of collagen fibers in 3D CRC µTs than in 3D NF µTs. It is well-known that cancer cells are also capable to remodel the ECM to generate regions of highly aligned collagen fibers (Taufalele, Vanderburgh et al. 2019). For this reason, to investigate the alignment degree between cancer cells and collagen fibers, 2D fast Fourier transforms (2D FFTs) were performed, calculating the relative orientation intensity in the frequency domain (Ayres, Jha et al. 2008). To quantify the alignment of cancer cells and collagen fibers, we plotted the FFT spectra of confocal images, represented by GFP signal expressed by cancer cells and Draq 5 signal by NFs, and SHG images, represented by collagen fibers. Moreover, 2D FFT was carried out using two regions of different sizes (Fig. 2.6 d-g) (described in section 2.2.4), to explore global alignment areas and high magnification images in which was analyzed specific areas showing cancer cells alignment along the collagen fibers. The plots of Fig. 2.6 d, e showed a significant alignment overlapping between NFs and collagen fibers (Fig. 2.6 d) in which three prominent peaks were evident at 90°, 180°, and 270°, differently from the HCT-116 cells and collagen fibers (Fig. 2.6 e) where a partial overlapping and a more random distribution of collagen fibers was found. On the contrary, the plots of Fig. 2.6 f, g showed partial overlapping between NFs and SHG signals (Fig. 2.6 f) indicating that a random distribution was present. Instead, an alignment between HCT-116 cells and collagen fibers was shown with a prominent peak observed at 180 °, indicating a preferential orientation of HCT-116 along the collagen fibers.

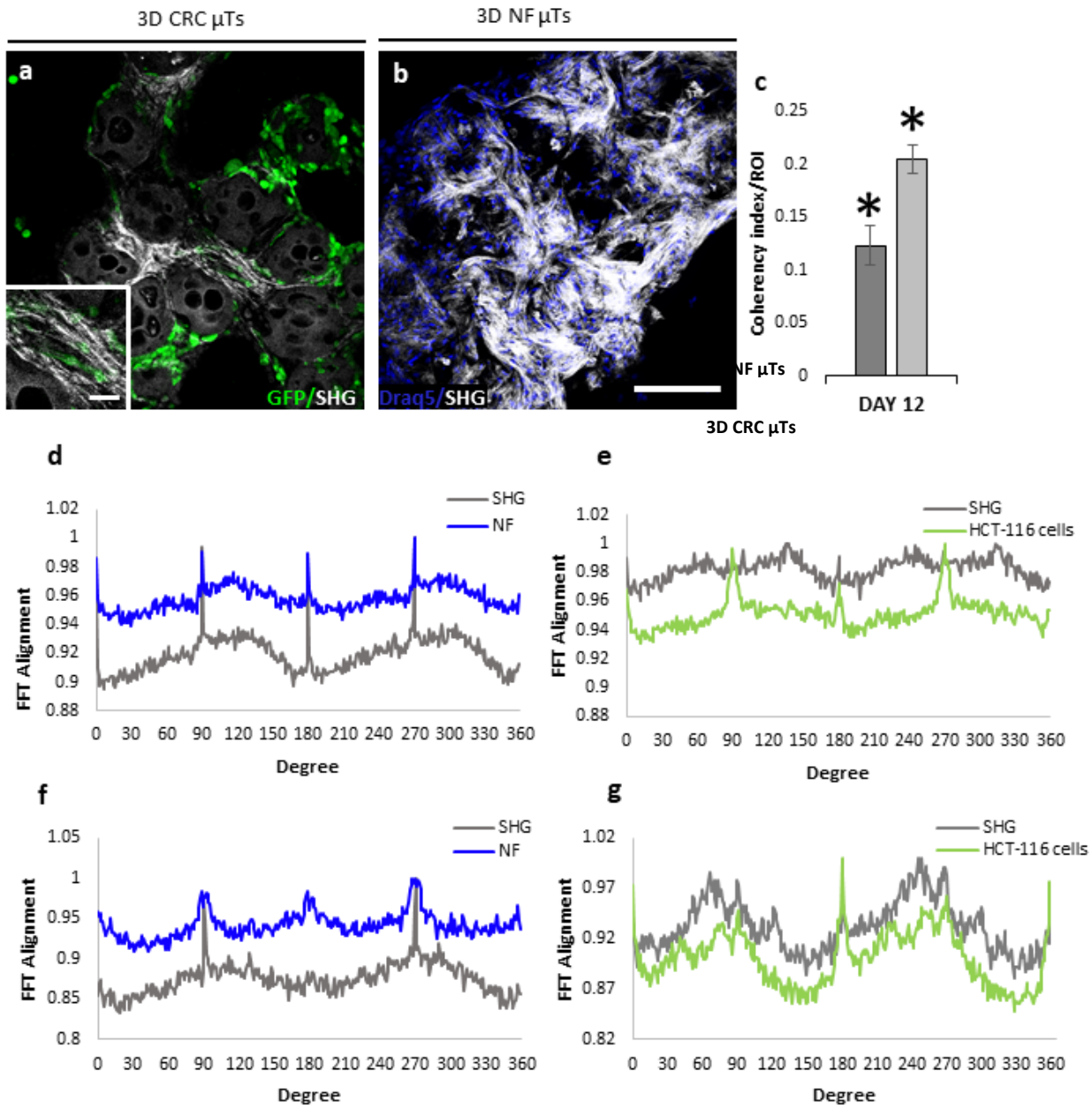

Figure 2.6 Collagen fiber Orientation analysis of 3D CRC µTs and 3D NF µTs at Day 12. Confocal images of HDF shown with Draq5 nuclear staining (blue) and HCT-116 cells expressing GFP (green) into the ECM neo-formation (SHG signal) (a and b, respectively), scale bar 155 µm; High magnification inset displays alignment of CRC cells along the collagen fibers (a). The graph shows the analysis of collagen fiber orientation of each sample (c). 2D FFT alignment plots are results of the summed pixel intensities for each radius along the corresponding angle of acquisition. 2D FFT transform of NFs (blue) or HCT-116 cells (green) and SHG signal (gray) using image size 1024x1024 pixels (d, e) and 256x256 (f, g). The shape and height of peaks of 2D FFT plots represent the relative degree of alignment, while the peak position corresponds to the principal axis of orientation for the fiber or cell. All the experiments were performed in triplicate (n = 3), values represent the mean and the standard deviation (g) (p ∗< 0.05; p ∗∗< 0.05).

2.3.4 Fibroblasts Reprogramming *in vitro*: activation of NFs into CAFs in 3D CRC µTs

Over the last years, it has been demonstrated that dynamic bidirectional crosstalk between cancer cells and the tumor microenvironment (TME) occurs and the key components of the TME, cancer-associated fibroblasts (CAF), play an important role in cancer progression and metastasis. During the cancer formation and progression, the activation of normal fibroblasts into CAFs occurs triggering several mechanisms that induce the malignant behavior of cancer cells. Among stromal markers used to detect CAFs, the most commonly used are α-Smooth muscle actin (αSMA) and Fibroblast activation protein-α (FAP α). In this perspective, we analyzed αSMA and FAP α markers using immunofluorescence. Our results indicated that the αSMA signal was distributed in the cytoplasm of fibroblasts and its signal was significantly higher in the 3D CRC µTs (Fig. 2.7 c, white arrow) compared with 3D NF µTs, in which the signal was almost non-existent (Fig. 2.7 d). Our results are in line with previous studies which highlighted the high expression of αSMA in stromal cells promoted CAF formation (Han, Liu et al. 2020). Moreover, we detected a strong signal of αSMA also in HCT-116 cells (Fig. 2.7 c) because they are able to acquire mesenchymal phenotype during progression and invasion, as seen also in previous studies (Ieda, Tazawa et al. 2019). Indeed, cancer cells that express αSMA are predicted to be the cells that have an invasive nature, tend to metastasize, and have a poorer prognosis (Anggorowati, Ratna Kurniasari et al. 2017). We further explored the FAPα expression in 3D CRC µTs (Fig. 2.8 a, c, e) and 3D NF µTs (Fig. 2.8 b, d, f). From the pictures, we observe a strong signal of FAPα in 3D CRC µTs (Fig. 2.8 c, e), compared with 3D NF µTs (Fig. 2.8 d, f). In detail, we can see that while the FAPα signal is shown in the cytoplasm of fibroblasts in 3D NF µTs, especially localized around the nuclei (Fig. 2.8 d white arrows), a stronger and more widespread signal of FAPα is displayed in both fibroblasts and HCT-116 cells in 3D CRC µTs (Fig. 2.8 c white arrows for fibroblasts, yellow arrows for HCT-116 cells). It is known that FAPα, a homodimeric integral membrane gelatinase of the serine protease family, is selectively expressed by CAFs in the stromal compartment (Yang, Lin et al. 2016). However, this gelatinase has been found in multiple epithelial cancer cell lines and is highly expressed in cancer cells, playing an important role in regulating cancer progression.

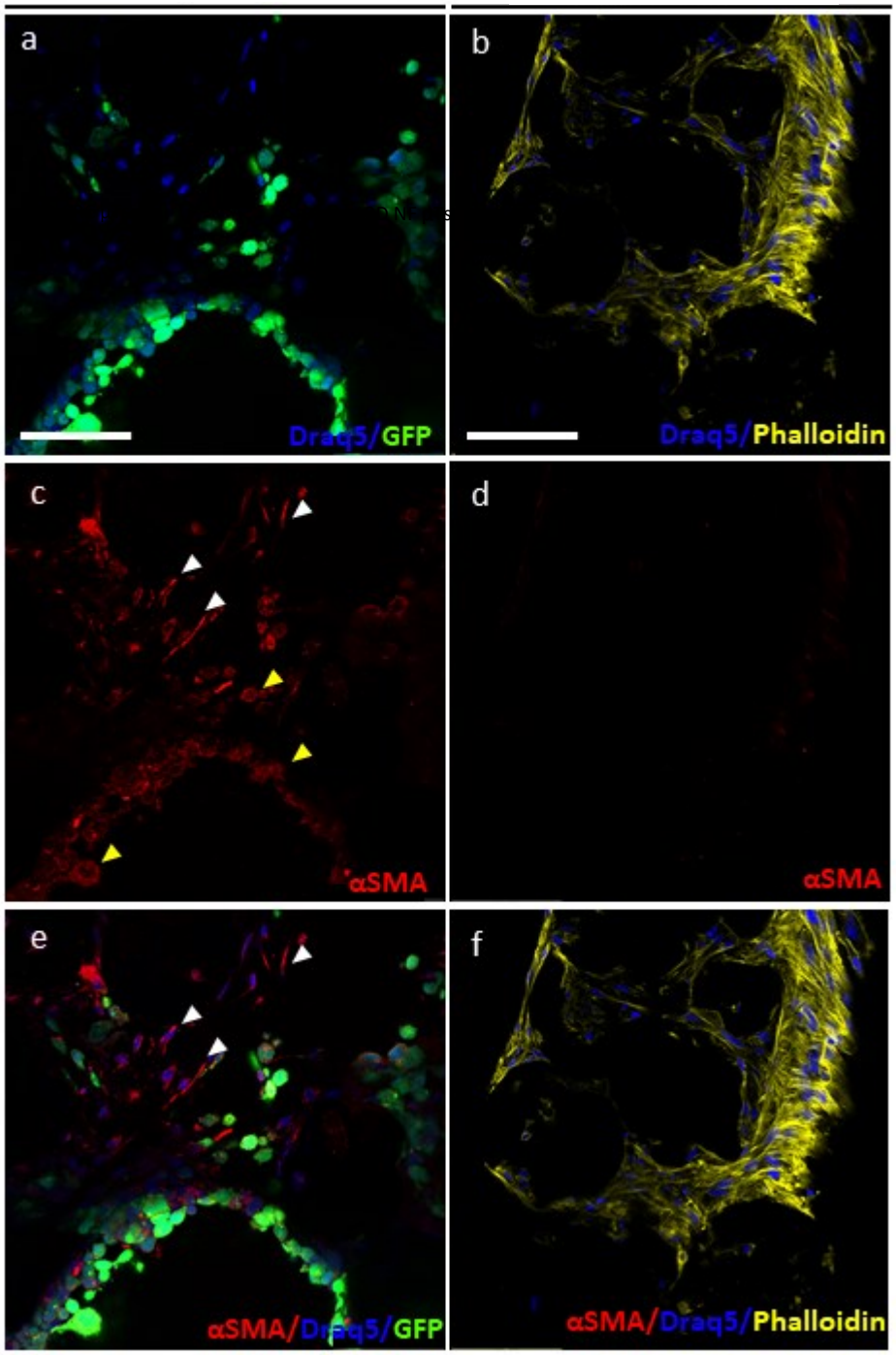

Figure 2.7 Markers for fibroblasts activation: αSMA. Immunofluorescence staining shows the expression level and location of α-SMA in 3D CRC µTs (c) and 3D NF µTs (d) at Day 12. In particular white arrows indicate a strong signal of αSMA coming from fibroblasts in 3D CRC µTs (c), unlike the 3D NF µTs (d). α-SMA was expressed also by HCT-116 cells, identified by yellow arrows (c). The nuclei of NF and HCT-116 cells are stained with Draq5 (blue) (a, b, e, f), HCT-116 cells expressed GFP signal (green) (a, e) and filamentous actin are stained with Phalloidin (yellow) (b and f); scale bar 50 µm.

Indeed, a previous study has confirmed that the upregulation of FAPα could enhance the migration and invasion of CRC cells and its expression increased with the development of tumor stage (Yuan,

Hu et al. 2021). Interestingly, we found that the FAPα signal is shown not only in the cytoplasm but also in the nuclei of fibroblasts and HCT-116 cells in 3D CRC µTs (Fig. 2.8 c white arrows for fibroblasts, yellow arrows for HCT-116 cells). The role of nuclear FAPα is still unclear, but it could be linked to the activation of several mechanisms underlying the cancer cell invasion and migration. This evidence is in line with the results of a previous study in which the nuclear signal of FAPα was found in CAF (Driesen, Hilkens et al. 2020). To further investigate the conversion of NFs into CAFs in 3D CRC µTs, the expression level of YAP-1 was investigated. It is well known in the literature that YAP-1 expression is upregulated within the nucleus of cancer epithelial cells, but its activation in the conversion of NFs into CAFs is not clear. Shen et al. observed that the YAP-1 expression was significantly up-regulated in the prostate cancer stroma (Pca) patients than in benign prostatic hyperplasia (BPH) patients and the number of CAFs increased with the increase of YAP-1 signal in Pca patients, demonstrating the key role of YAP-1 in the fibroblast activation in TME (Shen, Li et al. 2020). In this respect, immunofluorescence staining of YAP-1 expression was performed in 3D CRC µTs (Fig. 2.9 a, c, e) and 3D NF µTs (Fig. 2.9 b, d, f). We found a high nuclear expression of YAP1 in fibroblasts of 3D CRC µTs samples (Fig. 2.9 c, white arrows), compared to fibroblasts in 3D NF µTs, where a cytoplasmatic signal of YAP-1 was detected (Fig. 2.9 d, white arrows). Moreover, from the pictures we observed a nuclear signal of YAP-1 also in HCT-116 cells, confirming the critical role of YAP-1 in regulating the cell invasion, migration, survival, and EMT during metastasis (Yamaguchi and Taouk 2020) (Fig. 2.9 c, yellow arrows). Taken together, we observed many differences in expression of αSMA, FAPα, and YAP-1 between 3D CRC µTs and 3D NF µTs, suggesting that conversion of NF in activated fibroblasts took place within 3D CRC µTs.

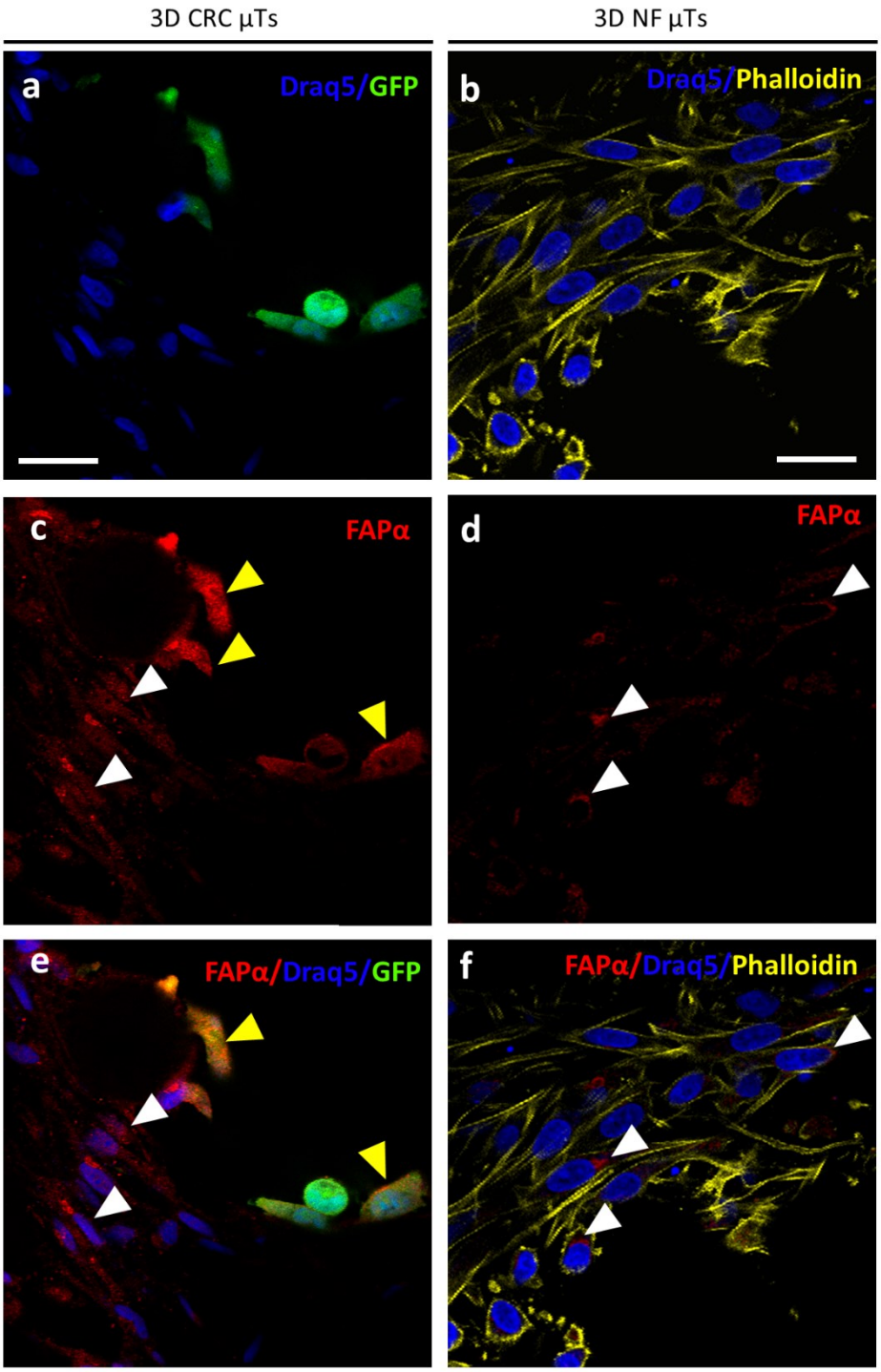

Figure 2.8 Markers for fibroblasts activation: FAPα. High magnification insets show the expression level and location of FAPα in 3D CRC µTs (c, e) and 3D NF µTs (d, f) at Day 12 of culture. White arrows indicate a strong cytoplasmic and nuclear signal of FAPα coming from fibroblasts in 3D CRC µTs (c, e), unlike the 3D NF µTs (d, f) in which the signal is localized only in the cytoplasm. FAPα was expressed also by HCT-116 cells, identified by yellow arrows (c, e). The nuclei of NF and HCT-116 cells are stained with Draq5 (blue) (a, b, e, f), HCT-116 cells expressed GFP signal (green) (a, e) and filamentous actin are stained with Phalloidin (yellow) (b and f); scale bar 50 µm.

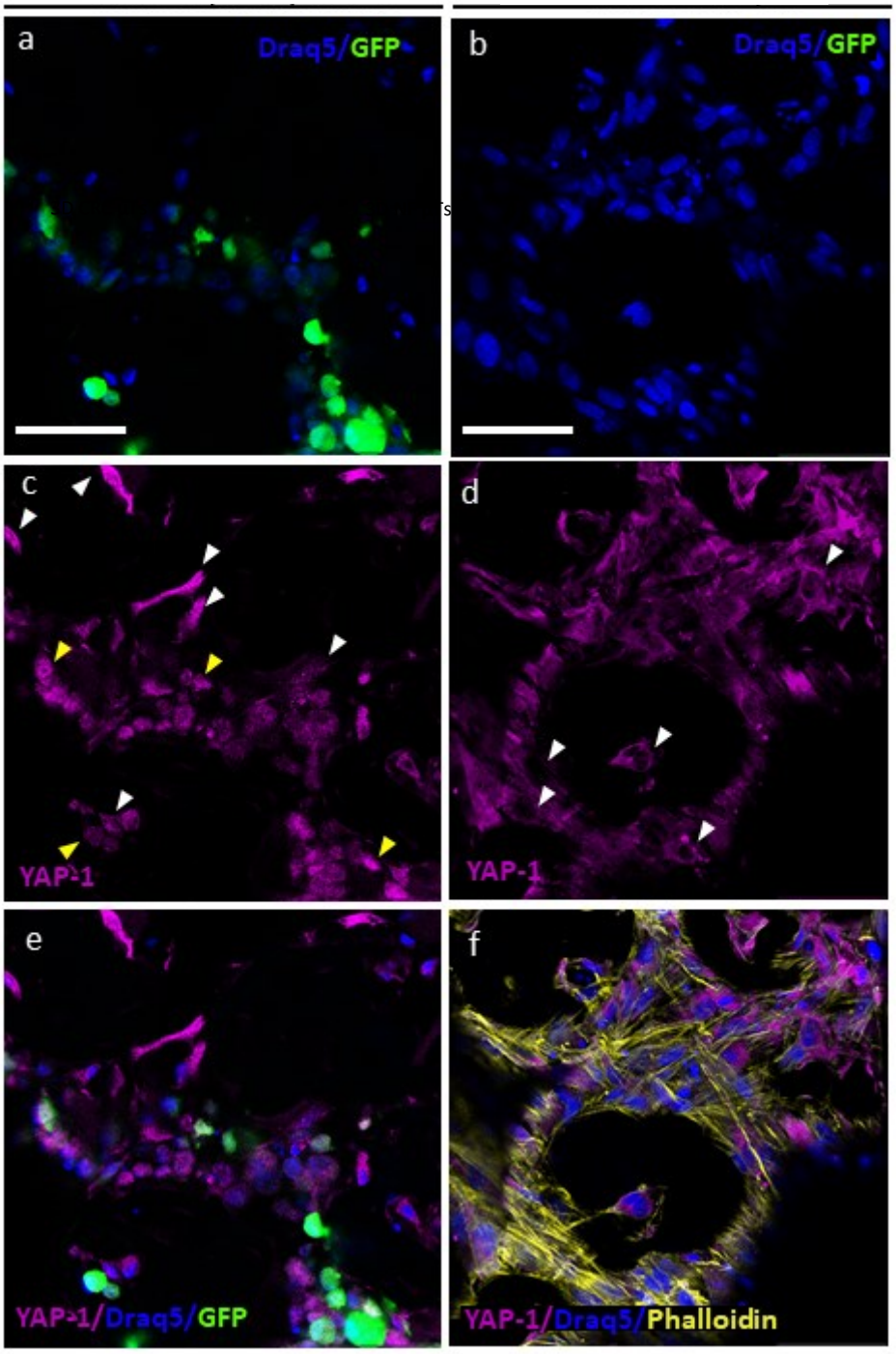

Figure 2.9 YAP-1 expression during fibroblasts activation. Immunofluorescence staining of YAP-1 expression in 3D CRC µTs and 3D NF µTs at Day 12. Images, acquired by a confocal microscope, display that the YAP-1 signal (magenta) is present more in the nucleus than in the cytoplasm in fibroblasts of 3D CRC µTs (c) compared to 3D NF µTs (d), showing the activation of fibroblast. White arrows display the signal location of YAP-1 in 3D CRC µTs (a) and 3D NF µTs (b). Yellow arrows display the YAP-1 expression also in HCT-116 cells (c, e). The nuclei of NF and HCT-116 cells are stained with Draq5 (blue) (a, b, e, f), HCT-116 cells expressed GFP signal (green) (a, e) and filamentous actin are stained with Phalloidin (yellow) (b and f); scale bar 50 µm.

2.3.5 Treatments with 5-FU and CT-NE-Curc on 3D NF µTs, 3D CRC µTs, and 3D HCT-116 µTs

The treatment with different concentrations of 5-FU on 3D CRC µTs and 3D NF µTs was performed for 24 h, 48 h, and 72h to observe the cytotoxic effect of the chemotherapeutic agent. The graphs show a strong reduction of cell viability in 3D CRC µTs in a dose-dependent manner after 24 h, 48 h, and 72h of treatment, differently from the 3D NF µTs in which a small reduction of cell viability was observed (Fig. 2.10 a, b, c orange, and blue bars, respectively). These results suggest a selective cytotoxic effect of 5-FU on cancer cells composing 3D tumor microtissues compared to 3D healthy microtissues (Imamura, Mukohara et al. 2015). Moreover, we observed that the high cell viability in 3D NF µTs kept constant after 24 h, 48 h, and 72 h, differently from the cell viability in 3D CRC µTs in which it decreased over time. In addition, 3D HCT-116 µTs, made only of cancer cells, were treated with the same concentrations of 5-FU to observe how the cancer cells respond to the cytotoxic effect of the chemotherapeutic agent. The results show the high cell viability in 3D HCT-116 µTs after 24 h, 48 h and 72h (Fig. 2.10 a, b, c gray bars), compared with 3D CRC µTs and 3D NF µTs, except for 1mM and 10 mM, in which cancer cells in 3D HCT-116 µTs show low cell viability after 72h. This is maybe because cancer cells tend to form tight junctions and make more difficult diffusion mechanisms as compared to cancer tissues including healthy cells such as 3D CRC µTs.

The combination treatment with CT-NE-Curc and 5-FU was carried out on 3D CRC µTs, 3D NF µTs, and 3D HCT-116 µTs. The graph shows that at 24 h (Fig. 2.10 d) the effect of CT-NE-Curc/cell medium (with no 5-FU) is low, whereas it strongly appears at 48 h (Fig. 2.10 e), probably due to a delayed action of the nanocarrier which is much larger as compared to a molecule such as 5-FU and it takes more time to penetrate in the µTs. Indeed, at 48 h CT-NE-Curc/cell medium shows an interesting selective behavior, that is not at all toxic towards 3D NF µTs but cytotoxic for 3D CRC µTs (Fig. 2.10 e). Regarding the combination of CT-NE-Curc/5-FU, the co-adjuvant and protective effect of curcumin in 3D NF µTs and 3D CRC µTs is particularly evident at 48 h (Fig. 2.10 e). For 3D HCT-116 µTs treated with CT-NE-Curc/cell medium, the cell viability was reduced compared with 3D CRC µTs and 3D NF µTs at 24 h (Fig. 2.10 d), but it increased after 48 h (Fig. 2.10 e). The same results were showed when 3D HCT-116 µTs were treated with CT-NE-Curc/5-FU, except for CT-NE-Curc/5-FU 10 mM. After 72h of treatments, 3D CRC µTs treated with CT-NE-Curc/cell medium have low cell viability, differently from 3D NF µTs and 3D HCT-116 µTs (Fig. 2.10 f). The same behavior was shown when 3D CRC µTs, 3D NF µTs, and 3D HCT-116 µTs were treated with CT-NE-Curc/5-FU 10 µM and 100 µM. Instead, the cell viability of 3D NF µTs result higher than in 3D HCT-116 µTs and 3D CRC µTs

when they were treated with CT-NE-Curc/5-FU 1 mM and 10 mM, probably due to the protective effect of curcumin in healthy cells (Fig. 2.10 f). However, the CT-NE-Curc/5-FU 1 mM and 10 mM combinations provoke almost 50% mortality rate in 3D NF µTs, differently from CT-NE-Curc/5-FU 10 µM and 100 µM combinations, probably result of the high concentrations of 5-FU which predominate over the protective effect of curcumin (Fig. 2.10 f). Taken together, we observed that the cell viability of 3D CRC µTs was reduced both treatments with 5-FU alone and CT-NE-Curc/5-FU combinations, suggesting a rapid 5-FU and CT-NE-Curc penetration and diffusion which might be possible due to the greater intercellular space between cells, caused by cancer cells and activated fibroblasts which overexpress and secrete proteases which are capable of degrading the ECM components (Brancato, Gioiella et al. 2017). On the contrary, 3D NF µTs show a more complex and intact ECM with a slow remodeling, in which the drug penetration is more difficult within a microtissue as compared to direct contact with cells as in the case of a 2D culture where the selectivity of the 5-FU was less evident. In the same way, the high cell viability in 3D HCT-116 µTs, treated with 5-FU alone and in combination with CT-NE-Curc, might also be due to the microtissues structure and organization. Indeed, it is known that cancer cells are more proliferative and divide and grow over each other in an uncontrolled manner even when in contact with neighboring cells. This property, known as contact inhibition of proliferation, allows the cancer cells to form more tight junctions which could block the diffusion of the chemotherapeutic agent to the outer layers in which cells are more proliferative and therefore more sensible to 5-FU treatment (Brancato, Gioiella et al. 2018). Despite some of the traditionally administered chemotherapy drugs, like 5-FU, have high proliferative cells as targets, cancer cells develop resistance to anti-cancer drugs, that if from one side can internalize the drug, on the other they over-express efflux pump proteins that make the cells resistant to the treatment, flushing out drugs (Wu, Yang et al. 2014). In addition, we suggest that 3D HCT-116 µTs are not able to recapitulate the complexity of tumor *in vivo*, because of the formation of cancer cell aggregates which are not physiological and, therefore truthful, unless the highest two concentrations of 5 FU, that are toxic for 3D NF µTs. Indeed, it is well known that tumor *in vivo* is not merely an aggregation of cancer cells but a complex entity in which cancer cells interplay with stroma cells and ECM and together contribute to cancer progression (Bissell and Radisky 2001).

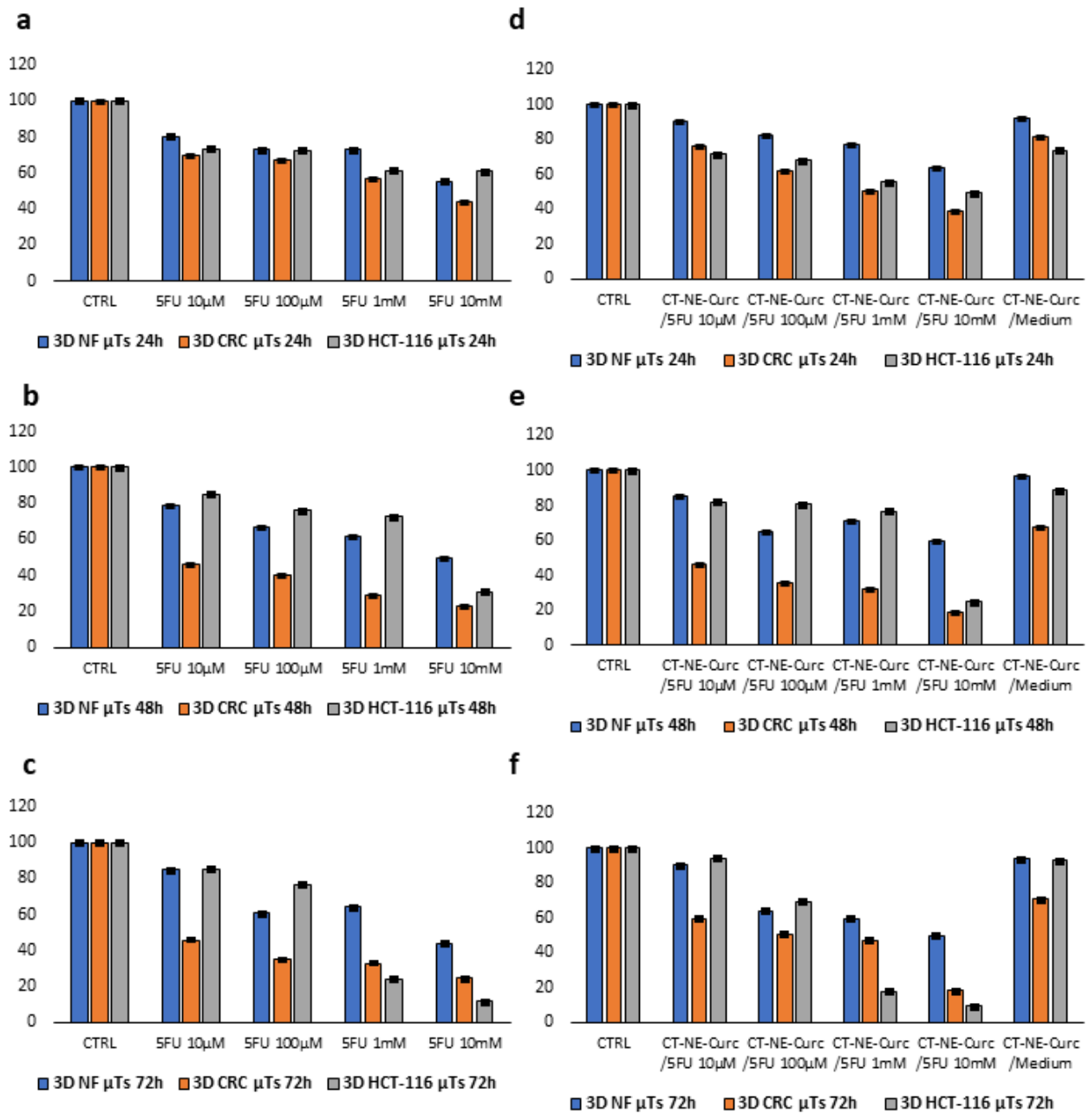

Figure 2.10 Cell Viability assay on 3D CRC µTs and 3D NF µTs treated with 5-FU alone and combination CT-NE-Curc and 5-FU. The graphs of treatments with different concentrations of 5-FU at 24h, 48h, and 72h (a, b, c); The graphs of combination treatments with CT-NE-Curc and different concentrations of 5-FU at 24h, 48h, and 72h (d, e, f). All the experiments were performed in triplicate (n = 3), values represent the mean and the standard deviation (g) ($p * < 0.05$; $p ** < 0.05$).

2.4 Conclusion and Future Perspectives

In this work, 3D Colorectal cancer microtissues (mono-cultures and co-cultures 3D CRC µTs) were fabricated to develop 3D CRC models that reproduce faithfully the TME, essential for the cancer growth, progression and metastasis process. Several configurations of 3D CRC µTs were fabricated

and different behaviors in terms of ECM remodeling and dynamic bidirectional crosstalk between cancer cells and TME were detected. We demonstrated that the ECM within 3D CRC µTs was modeled and modified in presence of cancer cells, compared to 3D NF µTs, favoring the formation of preferential routes for invasion and migration through the surrounding ECM. In addition, we observed the high expression of some stromal markers, αSMA, and FAPα, and the high frequency of nuclear localization of YAP-1 for the fibroblast activation in 3D CRC µTs, compared with 3D NF µTs, demonstrating that our *in vitro* 3D CRC models reproduced the transformation of normal fibroblasts in activated fibroblasts. Although the fibroblasts used to develop 3D CRC µTs are not tissue-specific, however, the results proved promising, and these could be a starting point to fabricate 3D CRC models with human primary intestinal fibroblasts, reproducing even more faithfully the native tissue. We can conclude that a 3D model of cancer tissue to be appropriate as a drug screening platform need to include cancer cells in their own environment which involves extracellular matrix as well as healthy cells. This is paramount to get more realistic permeability properties and better mimic the right diffusion of free drugs as well as nanoencapsulated drugs. We can also conclude looking at the results at 72 h that the two highest concentrations of 5-FU are not appropriate since they also kill almost 50% of the cells of the healthy 3D NF µTs. Therefore, we expect that the best formulation is a combination of CT-NE-Curc and 5-FU at a concentration to be searched in the range of 10 and 100 µM. However, since the 3D HCT-116 µTs cannot be representative of the cancer cell contribution, the final evaluation needs to be carried out within the 3D CRC µTs analyzing the evolution of the ratio between healthy and cancer cells upon the treatment to select the right formulation. For this reason, image analyses are underway to study how the ratio of healthy cells to cancer cells changes in the absence and the presence of curcumin at 10 and 100 µM of 5-FU. We expect that thanks to the selectivity of curcumin the ratio of healthy cells to cancer cells increases when the curcumin treatment is carried out, compared to treatment in the absence of curcumin. Understanding which of the two concentrations of 5-FU is most suitable for combination with curcumin is crucial to establish the best treatment against CRC, which, on one hand, improves the therapeutic efficacy and the other hand reduces the toxicity of 5-FU.

3. Metastasis-on-chip platform for investigating the Colorectal Cancer Liver metastasis

3.1 Introduction

Metastasis is a complex process still not well understood. In detail, several scientists scarcely know the mechanisms underlying the activation of tumor cell growth and malignancy, how these mechanisms affect the formation of spontaneous metastasis and the role that the TME plays in regulating these relevant mechanisms (Skardal, Devarasetty et al. 2016). Therefore, a greater understanding of these mechanisms at the base of the metastatic process is the pivotal objective of many researchers and clinicians. In recent years, with rapid advancements in multi-organ-on-a-chip technologies, it has been possible to create new platforms that reproduce the *in vivo* dynamic conditions and metastasis process (Ruiz-Espigares, Nieto et al. 2021). Recently, the combination of tissue engineering strategies and micro-scale systems has resulted in a potential tool to understand several phenomena and events involved in cancer metastasis improving our capacity to predict and control cancer progression. As previously reported, Metastasis-on-a-chip (MOC) models can include two or more separated compartments to resemble the crucial cross organ-communication between two specific organs (Skardal, Devarasetty et al. 2016) or more organs (Aleman and Skardal 2019), in which cancer cells migrated and colonization predominant target sites. Although these MOC platforms reproduce cancer cells migration from the primary tumor site towards the predominant target sites, however, the architecture of organoids formed by cell encapsulation in the hydrogel is more simplistic and is not suitable to recapitulate organ-specific extracellular matrix (ECM) *in vivo*-like function. Indeed, it is widely accepted that ECM remodeling is one of the key events occurring in the TME, therefore the presence of endogenous and responsive ECM allows the study of the tumor progression and metastatic events in a more relevant *in vitro* context. Moreover, it is also known that the metastatic niche is a complex environment that co-evolves with cancer cells. In this perspective, other MOC platforms mimic the progression of metastatic cancer using a decellularized matrix to resemble a complex and endogenous ECM (Wang, Wu et al. 2020). Although in these MOC systems, cancer cells were incorporated in a natural acellular matrix that exhibited similar mechanical stiffness to that of the native tissue, nonetheless they did not faithfully recapitulate the cancer progression existing *in vivo* owing to the use of the animal ECM rather than human ECM. In this thesis, I develop 3D *in vitro* models of the primary tumor site and target organ that reproduce faithfully *in vitro* the organization, structure, and cellular component of the TME, and I exploit the multi-organ-on-a-chip technology to investigate the hepatic metastasis from colorectal cancer including cell invasion, migration, and colonization of the target organ. The fabrication of 3D

Colorectal Cancer microtissues (3D CRC µTs) and 3D Target Organ microtissue (3D HepG2 µTs) is detailed in chapter 2. Briefly, the 3D CRC µTs are composed of an engineered system in which Normal Fibroblasts (NF) are continuously engaged in synthesizing, assembling, and disassembling their own ECM. Preliminary findings of cancer cells migration and colonization in the target organ were observed by using transwell inserts in order to carry out the pilot studies on cell migration times. Then, an optically accessible microfluidic chip was fabricated in order to host in the two separated chambers, primary tumor, and target organ respectively. A computational fluid dynamic simulation was performed in order to establish the fluid dynamic regime to guarantee cells survival in the chip. By coupling 3d tumor microtissues with microfluidic technology, I succeeded in detecting in real time the modification occurring at ECM level and the cancer cells invasion, migration, and colonization towards target organ via confocal and multiphoton microscopy.

3.2 Materials and methods

3.2.1 3D Microtissues (3D µTs) fabrication

Cell types

Normal Human Dermal Fibroblasts (NFs) were extracted from healthy biopsies and cultured in Eagle's Minimum Essential Medium (EMEM, Biowest) supplemented with 20% Fetal Bovine Serum (FBS, Sigma Aldrich), 200 mM L-Glutamine (Sigma Aldrich), 100 IU ml $^{-1}$ Streptomycin/Penicillin (Himedia), 100X Non-Essential Amino Acid (Euroclone).

Human colorectal carcinoma cell line (HCT-116 cells), transfected with pLVX-ZsGreen1-N1 (λex 493 nm, λem 505 nm) viral vector purchased from Clontech (USA), as indicated in (DOI: 10.1016/j.actbio.2016.11.072) and growth in Dulbecco's Modified Eagle's Medium (DMEM, Microgem) supplemented with 10% FBS (Sigma Aldrich), 200 mM L-Glutamine (Himedia), 100 IU ml $^{-1}$ Streptomycin/Penicillin (Himedia).

Hepatocellular carcinoma cell line (HepG2), with differentiated cells with epithelial-like phenotype, was purchased by ATCC and cultured in Minimum Essential Medium Earle's Salt (MEM, Biowest), containing 10% FBS, 200 mM L-Glutamine (Himedia), 100 IU ml −1 Streptomycin/Penicillin (Himedia), 0.1mM Non-Essential Amino Acid and 0.1mM Sodium pyruvate. The seeding density was 12 500 cells/cm2. HepG2 cells were sub-cultured every other Day thereafter using Trypsin/EDTA

0.05% (Himedia) and centrifuge at 1000 rpm for 5 min. The change of culture medium was every 2 Days.

The microtissues used to reproduce metastasis-on-a-chip were 3D CRC µTs, to simulate the primary tumor, and 3D Target Organ microtissues (3D HepG2 µTs), to simulate the secondary tumor. In addition, 3D mono-cultured Stroma microtissues (3D NF µTs) were produced and loaded into the microfluidic platform as control of 3D CRC µTs in the absence of colon cancer cells. For 3D CRC µTs and 3D NF µTs production, different culture conditions in parallel were performed by seeding cells on gelatin porous microbeads (GPMs), as previously reported in section 2.2.3.

Microscaffolds production

The gelatin porous microbeads (GPMs) were produced by following a previously established protocol and described also in paragraph 2.2.2. Before using, GPMs were sterilized in 100% Ethanol for 24 h on a rotating plate. Then, ethanol was removed, and the microbeads were washed 4 times in sterile phosphate-buffered saline (PBS) without calcium and magnesium solution for 30 min on a rotating plate and let it settle by placing the tube vertically for 30 min. After that, before cell seeding, PBS was replaced with fresh culture medium and stored at 4°C.

3D Colorectal cancer microtissue (3D CRC µTs) fabrication

For primary tumor production, a co-cultured Colorectal Cancer microtissues (3D CRC µTs), containing stromal and epithelial cells, was fabricated. In brief, 24 mg of GPMs were loaded with NF (20 cell/microbeads ratio) and cultured in 6-well Clear Flat Bottom Ultra-Low Attachment Multiple Well Plates (Corning ® Costar ®) with an intermittent stirring regime (30 min at 0 rpm, 5 min at 30 rpm) for 6 h to produce 3D Stromal microtissues (3D NF µTs). Then, dynamic cultures were kept under continuous stirring at 80 rpm for up to 12 days. Then, HCT-116 cells (10 cell/microbeads ratio) were seeded on 3D NF µTs at day 4 at a ratio 1:2 (HCT-116: NF). The culture medium was changed on the first day and every 3 days until the end of the experiments and acid ascorbic 50 µg/ml was added until Day 12. Then, 3D CRC µTs or 3D NF µTs were loaded into the microfluidic device on Day 6 of the culture. All cultures were maintained at 37°C in a humidified 5% CO2 incubator.

3D Target Organ microtissue (3D HepG2 µTs)

For Target Organ production, 35 mg of GPMs were loaded with HepG2 cells (30 cell/microbeads ratio). To promote HepG2 cells seeding on GPMs, an intermittent stirring regime (30 min at 0 rpm, 5min at 30 rpm) was applied for 24 h and then a continuous rotation at 20 rpm was applied for up to 5-7 days. The culture medium was changed three times per week. All cultures were maintained at 37°C in a humidified 5% CO2 incubator.

3.2.2 *In vitro* Colon cancer Cell Migration with Transwell insert in the presence and the absence of Target Organ

To investigate the capability of the colon cancer cells (HCT-116 cells) migration and invasion in the presence or the absence of Target Organ, 3D CRC µTs and 3D HepG2 µTs were fabricated and cultured into the ultra-low attachment well plates under stirring condition until Day 6. For the experiment with or without Target Organ, 3D CRC µTs were accommodated in the apical side of transwell 6.5 mm insert with 3 µm pore polyester membrane (Constar, Corning), integrating the medium cell (DMEM high glucose with 10% FBS, 200 mM L-Glutamine, 100 IU ml $^{-1}$ Streptomycin/Penicillin) both in the apical and basal chamber of transwell insert (Day 0). For experiment without Target Organ, transwell insert was observed by Confocal Fluorescence Microscope on Day 2. To observe the migration of HCT-116 cells, the microporous membrane of the transwell was fixed in 4% PAF at day 6, washed two times with phosphate-buffered saline (PBS), and incubated with the permeabilizing solution (PBS-Triton X-100 0.2%) for 10 min. Then, Alexa Fluor™ 555 Phalloidin staining at 1:1000 dilution for 30 min at RT was carried out. The GFP expression in HCT-116 was preserved after the fixing procedure. Images were obtained using a confocal laser scanning microscopy (CLSM) (λex= 555/565, λem= 567/588) and Z-stack series was performed to observe the cancer cells migration from the upper to the lower side of the porous polyester membrane. For the experiment with Target Organ, 3D HepG2 µTs were housed in the basal chamber of the transwell insert, and the cell migration was monitored until the tumor cells have migrated to the basal side (1 week).

3.2.3 Metastasis-on-chip devices Design and fabrication (MET-on chip)

To reproduce and investigate the metastasis process from CRC to Liver, a miniaturized and optically accessible microfluidic system was performed with the help of Computer-aided design (CAD) software. Two designs of MET-on-chip devices were fabricated that differ for the configuration of the channels for the medium supplement to the primary tumor and target organ. Both device configurations consisted of 2 chambers that allow the culture of 3D CRC µTs (primary tumor chamber) and 3D HepG2 µTs (target organ chamber), respectively. The two chambers were separated by pillars (0.3 x 0.3 x 0.3 mm^3).

First configuration (Fig. 3.1 a): The size of primary tumor chamber was 1,8 (length) x 1,650 (width) x 0,3 (depth) mm^3, while those of target organ were 2 x 2 x 0.3 mm^3. Moreover, the two chambers were provided by dedicated channels for µTs loading (primary tumor chamber: 3 x 0,7 x 0,3 mm3) and (Target organ chamber: 2,8 x 0,5 x 0,3 mm^3), respectively. Two lateral channels (2,5 x 0,5 x 0,3 mm^3) were inserted in order to guarantee a cross-flow of the nutrients supply to the primary tumor chamber. Furthermore, a diffusive channel (2,5 x 0,5 x 0,3 mm^3) allowed the flowing of the culture medium, thus guaranteeing the nutrients supply to the Target Organ from which waste removal.

Second configuration (Fig. 3.1 b): The size of primary tumor chamber was 1,37 (length) x 1 (width) x 0,3 (depth) mm^3, while those of target organ were (9,5 x 9,7 x 0,3 mm^3). Moreover, the two chambers were provided by dedicated channels for µTs loading (primary tumor chamber: 3 x 0,7 x 0,3 mm3) and (Target organ chamber: 3,1 x 0,7 x 0,3 mm^3), respectively. Two inlet channels (5,6 x 0,6 x 0,3 mm^3) and two outlet channels (5,6 x 0,6 x 0,3 mm^3) were inserted in order to guarantee a cross-flow of the nutrients supply from the primary tumour chamber to Target Organ chamber.

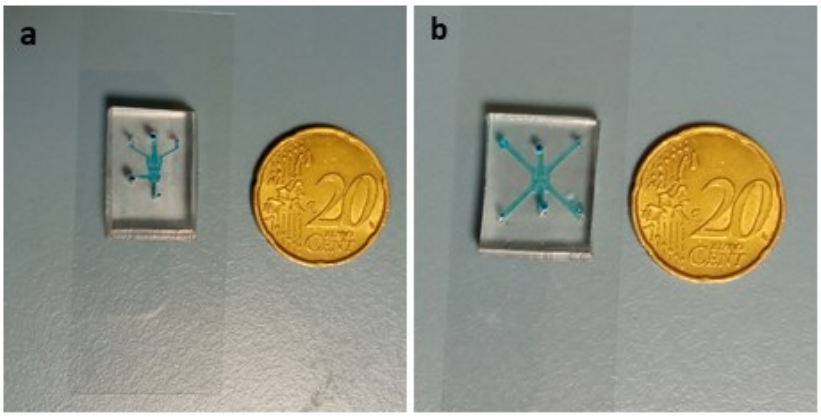

Figure 3.1 Two configurations of MET-on-a-chip platforms. First configuration (a) and Second configuration (b).

To fabricate the microfluidic device, the CAD file was converted into a Computer-Aided Machine (CAM) file using DESKAM software. Afterward, a replica molding of polydimethylsiloxane (PDMS) (Sylgard 184, Mascherpa), from a Poly (methyl methacrylate) (PMMA, Goodfellow) slab was produced by a micromilling machine (Minitech CNC Mini-Mill). PDMS base and curing agent were mixed using a weight ratio 10:1 and were poured on the PMMA master. Then, the PMMA master with the blend was degassed under vacuum for 1 hour to remove the air bubbles and cured in an oven for 40 min at 80°C. Then, the PDMS layer was softly detached from the PMMA master and, inlets and outlet holes were shaped using the biopsy punch (DifaCooper) with a 1 mm for medium channels and a 1,5 mm for µTPs loading channels. After punching, the PDMS layer was bonded on a coverslip (Menzel-Glaser 24 x 60 mm # 1,5) by oxygen plasma treatment for 1 min at 50 W in an oxygen plasma oven (Plasma Femto, Diener). Further, the device was placed in an oven and maintained at 80°C for 1 hour with the small metal weights resting on it to strengthen the bond.

3.2.4 CFD Simulation

To define the experimental setup, the three-dimensional velocity, the oxygen, and pressure gradients of the MET-on-a-chip platforms were performed before *in vitro* trial by using the COMSOL Multiphysics version 5.6 (build 280) in order to define the velocity and the oxygen concentration profile during the perfusion culture. The simulations were carried out as described in (Corrado, De Gregorio et al. 2019, Scognamiglio 2020) by modifying several parameters. Briefly, the devices were divided into two different domains as shown in Fig. 3.2, a fluid domain indicated with “f”, which identified the regions filled with culture medium, and microtissue domains, indicated with “µTs”, which identified the regions filled with 3D CRC µTs and 3D HepG2 µTs. Free and Porous Media Flow and Transport of Diluted Species in Porous Media models were set up in steady-state conditions, considering different boundaries and initial conditions. Again, as reported in two references, µTs properties were manually set up considering previous knowledge of the research group.

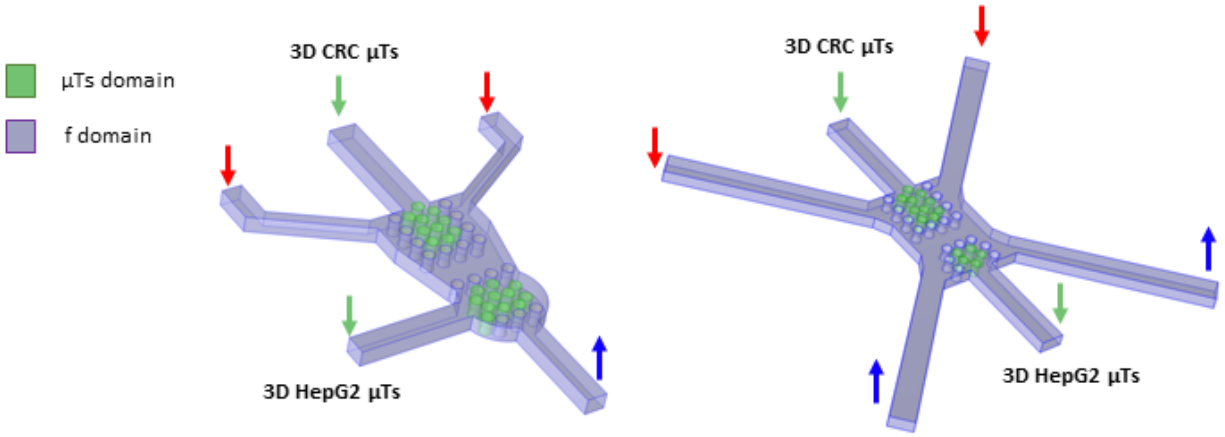

Figure 3.2 CFD Images of first configuration (left) and second configuration (right) of MET-on-a-chip. Medium's domain (domain "f" of the fluid) is highlighted in violet and microtissue's domains (domain "µTs"), highlighted in green. Inlet and outlet of medium indicated with red and blue arrows respectively. Inlet of microtissues loading indicated with green arrows.

3.2.5 Metastasis-on-chip (MET-on chip) assembling

MET-on chip was sterilized by 70% (v/v) ethanol for 30 min, then rinsed in PBS sterile, supplemented with 2% of penicillin/streptomycin, to remove residual ethanol and placed under UV light overnight. Tygon tubes (0.89mm ID) and connectors were sterilized in an autoclave and then, inserted into the inlets and outlet of the side channels using Polyethylene Tubing (0.58 ID x 0.97 OD mm) male and barbed female Luer lock connectors (Harvard Apparatus), previously sterilized. The tube of the inlet was split into two tubes using Y connectors (Harvard apparatus) to guarantee the same medium supply in both channels. Before starting the experimental phase, the devices were flushed with preheated medium to minimize bubble formation. In detail, a 5 ml syringe filled with the medium was connected to the inlets in order to fill the channels with medium and the whole system was incubated at 37°C in a humidified atmosphere with 5% CO_2 for 30 min.

3D CRC µTs and OT µTs Loading

Two experimental setups were performed:

1. Device with the presence of 3D CRC µTs in the chamber of the primary tumor without 3D HepG2 µTs in the chamber of Target Organ;
2. Device with the presence of both CRC µTs and 3D HepG2 µTs in the chambers.

Before the 3D µTs loading, the device was filled with culture medium and incubated at 37°C in a humidified 5% CO_2 incubator overnight to guarantee the microfluidic priming.

In the first experimental setup, 200 µL of 3D CRC µTs suspension were collected and injected into the loading inlet directly in the primary tumor chamber using a pipette-driven loading process. When 3D CRC-µTs suspension were injected in the primary tumor chamber, the outlet and inlet of the Target Organ chamber were left free. After 3D CRC µTs loaded, both inlets of the primary tumor and target organ chambers were closed with a 250 µm PDMS membrane (realized with spin coater 500 rpm for 30 s). The microfluidic device was observed online monitored by an inverted optical microscope for 24, 48, and 96h.

In the second experimental setup, 200 µL of 3D HepG2 µTs were collected and injected into the loading inlet of the Target Organ chamber, closing with a 250 µm PDMS membrane the inlet of the primary tumor chamber and keeping open the outlet, to avoid that 3D HepG2 µTs flowed in another chamber. Finally, the devices were connected to the syringe pumps (Harward Apparatus) to drive and control flow through microfluidic devices. A nominal flow rate of 2.0 µl/min was used to produce an average linear velocity like that of blood in tumors. The devices were placed inside a 37 °C incubator with 5% CO2 for 48 h. The microfluidic devices were online monitored by an inverted optical microscope (Leica) for 16h, 24, 96 h.

3D NF µTs Loading

3D NF µTs were loaded into the primary tumor chamber of the MET-on-a-chip platform by the appropriate loading inlet. Before the loading, the overnight microfluidic priming was carried out to set the device with culture medium at 37°C in a humidified 5% CO_2 incubator. After that, 200 µL of 3D NF µTs suspension were collected and injected into the loading inlet directly in the primary tumor chamber using a pipette-driven loading process, keeping the inlet of the Target Organ chamber free. Then, both inlets of the primary tumor and target organ chambers were closed with a 250 µm PDMS membrane. The microfluidic device was observed online monitored by an inverted optical microscope for 24, 48, and 96h.

3.2.6 In situ Online monitoring of CRC cell migration in MET-on chip devices

Experimental set up for online monitoring

MET-on chip was placed in an appropriate insert of the TCS SP5 MP Scanning confocal microscope (Leica) which is connected to the touch screen interface OKO-TOUCH (Oko-lab) regulating both temperature (37°C), gas (5% CO_2) and humidity (around 95%). A syringe pump was connected and placed outside the incubation system to reproduce a dynamic condition. In addition, a homemade PMMA adapter was produced using a micromilling machine (Minitech CNC Mini-Mill) with a size 24 x 60 mm and used to accommodate the device inside the insert of the confocal microscope. The objective used was 10x and two channels for Alexa Fluor 488 and Brightfield were set.

In situ Online monitoring of CRC cell migration in MET-on chip without Target Organ

Online monitoring of CRC cells migration was carried out using Time-lapse imaging with a time interval of 1 h, stacks 25 and 15 step numbers of Z-stack with a 10X objective (HCX APO L U-V-I 10.0x0.30 WATER). Two channels were used: Alexa Fluor 488, to observe CRC cells that expressed cells transfected with GFP, and Brightfield, to observe the cells migrate from the primary tumor chamber to the space between two chambers of the microfluidic device. The experiment lasted for 120 h and each 24 h was stopped to acquire images in a different region of the device.

Measurements of cell migration and motility parameters in MET-on-a-chip without Target Organ

Cell motility experiments were performed by a time-lapse and z-stack acquisition using a 10X objective (HCX APO L U-V-I 10.0x0.30 WATER) by a TCS SP5 MP Scanning confocal microscope (Leica). To evaluate cell migration, two areas of the primary tumor chamber were considered: cells that migrated into the stroma area and cells that migrated close to the pillars area. Briefly, two ROIs (503 x 599 μm^2), corresponding to the stroma and pillars areas, were selected using ImageJ Fiji software. Cell positions in each frame were tracked manually using the MTrackJ plugin of ImageJ Fiji and then added to an MS Excel file containing the DiPer suite of custom-made macros for quantifying migration parameters (Gorelik and Gautreau 2014). Specifically, Migration velocity and the Mean Squared Displacement (MSD) of individual trajectories (i.e., the time-dependent x and y coordinates of each cell centroid) at different time lags were calculated by the following formulas:

$$v = \sum \frac{\sqrt{(x_{i+1} - x_i)^2 + (y_{i+1} - y_i)^2}}{\Delta T} \quad (1)$$

$$MSD\ (\tau) = [x(t-\tau) - x(t)]^2 + \ [y(t-\tau) - y(t)]^2 \quad (2)$$

where x_i e y_i were the coordinates of cell in the i-th frame, ΔT is the time interval between two frames, t is the time, and τ is the lag time. To estimate diffusion coefficient D and directional persistence P, MSDs curves were fitted with Fürth's Formula (Selmeczi, Mosler et al. 2005):

$$MSD(\tau) = 4D(\tau - P\left(1 - e^{-\frac{\tau}{P}}\right)) \quad (3)$$

The fitting was done with ordinary nonlinear least-squares regression analysis. A further parameter to quantify directional persistence is α-value, calculated as the slope of log-log plot, with log(MSD) on the y axis and log(time interval) on the x-axis: a log-log curve with slope α = 1 indicates a random migration; a slope α<1 indicates a sub-diffuse migration includes confined diffusion and anomalous diffusion; a slope 1 < α < 2 indicates a super-diffuse migration in which the motion is faster and in a specific direction (α = 2 for cells that move along a straight line); a slope 0 < α < 0.5 indicates a random caged migration. In addition, Directionality ratio, the straight-line length between the start-point and the end-point of the migration trajectory, divided by the length of the trajectory, was calculated by the following mathematical equation:

$$Directionality\ ratio = \frac{Cell\ displacement\ (d)}{Cell\ accumulated\ distance\ (D)} \quad (4)$$

This ratio is equal to 1 when a cell is moving in a straight line, while it is equal to 0 when a cell has a random movement at a particular measured point. Rose plots were obtained using the open-source program DiPer by inserting the cell trajectories where the starting point of each track is located at the origin of the coordinate system. Statistical comparisons were performed with a Student's unpaired test when data exhibit a normal distribution. Instead, a nonparametric Mann-Whitney test was used. P-values of <0.05 denote statistically significant differences.

In situ Online monitoring of 3D NF µTs in MET-on-a-chip

Online monitoring of 3D NF µTs into the primary tumor chamber was conducted and several images in different areas of the chamber were acquired by using a 25X objective (HCX IRAPO L 25x 0.95 WATER). Two channels were used: Brightfield channel and SHG signal to detect the production of collagen fibers. The device was monitored for 96 h acquiring the different areas at different times (24h, 48h, and 96h).

Fibroblasts counting analysis between MET-on-a-chip with 3D CRC µTs alone and MET-on-a-chip with 3D NF µTs

To evaluate the number of fibroblasts that migrate in the MET-on-a-chip platform in the presence or absence of colon cancer cells, analysis for counting fibroblasts was performed using ImageJ Fiji software, the plugin "Cell Counter". After 120 h, 4 images of different areas were acquired from Confocal Leica TCS SP5 II combined with a Multiphoton Microscope. In detail, the counting was carried out by selecting 4 ROI (16.7 X 16.7µm^2) in each image for each sample. The results of cell counting were expressed as the ratio between the total cell number and ROI area. Statistical analyses were performed by ANOVA Tukey HSD test. Statistical significance was set at a value of $p < 0.01$. The experiment was repeated in independent studies.

In situ Online monitoring of CRC cell migration with Target Organ

Online monitoring of CRC cells migration towards the Target Organ was performed using the second configuration of the MET-on-a-chip device. Tile-scan stacks 25 and 15 step numbers of Z-stack and Time-lapse imaging with a time interval of 30 min and a 10X objective (HCX APO L U-V-I 10.0x0.30 WATER) was performed. Two channels were used: Alexa Fluor 488, to observe CRC cells that expressed cells transfected with GFP, and Brightfield channel, to observe the cells m from the primary tumor chamber to Target Organ chamber of the microfluidic device. The experiment lasted for 96h and each 24h the image acquisitions were carried out in both the primary tumor and the Target Organ chambers.

3.3 Results and Discussions

3.3.1 Preliminary results of cancer cell migration in transwell inserts in the presence or the absence of Target Organ

To investigate the high invasive capacity of colon cancer cells, HCT-116 cells, a preliminary experiment of cancer cell migration by using transwell in the presence or the absence of Target Organ was performed. For these preliminary experiments, transwell inserts with membrane pore size 3 µm were used, and 3D CRC µTs and 3D HepG2 µTs, produced as reported in paragraph 3.2.1, were placed into the apical chamber and basal chamber of Transwell respectively and maintained in culture for a week (Day 0-7) (Fig. 3.3). As a control, another transwell was used to accommodate 3D CRC µTs into the apical chamber without 3D HepG2 µTs basal chamber to evaluate the cell migration also in the absence of Target Organ.

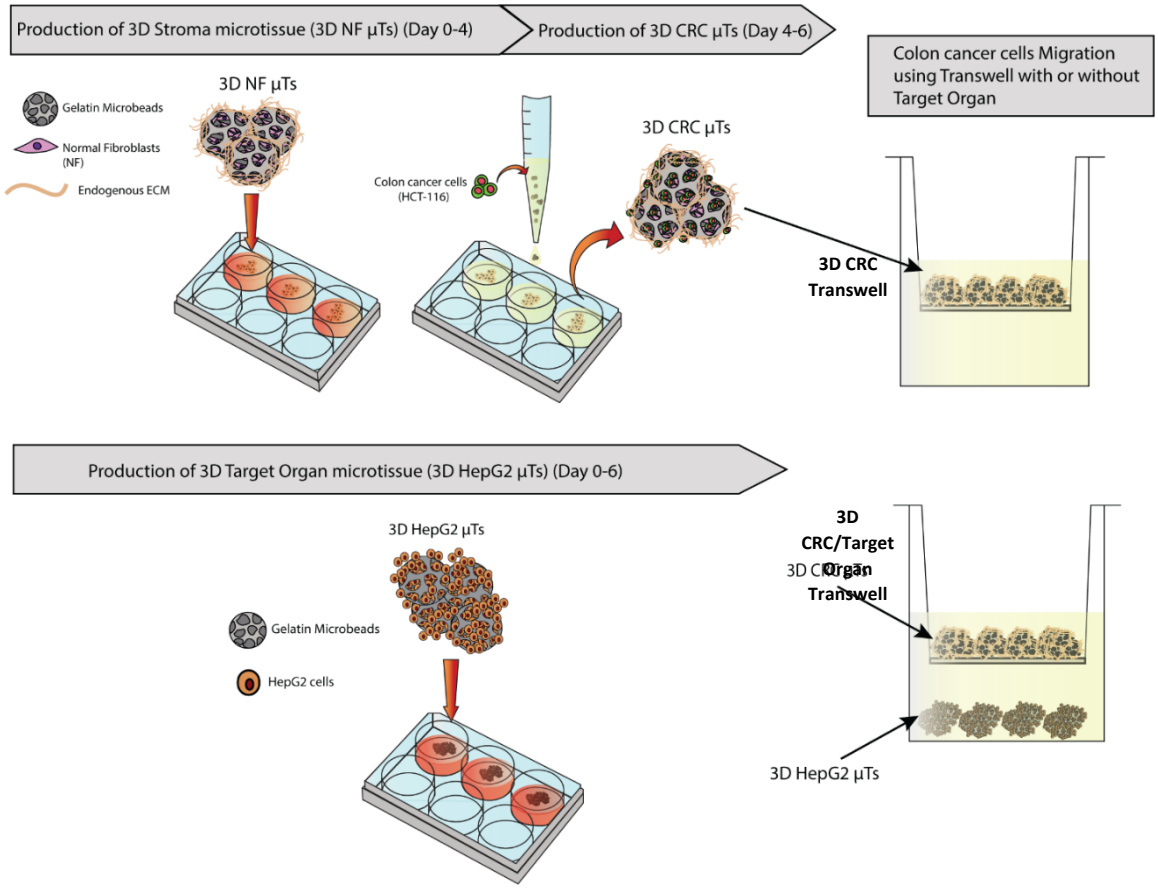

Figure 3.3 A schematic diagram of 3D CRC µTs and 3D HepG2 µTs fabrication and set up of 3D CRC Tranwell (3D CRC µTs housed into the apical chamber) and 3D CRC/Target Organ Tranwell (3D CRC µTs and 3D HepG2 µTs housed into the apical and basal chambers respectively) for the experiment of cell migration.

Images acquired by Confocal Fluorescence Microscopy displayed an overview of the lower side of transwell membrane in 3D CRC Transwell (Fig. 3.4 a-c) and 3D CRC/Target Organ Transwell (Fig. 3.4 d-f) at Day 1 of cell migration. In detail, high magnification insets of the lower side of the transwell membrane showed that some cells were migrating through the pores of size 3 µm, thus the green dots lined up with some of the pores of the low side of the membrane in 3D CRC Transwell and 3D CRC/Target Organ Transwell (Fig. 3.4 c, f insets with a dashed red circle). This evidence demonstrated not only the high invasive capacity of colon cancer cells but also their ability to change their shape to cross pores smaller than 8 microns in diameter (Justus, Leffler et al. 2014). This feature of cancer cells is named Plasticity and it has been widely reported in the literature as a typical feature of invasive cancer cells (Wu, Jiang et al. 2021).

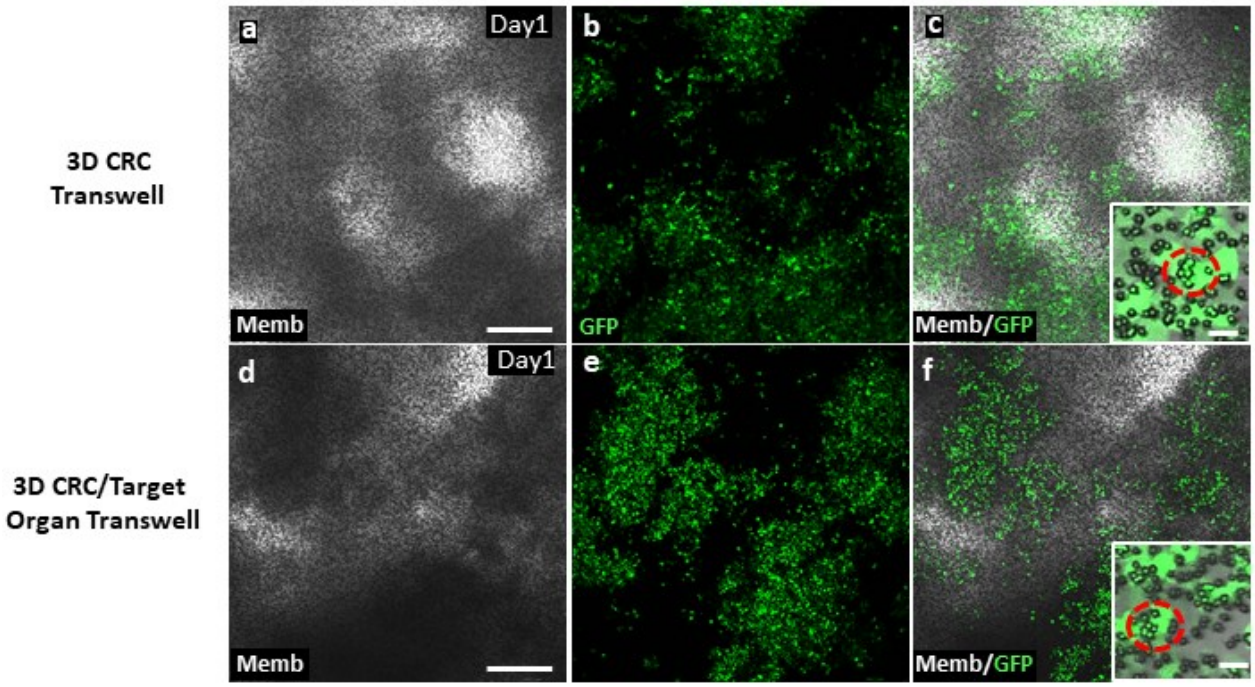

Figure 3.4 Overall picture of the Lower side of the membrane (Memb) of 3D CRC Transwell (3D CRC µTs housed into the apical chamber) (a-c) and 3D CRC/Target Organ Transwell (3D CRC µTs and 3D HepG2 µTs housed into the apical and basal chambers respectively) (d-f) at Day 1 of cell migration; scale bar 300 µm. High magnification insets of the lower side of the membrane in 3D CRC Transwell (c) and 3D CRC/Target Organ Tranwell (f); Two channels were used, brightfield channel to show the membrane and green channel to show GFP signal of HCT-116 cells; scale bar 50 µm.

On Day 6, the Z-stack images of the 3D CRC Transwell membrane displayed the HCT-116 cells migration from the upper to lower side of the membrane (Fig. 3.5 a-i), as it is shown also in the illustration (Fig. 3.5 j). In detail it was possible to observe the presence of many HCT-116 cells at the lower side of the membrane (Fig. 3.5 g-i), indicating that cancer cells had crossed the porous

membrane to invade the basal chamber. In addition, the higher-magnification inset of the lower compartment of the membrane (Fig. 3.5 k-m) showed that HCT-116 cells exhibited an elongated, spindle-like cell shape (Fig. 3.5 k, l yellow arrow) with the formation of pseudopod protrusions that went through the porous of the membrane (Fig. 3.5 k-m white arrows).

Moreover, several HCT-116 cells were distributed in different regions of the basal chamber in the 3D CRC/Target Organ Transwell (Fig. 3.6 d-f) and the 3D CRC Transwell (Fig. 3.6 a-c). However, clusters of cancer cells interacting with 3D HepG2 µTs were observed in several areas in the 3D CRC/Target Organ Transwell, differently from the 3D CRC Transwell where single HCT-116 cells were scattered in different regions of the basal chamber. This particular case provides evidence that cancer cells invaded and colonized the Target Organ, forming tumor foci (Skardal, Devarasetty et al. 2016). Albeit these results obtained by using the transwell inserts were promising, however, these systems request the use of large volumes of cell medium which implies the signaling factors are diluted in the cell medium and, in turn, the cell communication results slowed down. In addition, these systems are cultured in a static condition, which impedes to simulate the dynamic processes and to control several cell physical and/or biochemical stimuli (Picollet-D'hahan, Zuchowska et al. 2021). For these reasons, I evaluated the possibility to explore microfluidic strategies.

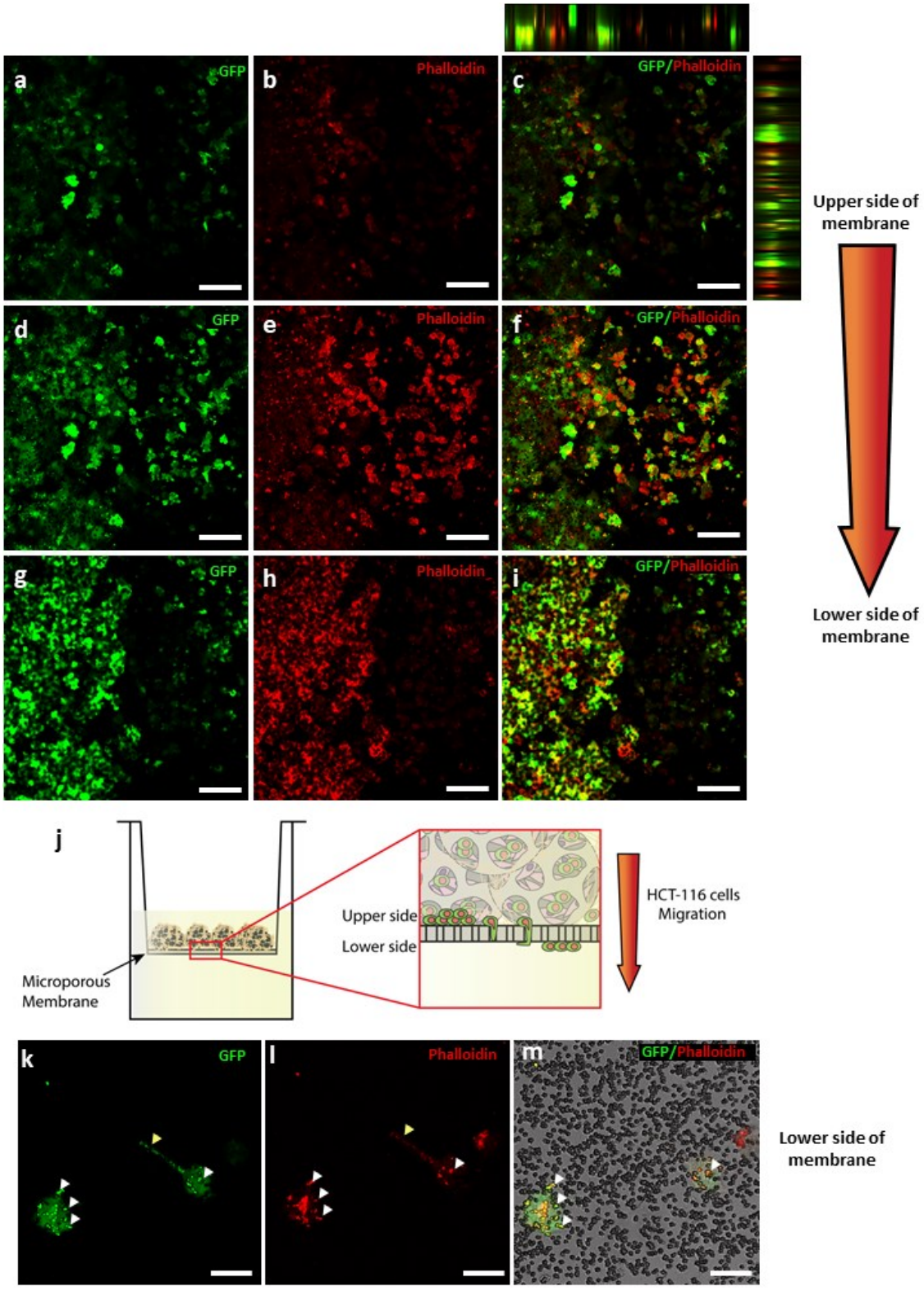

Figure 3.5 Colon cancer cells migration of 3D CRC µTs observed by a series of z-stack confocal microscopy images. Three images of 200 slices of the Z-stack series were considered to investigate the cancer cell migration: 1 (a-c), 71 (d-f), and 136 slices (g-i). The images were acquired through the green (GFP for HCT-116 cells) (a, d, g) and red emission (Phalloidin) (b, e, h), and merged images were obtained (c, f, i); scale bar 100 µm. Schematic image of HCT-116 cells migration through the microporous membrane (j). High Magnification inset showed the elongated, spindle-like shape of

HCT-116 cells (yellow arrow) with the formation of pseudopod protrusions at the lower side of the membrane (white arrows) (k, l, m); scale bar 80 µm.

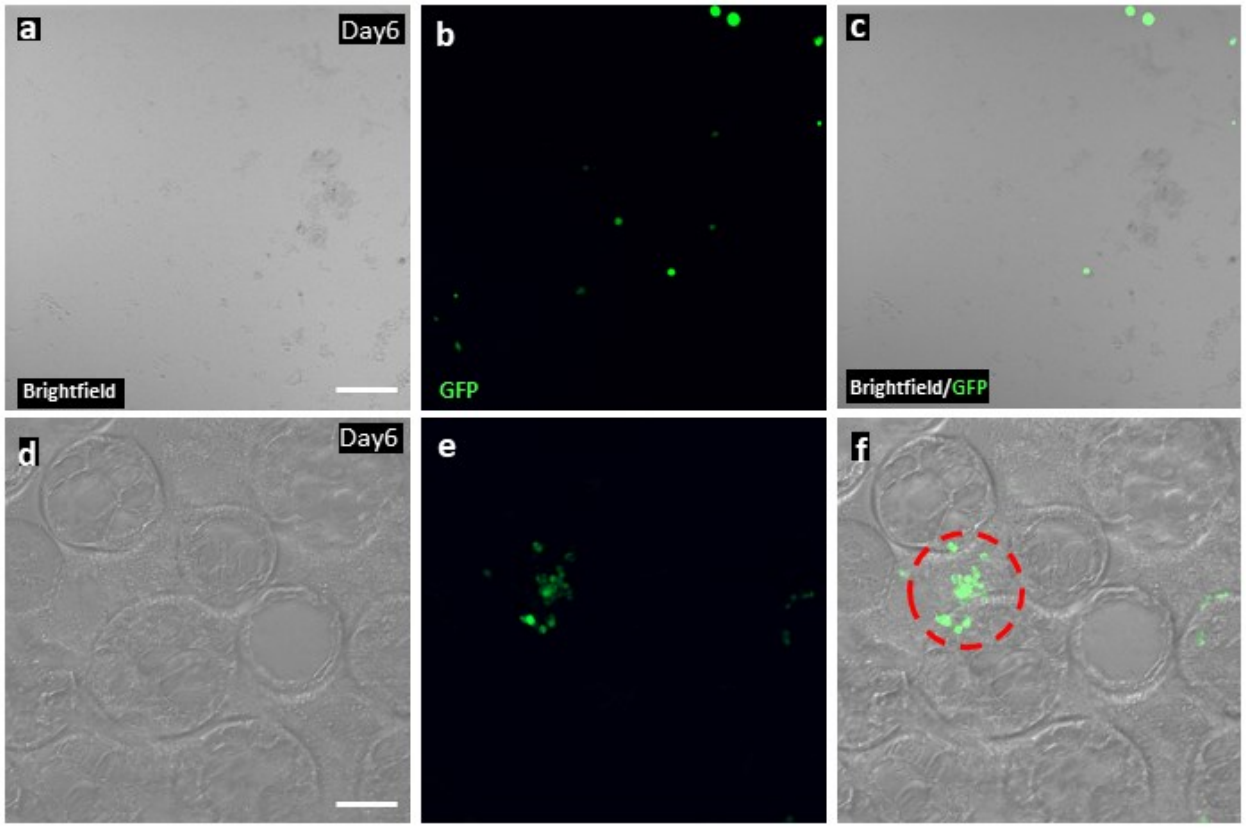

Figure 3.6 Basal chamber of transwell insert at Day 6 of cell migration in 3D CRC Transwell (a, b, c) and 3D CRC/Target Organ Transwell (d, e, f); A cancer cell cluster was showed in 3D CRC/Target Organ Transwell at Day 6 of cell migration, indicated with a dashed red circle (f); Two channels were used, brightfield channel to show the membrane and green channel to show GFP signal of HCT-116 cells; scale bar 100 µm.

3.3.2 Comsol simulation of MET-on-a-chip platforms

To select the optimal parameters for dynamic culture and to check if the 3D CRC µTs and 3D HepG2 µTs were well oxygenated in two configurations of MET-on-a-chip platforms, we carried out CFD simulations (Computational Fluid Dynamics), as mentioned in the previous 3.2.4 paragraph. We used a flow rate Q=2µl/min in both configurations of MET-on-a-chip platforms because this parameter is comparable to blood flow *in vivo* tissue (Albanese, Lam et al. 2013). At first, the simulations were performed considering the first configuration of the MET-on-a-chip (Fig. 3.7 a-d). Fig. 3.7 a shows that the velocity of cell medium is higher in the inlets and the outlet than the area enclosed by the internal lateral walls and the pillars (depicted in white into Fig. 3.7 a), differently

from the inlets of microtissues loading that is zero. The oxygen concentration was high in all parts of the device, whereas it was low in the primary tumor and Target Organ chambers, indicating that there was a high oxygen consumption due to the 3D CRC µTs and 3D HepG2 µTs (Fig. 3.7 b), as displayed also in Fig. 3.7 c in which the streamlines cross all part of the device. In addition, Fig. 3.7 d shows the simulation of fluid pressure in which it is possible to find high pressures in correspondence of the inlets of cell medium and low pressures in the outlet of the device.

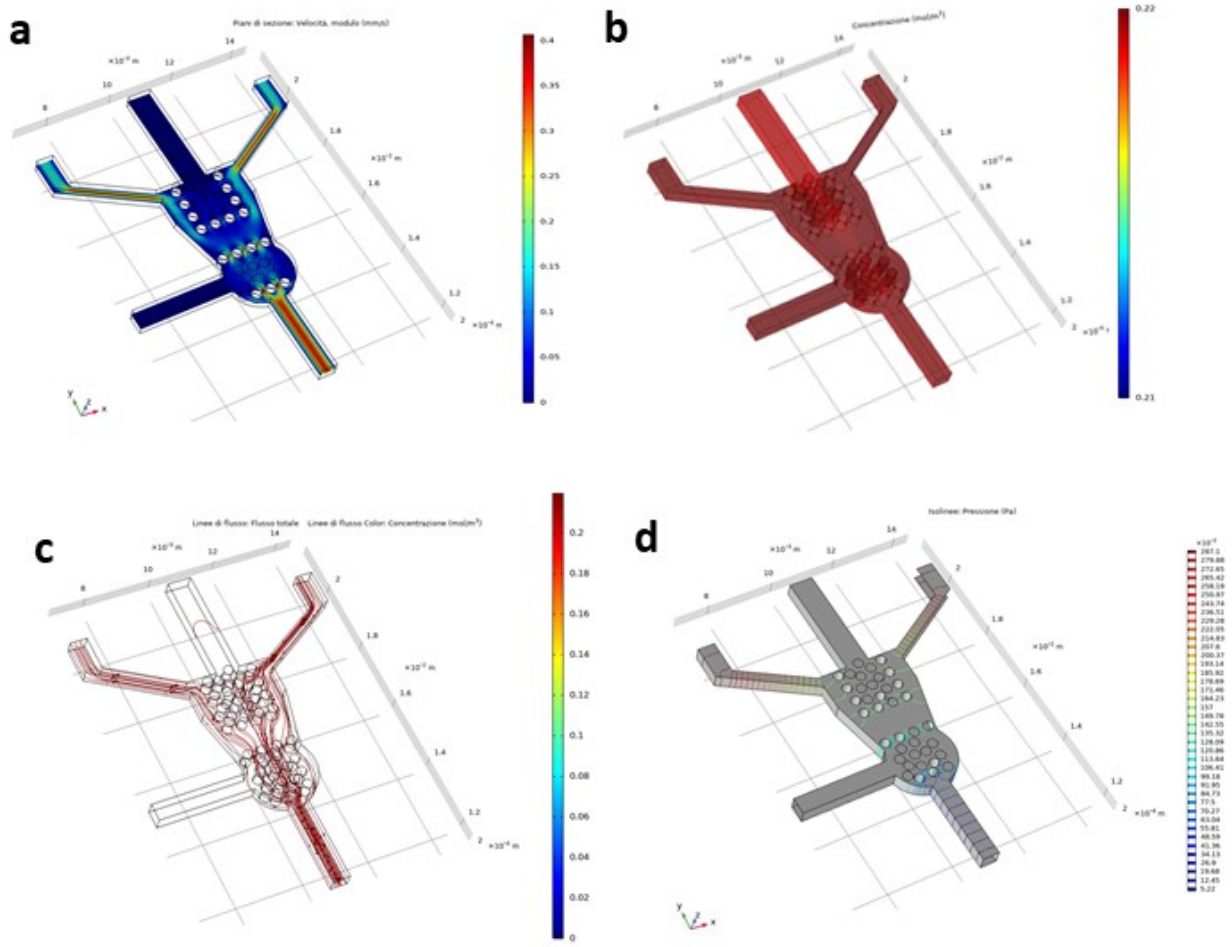

Figure 3.7 CFD simulations of 3D CRC µTs and 3D HepG2 µTs loaded in the first configuration of the MET-on-a-chip platform using COMSOL Multiphysics. Velocity field (a); Oxygen concentration and streamlines (c); Flow pressure (d).

Since the fluid velocity resulted very high along the lateral inlets, to avoid that the microtissues could be subjected to excessive stresses, we designed another configuration of MET-on-a-chip in which the section of lateral inlets was increased in dimension. Therefore, the simulations were performed considering the second configuration of the MET-on-a-chip (Fig. 3.8 a-d). Fig. 3.8 a shows the velocity of cell medium is slightly higher near the primary tumor chamber than all parts of the device

in which a homogeneously distributed velocity of cell medium is displayed. Instead, the flow velocity resulted zero in the inlets of microtissues loading. The oxygen concentration resulted homogeneously distributed in all parts of the device, indicating the cell medium supplied a sufficient amount of oxygen to microtissues (Fig. 3.8 b). Fig. 3.8 c shows the streamlines of the cell medium crossing all parts of the device. Moreover, the simulation of fluid pressure resulted high in correspondence of the inlets of cell medium and low in the outlet of the device (Fig. 3.8 d).

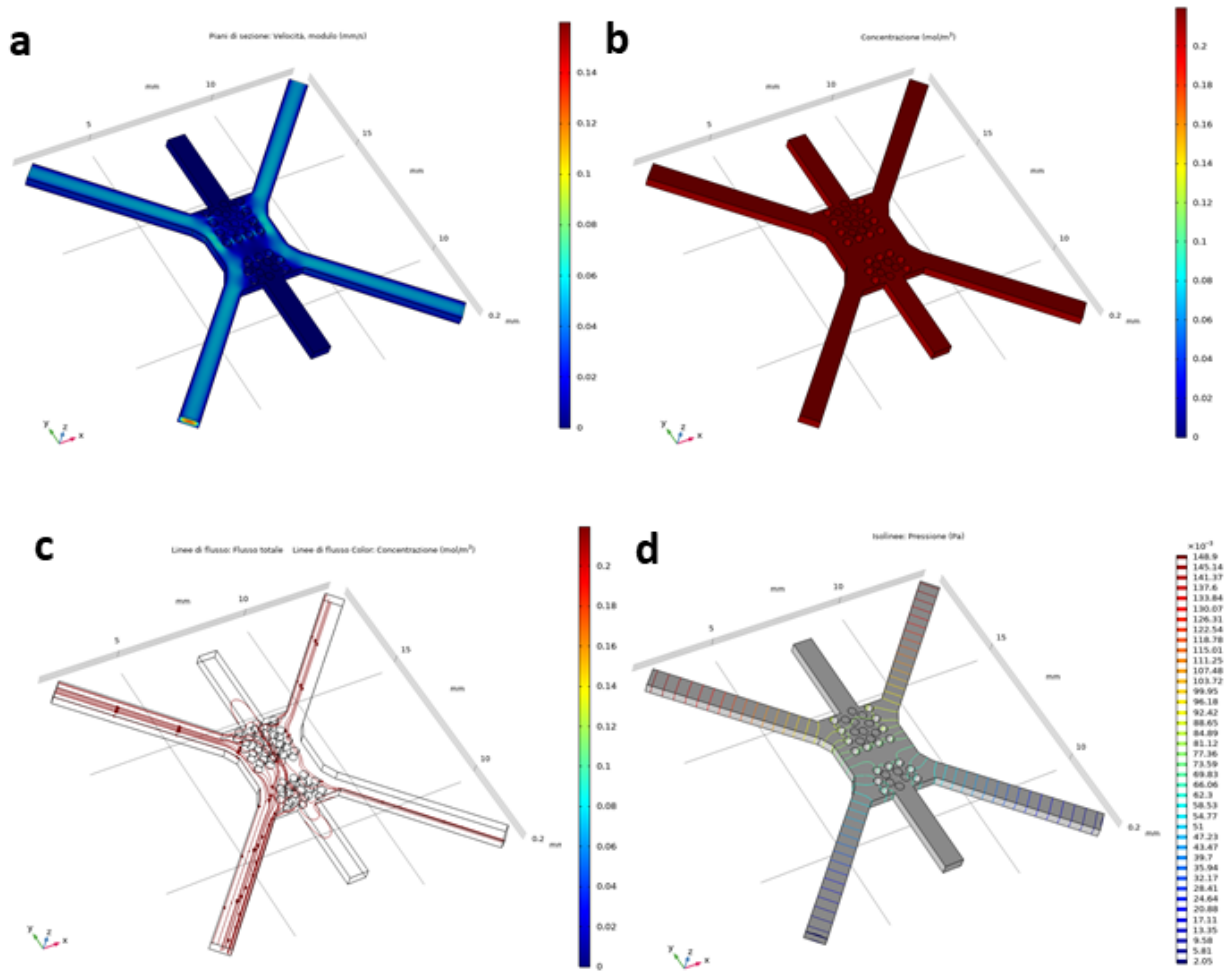

Figure 3.8 CFD simulations of 3D CRC µTs and 3D HepG2 µTs loaded in the second configuration of the MET-on-a-chip platform using COMSOL Multiphysics. Velocity field (a); Oxygen concentration and streamlines (c); Flow pressure (d).

The results of the simulations of both MET-on-a-chip platforms showed parameters – such as fluid velocity, oxygen concentrations, and fluid pressure – which seem appropriate for dynamic culture experiments. Starting from these findings, we assembled the experimental setup. In the preliminary tests, we used the first configuration in which 3D CRC µTs were housed without target organ, to acquire preliminary data of cancer cells migration. Then, we carried out further tests using the

second configuration of MET-on-a-chip in which 3D CRC µTs and 3D HepG2 µTs were loaded in the corresponding chambers, to observe the cross-talk between the primary tumor site and target organ site.

3.3.3 The migration of CRC cells in MET-on-a-chip platform without Target Organ

At first, the experiment of cancer cell migration was carried out without Target Organ, using the first configuration of the MET-on-a-chip platform (Fig. 3.9 a). After the sterilization of the device, 3D CRC µTs were loaded into the primary tumor chamber. After 5 h from loading, in situ online monitoring of cell migration by using a Confocal Leica TCS SP5 II combined with a Multiphoton Microscope was performed (Fig. 3.9 b). For this purpose, time-lapses with z-stacks of primary tumor chamber were implemented, the first lasted 16h and the second lasted 64h. Several images were extracted from each time-lapse video and imaging analyses of cell migration were performed. From these acquisitions, it was observed that HCT-116 cells were able to migrate below the pillars (the vertical distance between coverslips and the pillars was ~60 µm) finding as a preferential way to migrate. The HCT-116 cells began to migrate after 4h the time-lapse experiment started (Fig.9 c, red arrow); cells number increased at 13h, 25h, 64h, and 96h (Fig. 3.9 d, e, f, g, red arrows). In addition, changes in HCT-116 cells morphology from round to elongated and spindle-like shape were observed (Fig. 3.9 e red arrow), becoming more deformable and contractile, due to their high invasiveness and metastatic potential, as confirmed in literature (Walker, Sai et al. 2005). Several cell clusters were individuated outside of the primary tumor chamber at 96h of acquisition experiment, as better evidenced by the image at high magnification (Fig. 3.9 g inset blue square), reproducing the formation of Circulating Tumor Cell cluster (CTC cluster), a rare population of cancer cells that leave the primary tumor site to migrate and colonize the distant organs (Aceto, Toner et al. 2015). Moreover, the fibroblasts' migration was observed at different times and their number increased over time (Fig. 3.9 c-g, white arrows). Fibroblasts can be easily distinguished from HCT-116 cells because they do not express GFP signal and present a spindle-like cell shape. Furthermore, a direct and close interaction between fibroblasts and HCT-116 cells was more evident at longer migration times (Fig. 3.9 f, g), as displayed by the image at high magnification (Fig. 3.9 g inset red square), demonstrating the key role of fibroblasts in interacting with cancer cells to provide a cooperative invasion mechanism (Hurtado, Martinez-Pena et al. 2020). In addition, a comparison with MET-on-a-chip platform loaded with 3D NF µTs (without HCT116) into the primary tumor chamber was

performed to investigate the fibroblasts' tendency of migrating in the absence of cancer cells. The image analysis revealed that in absence of HCT-116 cells, the migration of fibroblasts is inhibited (Fig. 3.9 h), confirming the cooperation of stromal and tumoral components in the invasion and initialization of the metastatic process.

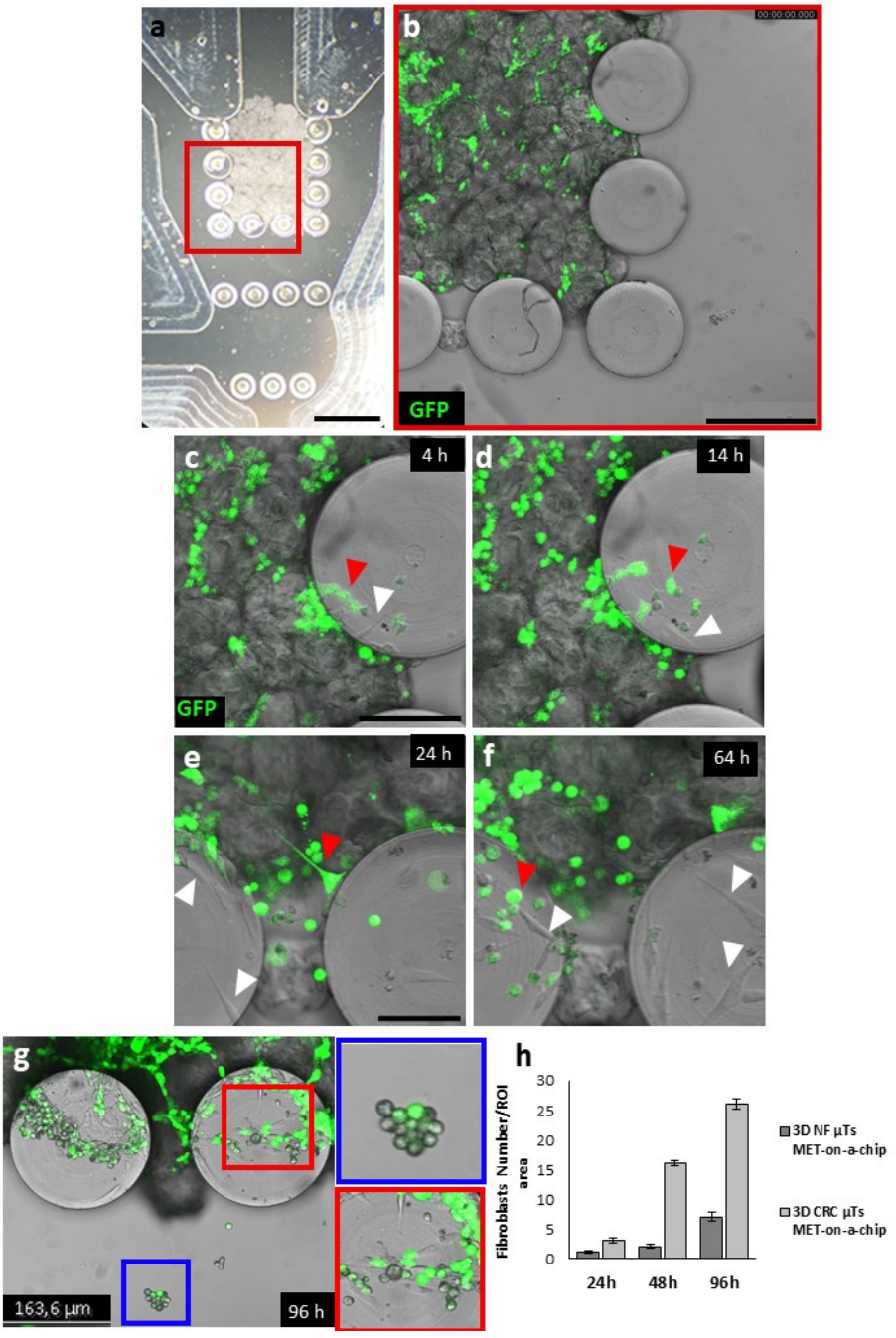

Figure 3.9 Time-lapse of HCT-116 cells migration into MET-on-a-chip platform without Target Organ. Image in brightfield of MET-on-a-chip platform loaded with 3D CRC µTs into the primary tumor chamber (a); scale bar 80 µm. Confocal image of the entire primary tumor chamber loaded with 3D CRC µTs and GFP signal was expressed by HCT-116 cells (b); scale bar 200 µm; Confocal images of time-lapse showed the HCT-116 cells (red arrows) and fibroblasts (white arrows)

migration in different time points (t=0h indicates the start of the acquisition experiment), at 4h, 14h, 24h, 64 and 96h (c, d, e, f, and g respectively); c and d (scale bar 100 µm); e and f (scale bar 80 µm); g (scale bar 200 µm; High magnification insets showed the cell cluster observed outside the primary tumor chamber (blue square) and the direct interaction between HCT-116 cells and fibroblasts (red square) at 96h of acquisition (g); scale bar 20 µm and 40 µm respectively. The graph showed the number of migrated fibroblasts in the presence or the absence of HCT-116 cells at 24h, 48h, and 96h (h); All the experiments were performed in triplicate (n = 3), values represent the mean and the standard deviation (g) (p ∗< 0.05; p ∗∗< 0.05).

Moreover, ECM remodeling was observed in the MET-on-a-chip platform loaded with 3D CRC µTs and 3D NF µTs. Confocal images acquired after 24h showed the presence of ECM both in 3D CRC µTs (Fig. 3.10 a) and 3D NF µTs (Fig. 3.10 c). However, images acquired after 96h showed a different scenario in 3D CRC µTs in which an increase of ECM degradation was displayed (Fig. 3.10 b), compared with 3D NF µTs in which an increase of collagen fibers production was highlighted (Fig. 3.10 d). Indeed, residual collagen fibers were shown on microbeads in 3D CRC µTs and on HCT-116 cells (Fig. 3.10 b white arrows), as observed in high magnification inset (Fig. 3.10 b inset). The high ECM degradation in MET-on-a-chip platform loaded with 3D CRC µTs suggest a strong proteolytic action of HCT-116 cells which degraded the surrounding ECM to invade and migrate.

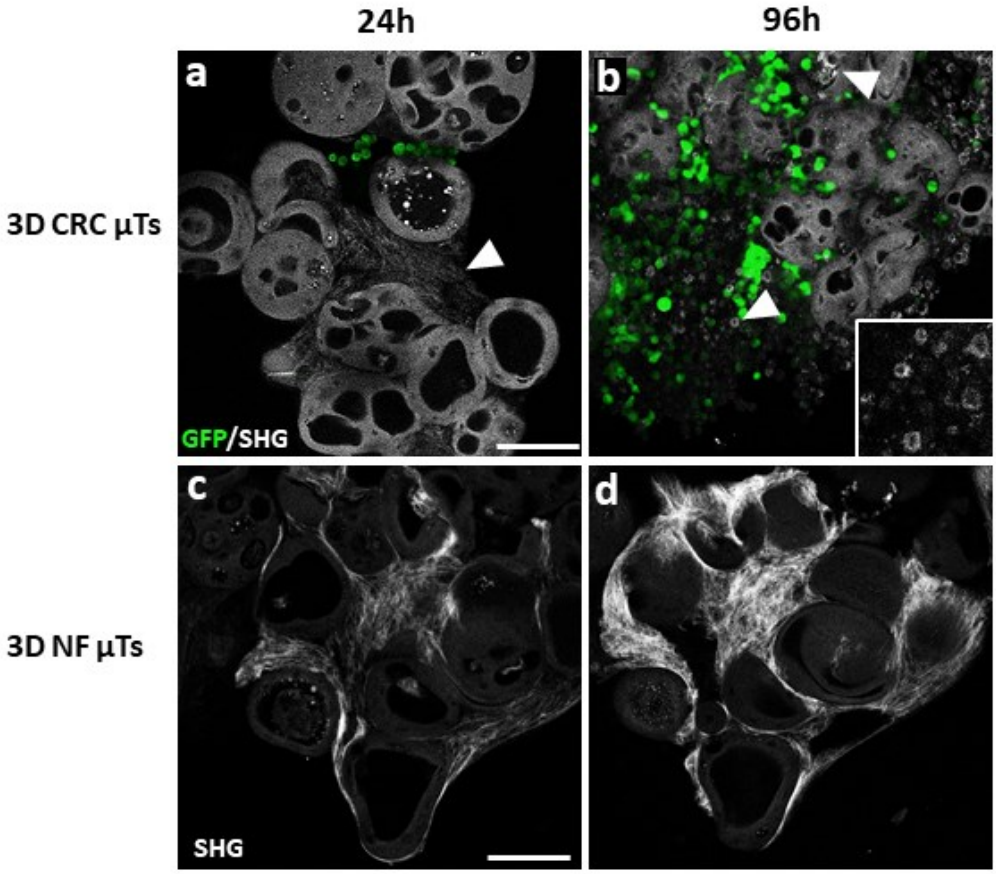

Figure 3.10 ECM Remodeling in MET-on-a-chip platform loaded with 3D CRC µTs (a, b) and 3D NF µTs (c, d) at 24h and 96h; scale bar 100 µm.

3.3.4 Analyses of cancer cell motility in MET-on-a-chip platform without Target Organ

To investigate if differences in cancer cells migratory behavior in different regions of the tumor chamber of MET-on-a-chip existed, 2 different zones were identified (we referred to as "stroma" and "pillar") and a time-lapse over a 16 h period was recorded with an interval of 60 min using time-lapse microscopy. The following parameters were evaluated to describe the cell motility: diffusion coefficient (D), Persistence (P), Speed (S), Directionality ratio (d/D), and α value. Images acquired by Confocal Leica TCS SP5 II Microscope showed the stromal region and pillars region (Fig. 3.11 a) from which cell trajectories were extracted (Fig. 3.11 b). «Rose-plots» of cell trajectories, a fast yet powerful way to visually compare cancer cell migration behavior, showed that the HCT-116 cells migration increased close to pillars region (Fig. 3.11 d), differently from the HCT-116 cells migration present in the stroma (Fig. 3.11 c). In addition, mean squared displacement (MSD) of the cell trajectories, which indicate how far a cell migrates in a given time interval, showed HCT-116 cells located near pillars had higher motility than those present in the stromal region (Fig. 3.11 e). Furthermore, it is known that MSD provides information about speed and directional persistence, and it is often shown as a log-log plot, with log(MSD) on the y axis and log(time interval) on the x-axis (Fig. 3.11 e). The graph of speed (S) displayed that HCT-116 cells located near to pillars migrated faster (0.162 µm/min ± 0.022) than those that migrated in the stroma (0.099 µm/min ± 0.013) (Fig. 3.11 f). Whereas the speed parameter is easy to calculate and interpret, the persistence time (P) describes how well the direction of migration is maintained and has been estimated by fitting the mean square displacements (MSDs) over time with the Fürth's formula (Material and Methods). Fig. g showed that HCT-116 cells that migrated near pillars had a high P-value compared to cancer cells located in the stroma. The low S and P of HCT-116 cells migrating in the stroma could be owing to the presence of surrounding ECM that could hinder or slow down the cancer cell motility. Instead, the high S and P of HCT-116 cells migrating near the pillars could be due to the flow condition into the microfluidic device could affect the cancer cells migration, as shown also in literature in which the flow could create small drag-forces on the cells (Walker, Sai et al. 2005). Furthermore, values of Diffusion coefficient (D) were obtained by fitting with Fürth's formula and results showed that HCT-116 cells located near the pillars had a high value of D, compared to those located in the stroma, confirming the correlation with P (Fig. 3.11 h). To confirm the persistence analysis, the α-value and

Directionality ratio (d/D) were obtained. A dot plot of Fig. 3.11 i showed the distribution of α-values of single cells MSD in the stroma and those near the pillars. The results displayed that both MSD of HCT-116 cells migrating in the stroma and those of HCT-116 cells migrating near the pillars showed a superdiffusive behavior with slopes equal to 1.47 ± 0.08 and 1.5 ± 0.10, respectively (Fig. 3.11 i). In addition, the graph of d/D displayed that HCT-116 cells migrated more in a straight line near the pillars than in the stroma (Fig. 3.11 j). Both results of α-values and d/D were correlated with the P and D results (Fig. 3.11 g, h).

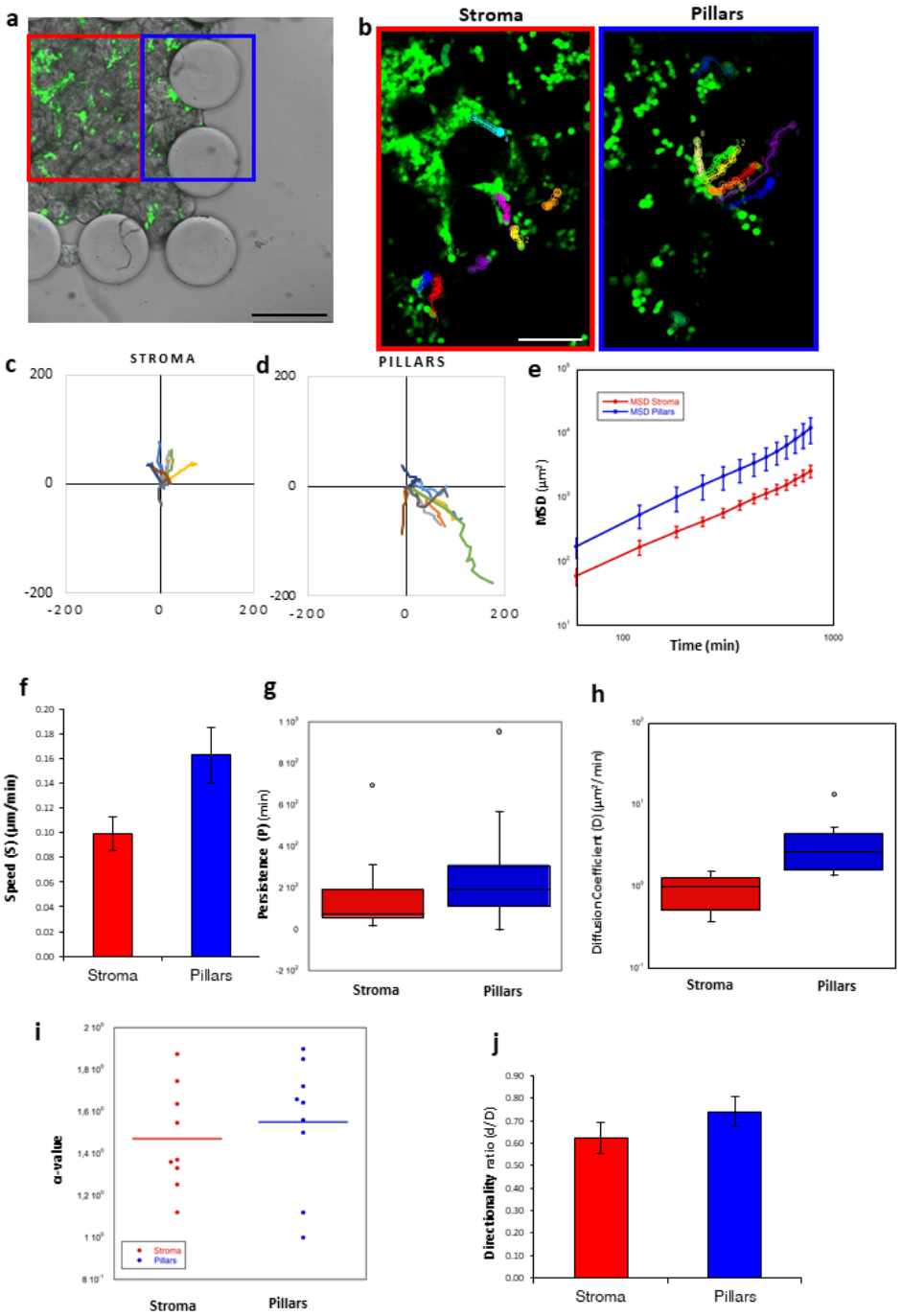

Figure 3.11 Analyses of cell motility behavior in the stroma and near the pillars in MET-on-a-chip. Confocal image of the entire primary tumor chamber with scale bar 200 µm (a); Cell trajectories obtained in the stroma and near the pillars with scale bar 150 µm (b); Rose plots of cell trajectories that migrate in the stroma (c) and near the pillars (d); MSD represented as a log-log plot and calculated from cell trajectories of cancer cells migrated (e); Graph of Average Speed (S) (f); Box plot of Persistence time (P) (g) and Diffusion Coefficient (D) (h) of cancer cells migrated in the stroma (red) and near the pillars (blue); Dot plot of α- values (i) of cancer cells migrated; Graph of Directionality ratio (d/D) (j).

3.3.5 The migration of CRC cells in MET-on-a-chip platform in presence of Target Organ

Figure 12 shows the cancer cell migration towards the Target Organ using the second configuration of the MET-on-a-chip device. In detail, Fig. 3.12 a illustrates an overall portrait of the MET-on-a-chip device loaded with 3D CRC µTs and 3D HepG2 µTs in the aforementioned chambers, as shown even in the tile scan image (Fig. 3.12 b). To observe the cancer cell migration, two regions were considered, as illustrated in Fig. b: namely, the red rectangle encloses the chamber of 3D CRC µTs and the blue rectangle enclosed the chamber of 3D HepG2 µTs. These two regions were monitored for 16h, 24h, and 48h (Fig 12 c-h). The confocal microscopy images, framed in red and extracted by Time-lapse videos, showed many HCT-116 cells migrated from the stromal area (Fig. 3.12 c) towards the pillars of the primary tumor chamber after 48h (Fig. 3.12 d, e). In addition, these images showed that HCT-116 cells migrated in close contact with fibroblasts (blue arrows) inside the primary tumor chamber (stromal area) and between the pillars after 48h (Fig. 3.12 c-e, blue arrows), as found even in Fig. 3.9 of section 3.3.3, demonstrating once again the key role of fibroblasts in interacting with cancer cells to provide a cooperative invasion mechanism (Hurtado, Martinez-Pena et al. 2020). The confocal microscopy images, framed in blue, revealed the presence of HCT-116 cells in the Target Organ chamber after 16h (Fig. 3.12 c red arrows), but it was not possible to track the path of cancer cells due to bubble formation into the device. However, some HCT-116 cells were observed near the Target Organ chamber after 24h (Fig. 3.12 g), probably many cancer cells were carried out by the flow and very few cancer cells arrived at the Target Organ chamber, suggesting that the metastasis process and formation are very rare and only a low percentage of cancer cells can colonize and form metastasis into the target organ, as shown in native tissue (Ruiz-Espigares, Nieto et al. 2021). After 48h the number of HCT-116 cells was reduced into the Target Organ chamber (Fig. 3.12 h), probably cells present a scares capability to adhere to the target organ and they were carried out by the flow. Regarding the acquisitions performed at 96h (data not shown), it seems a

prolonged exposure time of 3D CRC µTs and 3D HepG2 µTs could cause excessive stress of these models, thus further experiments should be carried out to confirm this potential issue.

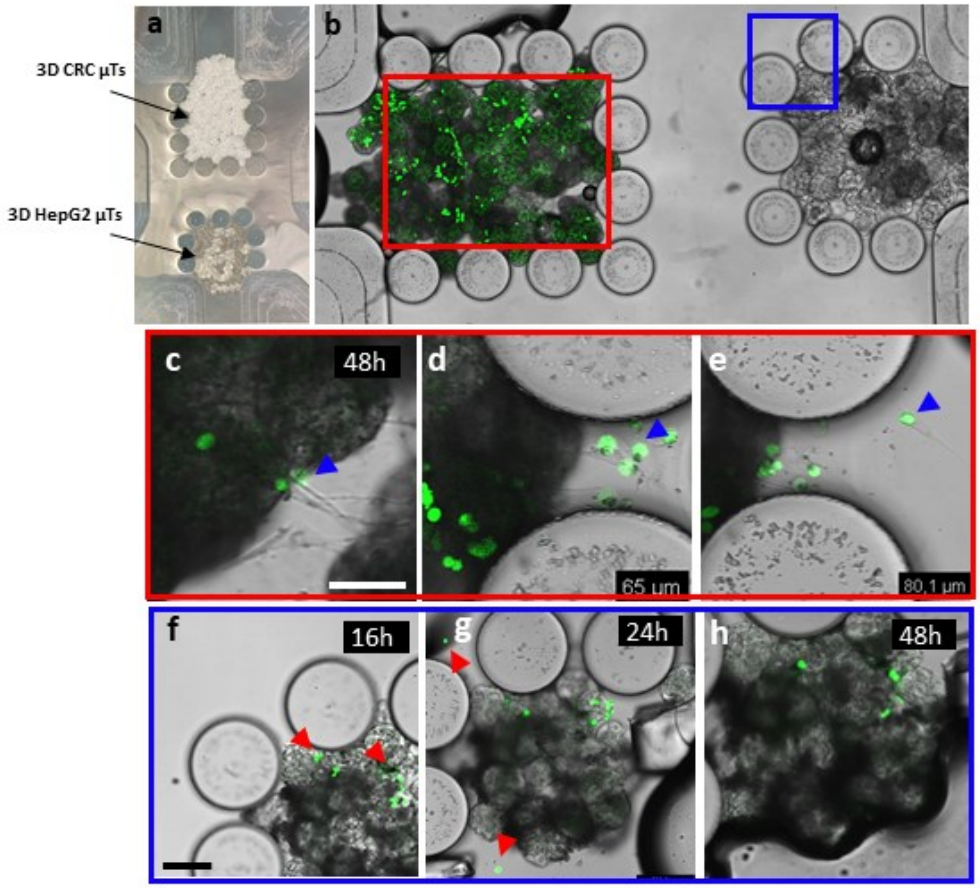

Figure 3.12 Cancer cells migration towards Target Organ in the second configuration of the MET-on-a-chip device. Overall images of the MET-on-a-chip device loaded with 3D CRC µTs and 3D HepG2 µTs (a, b), scale bar 1000 µm and 200 µm (tile scale reconstruction); HCT-116 cells migration with fibroblasts after 48h, indicated with blue arrows (c-e), scale bar of images (c, d) 65 µm and image (e) 80 µm; The presence of HCT-116 cells in the Target Organ chamber after 16h (f), 24h (g) and 48h (h), scale bar 150 µm.

3.4 Conclusion and Future Perspectives

In this study, we developed novel microfluidic platforms, named "MET-on-a-chip", to investigate and to reproduce hepatic metastasis from colorectal cancer. Preliminary results of colon cancer cell invasion, migration, and colonization into the target organ were obtained using transwell inserts, accommodating our 3D microtissue models that reproduce the primary tumor and target organ respectively. Albeit the transwell experiments showed promising migration results, nevertheless they do not resemble the dynamic conditions of the *in vivo* metastasis process. Differently, the optical accessibility of the microfluidic devices coupled with the high-fidelity features of our 3D microtissue models allowed, for the first time (to the best of the author's knowledge), to monitor –

in an online and straightforward manner – the invasion into the primary tumor, migration, and colonization of cancer cells into the target organ. The results seem very promising; however, further improvements and proofs will be acquired to validate this first evidence (namely, the spontaneous metastasis formation in transwells) and to investigate further the mechanisms underlying the bidirectional cross-talk between primary tumor and target tissues. Moreover, our devices could be potentially used as platforms for drug and or natural compounds testing and high-throughput screening to bridge the gap between current 3D tissue models and animal models, even reducing expensive and time-consuming protocols nowadays used in preclinical studies.

4. Supplementary: Design and fabrication of *in vitro* 2D cell culture models for drugs and nutraceuticals screening

4.1 Introduction

In the beginning, we carried out preliminary tests of the combination treatments with CT-NE-Curc and 5-FU on *in vitro* 2D cell cultures in order to investigate the synergistic effect of curcumin in targeting selectively the high invasive cancer cells (HCT-116 cells) and to prevent the cytotoxic effect of 5-FU on low invasive cancer cells (Caco2 cells) by using more simplified cell culture models. These preliminary experiments were useful to gain insights about the behavior of 5-FU alone, CT-NE-Curc alone, and their combination, to move towards the use of 3D tumor microtissues, that reproduce faithfully the complexity of TME.

4.2 Materials and Methods

4.2.1 *In vitro* 2D cell culture models

Cell types and subculturing

Human colorectal adenocarcinoma cell line (CaCo-2 cells) was obtained from American Type Cell Culture (ATCC, USA) and grown in Dulbecco's Modified Eagle's Medium (DMEM, Gibco) supplemented with 10% FBS (Sigma Aldrich), 200 mM L-Glutamine (Gibco), 100 IU ml^{-1} streptomycin/penicillin (Gibco). The seeding density of Caco2 cells was 10^5 cells/cm^2. The culture medium was changed every 2-3 days.

Human colorectal carcinoma cell line (HCT-116 cells) was sub-cultured in Dulbecco's Modified Eagle's Medium (DMEM, Sigma) supplemented with 10% FBS (Sigma Aldrich), 200 mM L-Glutamine (Himedia), 100 IU ml^{-1} Streptomycin/Penicillin (Himedia). The recommended seeding density of HCT-116 cells was 20 000 cells/cm2. HCT-116 cells were subcultured every 2-3 days.

Regarding the treatments and pre-treatments with NE-Curc and 5-FU, Caco2 and HCT-116 cells were sub-cultured onto T25 Flasks (Corning ® Costar ®). A day before the treatments, both cell lines were detached from flask Caco2 using Trypsin/EDTA 0,05% (Himedia), centrifuged at 1000 rpm for 5 min, and cultured in 96-well plates flat bottom at a density of 15 000 cells and 10 000 cells respectively and incubated at 37◦C in a humidified 5% CO2. Three 96-well plates flat bottom were prepared in order to carry out the treatments in 3 different time points: 24 h, 48 h, and 72 h.

4.2.2 Treatments on *in vitro* 2D cell culture models

For drug treatments, the 5-FU stock solution in DMSO [76 mM] was diluted at different concentrations in DMEM high glucose supplemented with 10% FBS (Sigma Aldrich), 200 mM L-Glutamine (Himedia), 100 IU ml −1 Streptomycin/Penicillin (Himedia). The final concentration of DMSO was less than 1% of drug treatment. To treat 2D cell culture models, different concentrations of 5-FU were used: 0 µM; 0,1 µM; 1 µM; 10 µM; 25 µM; 50 µM; 100 µM; 200 µM for 24, 48 and 72 h. Then, CT-NE-Curc was sterilized using PVDF filters (Millicell) and diluted at different concentrations into the same cell medium of 5-FU: 1:8 and 1:10. To investigate the co-adjuvant and cytoprotective effect of curcumin, both Caco2 and HCT-116 cells were treated with NE-Curc (1:8) for 2 h and incubated at 37◦C in a humidified 5% CO_2. After 2 h, cells were washed two times with sterile PBS and were treated with 5-FU at 10 µM and 100 µM or with their cell medium, as control. The effects were observed after 24, 48, and 72 h.

4.2.3 Cell viability assay

To evaluate the cell viability after 5-FU and NE-Curc combination treatment in 2D cell culture models as well as in 3D CRC µTs and 3D NF µTs, 3-(4,5-dimethylthiazol-2-yl)-2,5-diphenyltetrazolium bromide (MTT) assay was used according to the manufacturer's instructions (Sigma). Briefly, after 24, 48, and 72 h of treatment, both 2D and 3D cell cultures were washed two times with PBS, 200 µl of the MTT solution (5mg/ml) was added in each well incubating at 37◦C in a humidified 5% CO_2 for 3 h in the dark. Then, MTT solution was removed from each well and the remaining crystals (formazan precipitates) were solubilized with 200 µl of DMSO, and the cells were incubated for an additional 30 min at 37 °C with gentle shaking. In the end, the optical density of each well sample was measured with a microplate spectrophotometer reader at 550 nm, and the cell viability (%) was calculated by the following equation:

$$Cell\ Viability\ (\%) = \frac{OD\ treated}{OD\ control} x\ 100 \quad (1)$$

All statistical comparisons were performed with the ANOVA test followed by the Tukey HSD test. P-values of <0.05 denote statistically significant differences. For all data sets, experiments were repeated in independent studies.

4.3 Preliminary Results and Discussions

4.3.1 Treatments with 5-FU and CT-NE-Curc on *in vitro* 2D cell culture models

To explore the selective role of curcumin as an adjuvant in the cytotoxic action of 5-FU on invasive cancer cells and as a protector for healthy cells, *in vitro* 2D cell culture of low invasive cells, Caco2 cells, and high invasive cells, HCT-116 cells, were treated with 5-FU and NE-Curc alone and pretreated with NE-Curc and co-treated with 5-FU. At first, treatment with several 5-FU concentrations (0 µM; 0,1 µM; 1 µM; 10 µM; 25 µM; 50 µM; 100 µM; 200 µM) was carried out for 24 h, 48 h and 72 h (Fig 4.1 a-c), to evaluate the cytotoxic effect of chemotherapy drug action. The graphs showed a decrease of Caco2 and HCT-116 cell viability in a dose-dependent manner after 24 h, 48 h, and 72 h. After 72h, Caco2 and HCT-116 cells treated with 5-FU at 200 µM showed about 24% and 22% of cell viability, respectively (Fig 4.1 c). In addition, the graphs showed an approximately 50% of cell viability in both cell lines, when they were treated with 5-FU at 10 µM, while a high rate of cell viability was observed at 0,1 µM and 1 µM of 5-FU in Caco2 and HCT-116 cells after 72 h of treatment (Fig 4.1 c). The treatments of several 5-FU concentrations highlighted a cytotoxic effect of the chemotherapy drug for both Caco2 and HCT-116 cells, as known in the literature (Filgueiras, Morrot et al. 2013). Then, treatments with NE-Curc alone were performed on Caco2 and HCT-116 cells for 24 h, 48 h, and 72 h, in order to detect the Curcumin action by considering two dilutions, as compared to the stock nanoemulsion (10% w_t of oil in water), 1:8 and 1:10 (v/w) (Fig. 4.1 d-f). A marked decrease of HCT-116 cells viability was observed at 24 h, 48 h, and 72 h of treatments with NE-Curc 1:8 and 1:10, unlike Caco2 cells in which a high rate of live cells was shown up to 72 h (Fig. 4.1 f). The high susceptibility of HCT-116 cells could be due to the selective cytotoxic action of Curcumin. For the following experiments, we used the dilution 1:8 of NE-Curc to investigate curcumin effects at a higher concentration than 1:10.

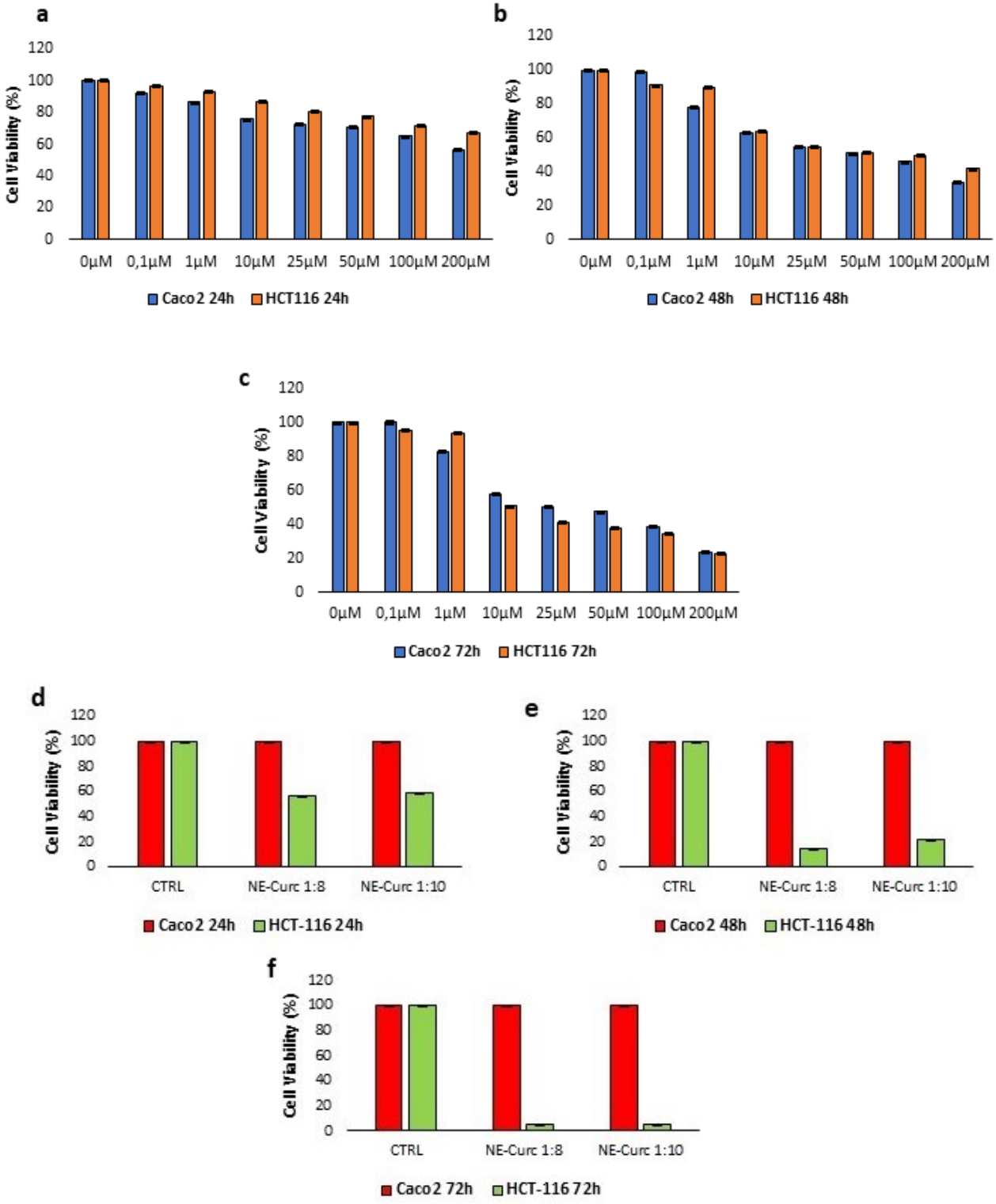

Figure 4.1 Treatments with 5-FU and NE-Curc on *in vitro* 2D cell culture after 24 h, 48 h, and 72 h. The graphs show the effect of 5-FU on *in vitro* 2D cell culture after 24 h (a), 48 h (b), and 72 h (c). Treatment with several concentrations of NE-Curc (1:8 and 1:10) on *in vitro* 2D cell cultures for 24h (d), 48h (e), and 72h (f); NE-Curc. All the experiments were performed in triplicate (n = 3), values represent the mean and the standard deviation (p ∗< 0.05; p ∗∗< 0.05).

4.3.2 Treatments with a combination of 5-FU and CT-NE-Curc on *in vitro* 2D cell culture models

The graphs (Fig.2 a-c) showed growing reduction of cell viability in both cell types when treated with 5-FU at 100 µM alone with 61% and 59% of mortality in Caco2 and HCT-116 cells respectively, at 72 h (Fig. 4.2 c), demonstrating the low cytotoxic selectivity of chemotherapy drug. Interestingly, when the cells were pre-treated with NE-Curc before the 5-FU treatment, as compared with the only treatment with 5-FU, a greater reduction of viability cell was observed in HCT-116 cells with a 79% of cancer cell deaths at 72h thanks to the expected adjuvant effect of curcumin. Instead, regarding the viability of Caco2 at 72 h, although preserved as compared to HCT-116 cells, which shows a selective effect promoted by the pretreatment with NE-Curc, it was only slightly higher than in the case of treatment with only 5-FU (Fig. 4.2 c), probably due to the relatively high concentration of 5-FU that didn't allow to observe the beneficial effect of Curcumin on healthy cells. Instead, a high rate of cell viability was displayed in Caco2 cells when they were treated with NE-Curc/cell medium, compared to HCT-116 cells (Fig. 4.2 a-c). The reason could be due to the selective action of Curcumin that inhibited the proliferation of HCT-116 cells since they are more metastatic and less differentiated colon cancer cells, compared with Caco2 cells, as known in the literature (Xiang, He et al. 2020).

In addition, a low concentration of 5-FU at 10 µM was also considered to observe the double-action of curcumin. The graphs of the MTT assay displayed high cell viability of HCT-116 cells compared to Caco2 cells, after 24 h of treatment with 5-FU at 10 µM alone (Fig. 4.3 a). However, after 48 h and 72 h a decrease of HCT-116 cell viability was detected, compared to a small viability increase of Caco2 cells (Fig. 4.3 b, c), observing a delayed effect of chemotherapy drug. After pre-treatment with NE-Curc and treatment with 5-FU at 10 µM a decrease of cell viability was observed in both Caco2 and HCT-116 cells with 50% and 60% of death rate respectively after 72 h (Fig. 4.3 c), compared to the treatment with 5-FU alone. Nevertheless, Caco2 cells survived slightly more than HCT116 cells after 48 h and 72 h (Fig. b, c). Moreover, the cell viability of Caco2 and HCT-116 cells between the NE-Curc/5-FU 10µM and NE-Curc/cell medium didn't change after 24 h (Fig. 4.3 a), but an increase of Caco2 cell viability compared to HCT-116 cells was observed after 48 h with 20% and 50% of mortality rate for Caco2 and HCT-116 cell respectively (Fig. b). A 10% decrease of Caco2 viability was observed in NE-Curc/cell medium after 72 h, while the HCT-116 cell viability was similar to that after 48h (Fig. 4.3 c).

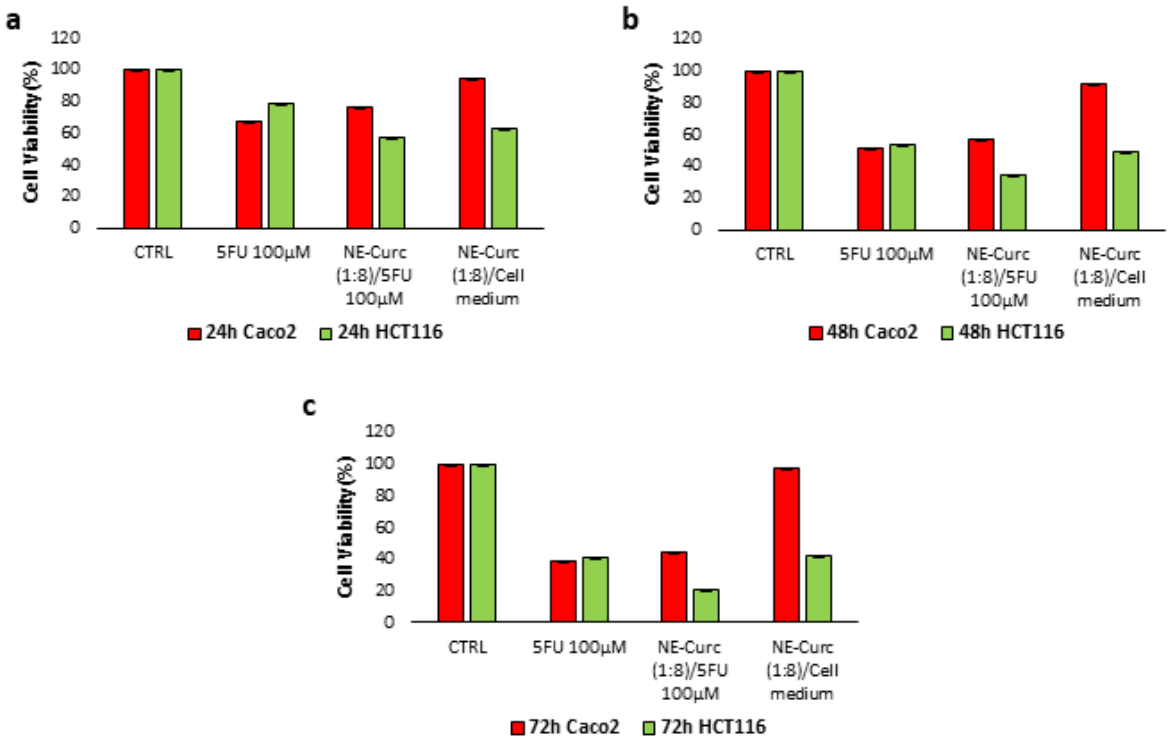

Figure 4.2 Cell Viability assay on *in vitro* 2D cell culture treated with combination NE-Curc (1:8) and 5-FU (100 µM). Pre-treated with NE-Curc (1:8) for 2h, washed and treated with 5-FU 100µM for 24h (a), 48h (b), 72h (c); NE-Curc, 5-FU, NE-Curc (1:8)/5-FU 10µM (Pre-treatment with NE-Curc and treatment with 5-FU), NE-Curc (1:8)/cell medium (Pre-treatment with NE-Curc and then addition cell medium). All the experiments were performed in triplicate (n = 3), values represent the mean and the standard deviation (g) (p ∗< 0.05; p ∗∗< 0.05).

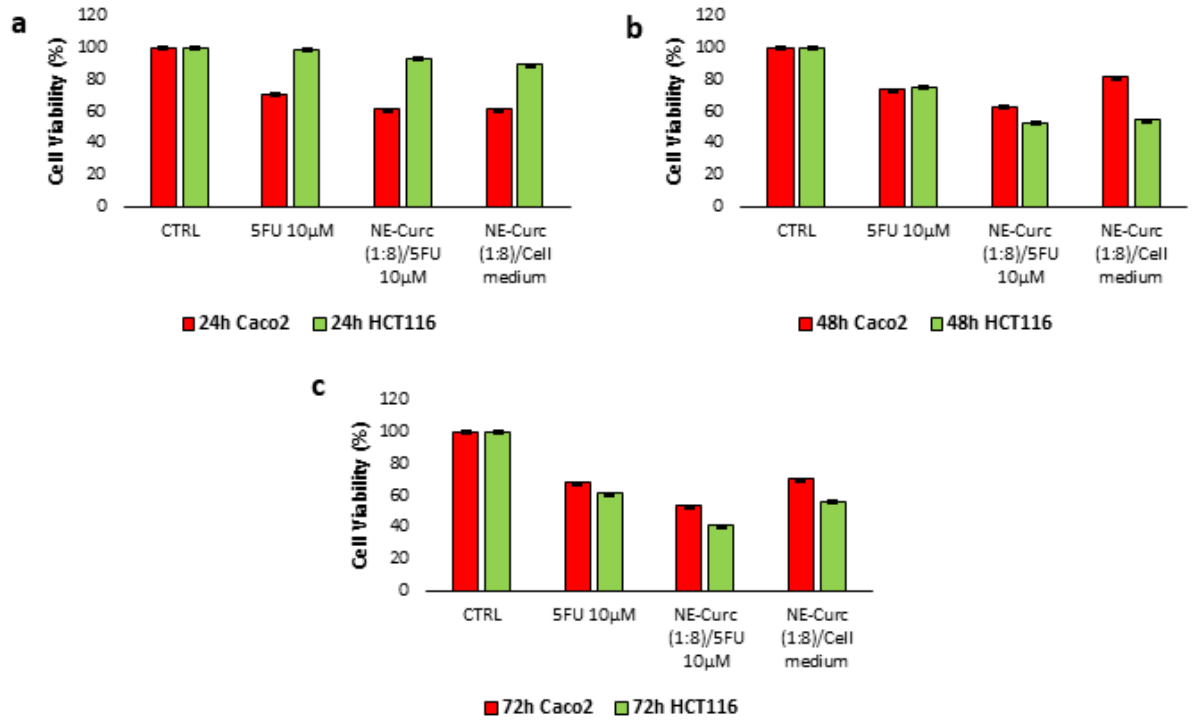

Figure 4.3 Cell Viability assay on *in vitro* 2D cell culture treated with combination NE-Curc (1:8) and 5-FU (10 µM). Pre-treated with NE-Curc (1:8) for 2h, washed and treated with 5-FU 10µM for 24h (a), 48h (b), 72h (c); NE-Curc, 5-FU, NE-Curc (1:8)/5-FU 10µM, NE-Curc (1:8)/cell medium. All the experiments were performed in triplicate (n = 3), values represent the mean and the standard deviation (g) (p ∗< 0.05; p ∗∗< 0.05).

5. Supplementary: Fabrication of *in vitro* 3D liver microtissue models

5.1 Introduction

In this supplementary, we describe the fabrication of different *in vitro* 3D Liver Tumor microtissue models 3D human hepatocellular carcinoma differentiated microtissues (3D HepG2 µTs); already established in the literature (Corrado, De Gregorio et al. 2019) and 3D human Primary hepatocellular carcinoma poorly-differentiated microtissues (3D HCC µTs), to compare the behavior of different 3D human liver cancer models and to use as potential 3D models for testing of drug candidates.

5.2 Materials and methods

5.2.1 Cell types

Hepatocellular carcinoma cell line (HepG2), with differentiated cells with epithelial-like phenotype, was purchased by ATCC and cultured in Minimum Essential Medium Earle's Salt (MEM, Biowest), containing 10% FBS, 200 mM L-Glutamine (Himedia), 100 IU ml $^{-1}$ Streptomycin/Penicillin (Himedia), 0.1mM Non-Essential Amino Acid and 0.1mM Sodium pyruvate. The seeding density was 12 500 cells/cm^2. HepG2 cells were sub-cultured every other Day thereafter using Trypsin/EDTA 0.05% (Himedia) and centrifuge at 1000 rpm for 5 min. The change of culture medium was every 2 Days.

Human Hepatocellular Carcinoma primary cells (HCC), poorly differentiated cells with mesenchymal cell phenotype (Nwosu, Battello et al. 2018), were provided by the Istituto Nazionale Tumori "Fondazione Pascale" (IRCCS). HCC cells were seeded onto a 0,1 % gelatin-coated plate and grown with Hepatocyte Culture Medium containing HBM^{TM} Basal Medium (CC-3199, Lonza) supplemented with HCM^{TM} SingleQuot Supplements (CC-4182, Lonza) and 20% FBS. The recommended seeding density for HCC cells was 20 000 cells/cm^2. Before cell seeding, a solution of 0,1 % gelatin (Euroclone) was loaded into a 6-multiwell plate (3 ml per well) and incubated at 37°C in a humidified atmosphere with 5% CO_2. Then, the gelatin solution excess was removed from the well plate and left for 2h under the hood at Room Temperature (RT). After that, a vial containing 300000 cells/ml was thawed and inoculated into the gelatin-coated 6-multiwell plate to allow the cell adhesion. A high concentration of FBS was used for the first 4-5 passages (20% FBS). The culture medium was changed after 48 h so that the most of cells have adhered. HCC cells were, then, sub-cultured every other day thereafter using Trypsin/EDTA 0.025% (CC-5012, Lonza) and centrifugation at 900 rpm for 5 min.

5.2.2 *In vitro* 3D Liver Tumor µTs fabrication

To reproduce the 3D Liver Tumor µTs, two types of 3D Liver Tumor µTs were realized:

- 3D Human Hepatocellular carcinoma differentiated microtissues (3D HepG2 µTs);
- 3D Human Primary Hepatocellular carcinoma poorly-differentiated microtissues (3D HCC µTs).

All 3D liver microtissues were produced in 6-well Clear Flat Bottom Ultra-Low Attachment Multiple Well Plates (Corning ® Costar ®), monitored and analyzed for different time points.

In vitro 3D Human Hepatocellular carcinoma differentiated microtissues (3D HepG2 µTs) production

HepG2 liver cells were cultured on GPMs in spinner flasks (Integra), as previously reported with slight modifications. Briefly, 35 mg of GPMs were loaded with 5.25×10^6 cells (30 cell/microbeads ratio). To promote cell seeding on microbeads an intermittent stirring regime (30 min at 0 rpm, 5min at 30 rpm) was applied for 24 h. Afterward, the stirring speed was kept at a continuous 20 rpm for up to 5-7 Days. The culture medium was changed three times per week. All cultures were maintained at 37°C in a humidified 5% CO_2 incubator and collected at 5-14 Days to characterize them.

In vitro 3D Human Primary Hepatocellular carcinoma poorly-differentiated microtissues (3D HCC µTs) production

HCC cells were seeded on GPMs through the use of a modified protocol in terms of cells density (Corrado, De Gregorio et al. 2019). In detail, two 3D mono-cultured HCC µTs (3D $_{mo}$HCC µTs) were produced with a different number of seeded cells: 20 cell/GPMs and 10 cell/GPMs ratio. Briefly, 25 mg of GMPs were loaded with 2,4 x 10^6 cells (20 cell/GPMs ratio) or 1,2 x 10^6 cells (10 cell/microbeads ratio) into 6-well Clear Flat Bottom Ultra-Low Attachment Multiple Well Plates (Corning ® Costar ®). To promote cell seeding on microbeads an intermittent stirring regime (30 min at 0 rpm, 5min at 30 rpm) was applied for 7 h. Then, an overnight static condition was applied in order to lead the cell adhesion within GPMs. Afterward, the stirring speed was kept at a continuous 30 rpm for up to 11 Days. Moreover, 3D co-cultured HCC µTs (3D $_{co}$HCC µTs) were realized following the same procedure of 3D CRC µTs, reported in section 2.2.1, considering the 10 cell/microbeads ratio and seeding HCC cells at Day 4 of culture. The samples were monitored, collected at Days 2, 4, 6, 8, 11, and were characterized using immunofluorescence staining and histological procedures.

5.2.3 Characterization of 3D Liver Tumor µTs

Encapsulation of 3D $_{mo}$HCC µTs with Alginate

Alginate solution was used to encapsulate 3D $_{mo}$HCC µTs. Alginate (2% w/v) was dissolved in H_2O using a Hot Plate and Magnetic Stirrer. In addition, a solution of Calcium Chloride at 0,1 M was prepared. Then, 3D $_{mo}$HCC µTs, previously fixed in PAF 4% and washed twice in PBS, were mixed with alginate at 2%, collected, and were dropped into the Calcium Chloride solution (drop by drop using a pipette) to obtain spheroids. In the end, microtissues encapsulated in alginate were picked up from Calcium Chloride using a surgical tweezer, placed into the tubes, and submerged in PBS 1X.

3D HCC µTs staining

For cell staining, 3D $_{mo}$HCC µTs and 3D $_{co}$HCC µTs were collected at different time points, washed twice with PBS, and then fixed with 4% PFA for 20 min. Following, the samples were incubated with the permeabilizing solution (PBS-Triton X-100 0.1%) for 10 min. After that, Phalloidin Red (Themofisher) diluted 1:1000 with PBS was used for 50 min. After SYTOX™ Green Nucleic Acid Stain diluted 1:10 000 was used for 10 min. The images were acquired using a Confocal Leica TCS SP5 II combined with a Multiphoton Microscope. The samples were observed using 488 nm Laser for Sytox Green Nucleic Acid Stain (λex/ λem= 504/523 nm), 543 nm Laser for Phalloidin Red (λex/ λem= 555/565 nm) and second harmonic generation (SHG) signal for collagen fibers and GPMs.

Histology of 3D HCC µTs and 3D HepG2 µTs on paraffin sections

As previously described in paragraph 2.2.4, 3D $_{mo}$HCC, 3D $_{co}$HCC µTs, and 3D HepG2 µTs were fixed in 4% PAF and dehydrated for Paraffin inclusion. For Hematoxylin/Eosin staining (Bio Optica W01030708) the sections were deparaffinized using xylene and hydrated in ethanol from 100% to 75%. After mounting with Histomount Mounting Solution (Bio Mount HM 05-BMHM500 Bio-Optica), 3D $_{mo}$HCC µTs, 3D $_{co}$HCC µTs, and 3D HepG2 µTs were observed with a light microscope (Olympus, BX53) to detect their morphological features.

5.3 Results and Discussions

5.3.1 Comparisons between 3D Liver Tumor µTs

Several 3D Liver microtissues were fabricated, characterized, and compared: 3D HepG2 µTs, 3D $_{mo}$HCC µTs and 3D HCC µTs. The H&E staining of HepG2 µTs showed the cell distribution over the GPMs surface at Day 5, 7, 10, and 14 (Fig. 5.1 a-d). The images depict a typical histotypic configuration and cytoarchitecture of normal hepatocytes characterized by a cuboidal cell shape with tight cell-cell contacts, as demonstrated in the literature (doi.org/10.3390/ijms222313135). However, the image (Fig. 5.1 d) showed a presence of a necrotic core at Day 14 of culture characterized by the breaking of cell-cell contacts (Fig. 5.1 d black arrows), suggesting that the quantity of oxygen and other nutrients transported into the inner regions of the spheroids, was not sufficient. Nevertheless this evidence, we demonstrated that 3D HepG2 µTs were able to grow and to stable until to Day 10 of culture and they could be used for the *in vitro* long-term culture, differently from the spheroids (Corrado, De Gregorio et al. 2019).

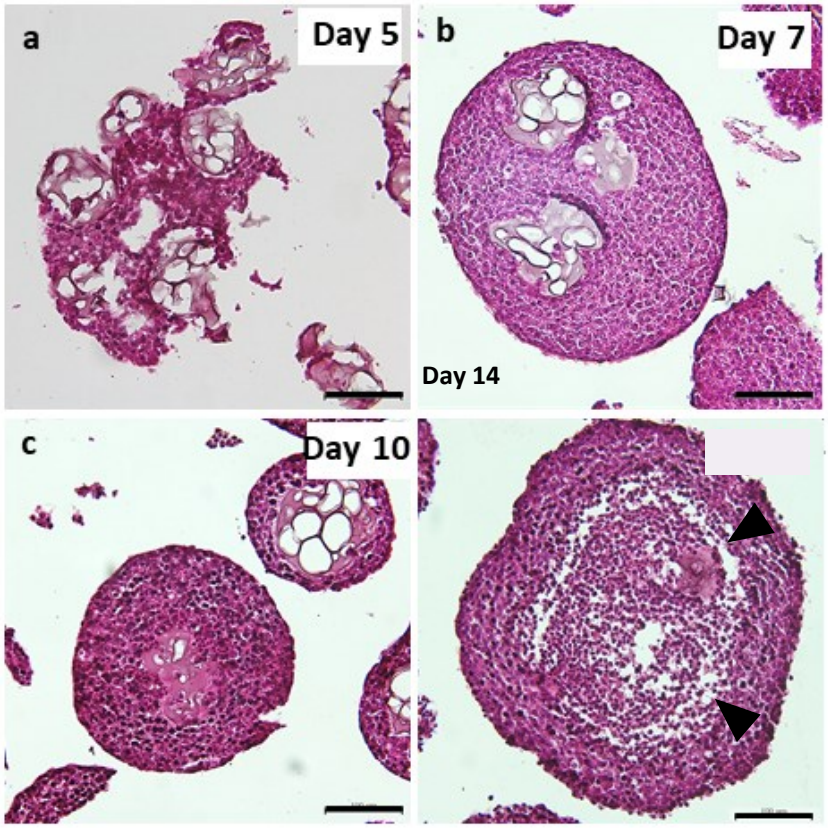

Figure 5.1 Characterization of 3D HepG2 µTs. Hematoxylin and eosin images of 3D HepG2 µTs at Day 5 (a), 7 (b), 10 (c) and 14 (d). Black arrows indicated the necrotic zone of 3D HepG2 µTs at Day 14 (b); scale bar 100 µm.

Two configurations of *in vitro* 3D $_{mo}$HCC µTs were realized with different cell density as follow: 20 cell/microbeads and 10 cell/microbeads. The brightfield images displayed a homogeneous distribution of 3D $_{mo}$HCC µTs 20 cell/microbeads in the first days of culture (Fig. 5.2 a, b) and large-scale of microtissues were present (Fig. 5.2 b). However, 3D $_{mo}$HCC µTs 20 cell/microbeads were disassembled at Day 6 of dynamic culture and several cell clusters came out from the microbeads (Fig. 5.1 c). It could be due to the high proliferation rate of HCC cells and the high cell density seeded. For this reason, 3D $_{mo}$HCC µTs with 10 cell/microbeads cell density was developed and the brightfield images showed a homogeneous distribution during microtissues production (Fig. 5.2 d-g). However, the 3D $_{mo}$HCC µTs with 10 cell/microbeads were not preserved until Day 11 of culture, due to the high rate of cell proliferation and an increase of microtissues size was exhibited with a diameter of 188 µm (Fig. 5.2 d-f, dotted red circles). Therefore, 3D $_{mo}$HCC µTs with 10 cell/microbeads cell density resulted better than 3D $_{mo}$HCC µTs with 20 cell/microbeads, as shown in table (Fig. 5.2 h).

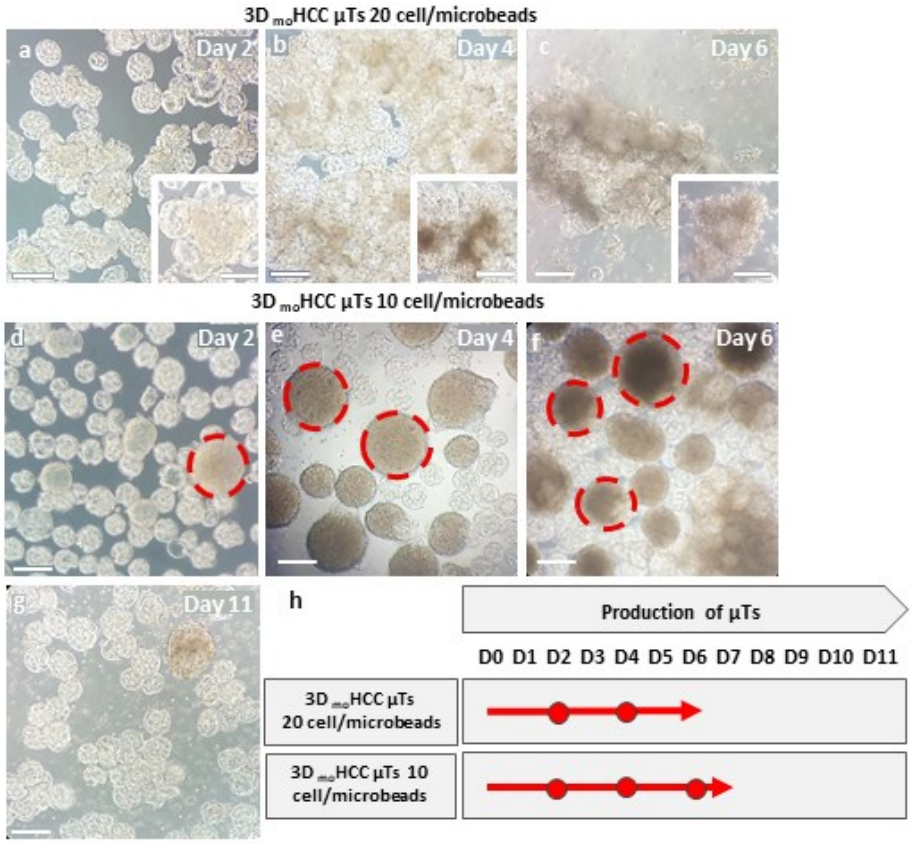

Figure 5.2 Production of *in vitro* 3D $_{mo}$HCC µTs with differents cell densities of HCC cells. 3D $_{mo}$HCC µTs in which were seeded 20 cells/microbeads at Day 0 and carried on until Day 6 (a-c); High magnification insets displayed some areas of 3D $_{mo}$HCC µTs 20 cell/microbeads; scale bar 140 µm. 3D $_{mo}$HCC µTs in which were seeded 10 cell/microbeads at Day 0 and carried on until Day 11 (d-g); Dotted red circles indicated the microtissues sizes; scale bar 140 µm. Table of microtissues production (h).

A deep characterization of microtissue produced at configuration selected was performed. In particular, a nuclear and actin filament staining of 3D $_{mo}$HCC µTs 10 cell/microbeads at Day 4, encapsulated in alginate, was achieved (Fig. 5.3 a). The images were acquired by using multiphoton imaging and second harmonic generation (SHG) displayed a well-organized and compact structure of 3D $_{mo}$HCC µTs 10 cell/microbeads and SHG signal was highlighted by the presence of gelatin microbeads that were in another frame of Z-stack acquisition (Fig. 5.3 b, white row). In addition, the histological cross-sections stained with H/E showed the organization and structure of 3D $_{mo}$HCC µTs 10 cell/microbeads at Day 4 (Fig. 5.3 c) with diameters around 90-200 µm, in which HCC cells were homogeneously spread over the surface of gelatin microbeads, acting as a scaffold (Fig. 5.3 d).

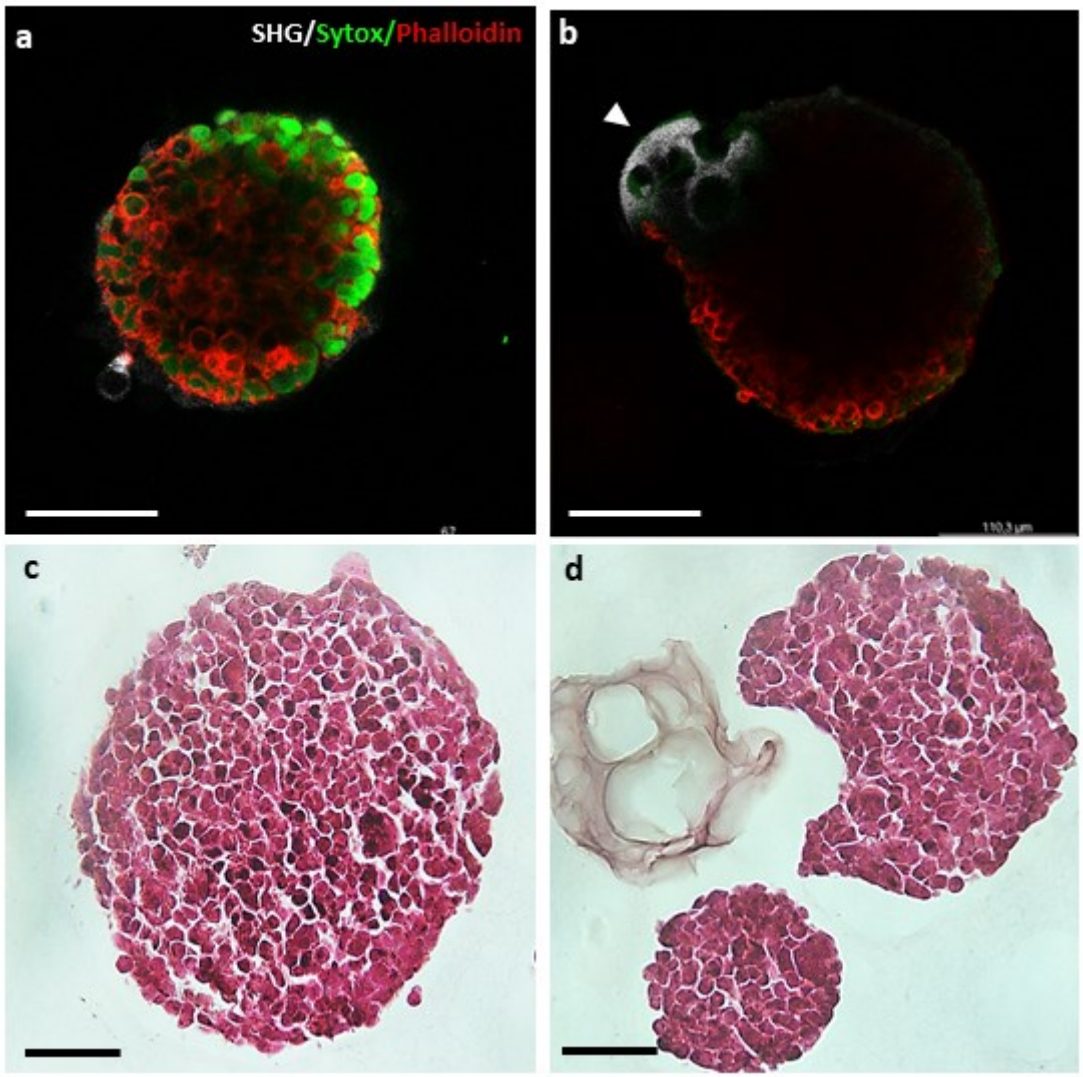

Figure 5.3 Characterization of 3D $_{mo}$HCC µTs 10 cell/microbeads at Day 4. Nuclear and actin filament staining were carried out by using Sytox green and Phalloidin red, respectively (a); a SHG signal of gelatin microbead was observed, indicated by a white row (b); scale bar 86 µm. Histological features of 3D $_{mo}$HCC µTs 10 cell/microbeads at Day 4 (b, c); scale bar 50 µm.

Fig. 5.4 showed that 3D $_{co}$HCC µTs resulted in a more compact structure on both Day 5 and Day 11 of culture. In detail, 3D $_{co}$HCC µTs were very thick with highly organized collagen fibers, produced by NF that extended from one microbead to another (Fig. 5.4 a, black arrows). In addition, $_{co}$HCC cells adhesion on the surface of the microbeads was observed (Fig. 5.4 a, high magnification inset). 3D $_{co}$HCC µTs showed the first signs of degradation at Day 11 of culture, probably due to the action of HCC cells that degrade the ECM to invade (Fig. 5.4 b). Moreover, images of the nuclear and actin filament staining acquired by using multiphoton imaging and SHG showed a homogeneous distribution of HCC cells into the surrounding ECM at Day 8 of culture and SHG signal coming from the collagen fibers (Fig. 5.4 c, white arrows). The histological cross-sections stained with H/E exhibited the HCC cell invasion into the complex and endogenous ECM (Fig. 5.4 d). In detail, a change of HCC cells from round to spindle shape (Fig. 5.4 d black arrows) was observed, due to the phenotypic transition from epithelial to mesenchymal that occurs during the cancer cell invasion into the surrounding ECM (Yamaguchi and Taouk 2020). In addition, NF were surrounded by the ECM and were highlighted with spindle and elongated shape (Fig. 5.4 d white arrows). Fig. 5.5 illustrates the Time evolution of several 3D Liver microtissues production. From this table, it was evident that the 3D $_{co}$HCC µTs configuration resulted better than 3D $_{mo}$HCC µTs 10 cell/beads, probably it could be due to the presence of ECM, capable to support the *in vitro* long-term culture. In addition, whereas 3D HepG2 µTs could be used to reproduce a 3D Liver tumor differentiated similar to normal phenotype, 3D HCC µTs could be used to reproduce a 3D Liver tumor model of Human Primary Hepatocellular carcinoma poorly-differentiated for the long-term culture.

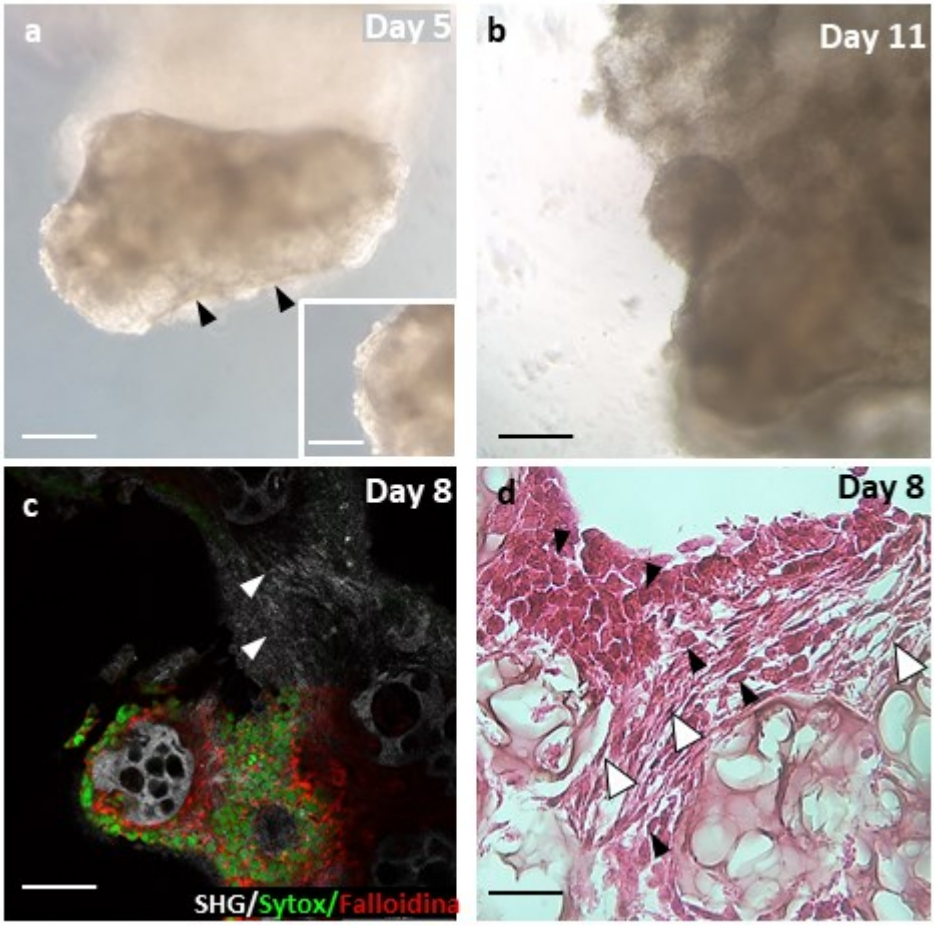

Figure 5.4 Characterization of 3D HCC µTs. Brightfield images of 3D coHCC µTs at Day 5 (a) and Day 11 (b) of culture, and the evidence of collagen fibers at Day 5 (black arrows); High magnification inset of 3D coHCC µTs at Day 5 showed the HCC cells adhesion on the microtissue; scale bar 140 µm. Nuclear and actin filament staining (sytox green and Phalloidin red, respectively) was carried out and the confocal images showed the HCC cells (green) embedded in an auto-produced ECM, highlighted by the SHG signal (white arrows); scale bar 155 µm. Histological features of 3D coHCC µTs displayed the HCC cell invasion (black arrows) into the ECM, and NF (white arrows); scale bar 50 µm.

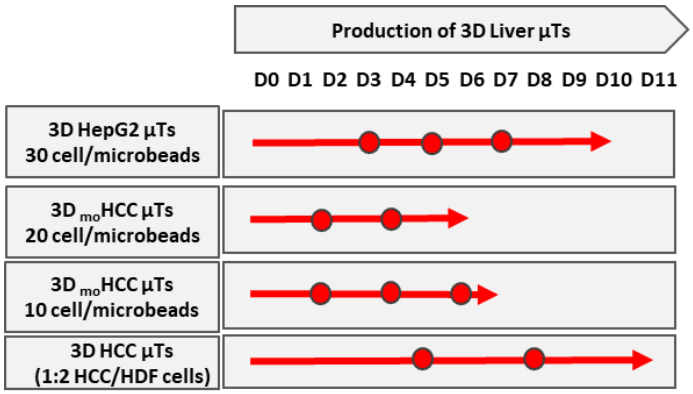

Figure 5.5 Production of several 3D Liver microtissues over time.

6. Conclusions and Future perspectives

In this work, we want to propose new 3D tumor microtissues of Colorectal cancer as potential models to be integrated into microfluidic platforms designed to simulate and investigate Colorectal cancer liver metastasis. At first, we focused on the fabrication of 3D Colorectal cancer microtissues (3D CRC µTs) exploring different process conditions and identifying the parameters that allow producing a 3D CRC µTs that better reproduce the tumor microenvironment, assessing in detail the difference in terms of cell growth, ECM deposition and ECM remodeling. We demonstrated that the configuration of 3D CRC µTs which proved the best one presented a tumor microenvironment that better resembled the *in vivo* counterpart. In addition, in these 3D CRC µTs we observed two relevant interactions between colon cancer cells and ECM: in particular, cancer cells interacted with ECM aligning along the collagen fibers direction to migrate and, at the same time, fibroblasts transformed in activated ones. After that, we used these 3D CRC µTs, as potential 3D tumor models, to investigate the coadjuvant action and the protective effect of curcumin-loaded nanoemulsions (CT-NE-Curc) in combination with 5-FU. The preliminary results of the treatments on *in vitro* 2D cell culture models seemed to not suggest a protective effect of the curcumin on cell viability of Caco2 cells, maybe potentially promoted by a cell environment that does not resemble the *in vivo* one. Whereas the treatments in 3D CRC µTs and 3D NF µTs showed that 5-FU alone and CT-NE-Curc/5-FU combinations seemed more selective in targeting the 3D CRC µTs compared with 3D NF µTs, suggesting that the penetration and diffusion of 5-FU alone and CT-NE-Curc/5-FU combinations was more immediate due to the continuous remodeling and changes of ECM in 3D CRC µTs by cancer cells and activated fibroblasts which degraded the surrounding tissue. Differently, the cell viability of 3D NF µTs was increased compared to 3D CRC µTs, probably due to more complex and intact ECM that allowed a slowing down of 5-FU alone and CT-NE-Curc/5-FU combinations penetration and diffusion. Therefore, the best formulation would seem a combination of CT-NE-Curc and 5-FU at a concentration to be searched in the range of 10 and 100 µM, since the cell viability of 3D NF µTs resulted in more than 50%, contrary to 3D CRC µTs after 72h of treatments. To assess the cell viability ratio between healthy and cancer cells, further analyses are ongoing to study how the ratio of healthy cells to cancer cells changes in the absence and the presence of curcumin at 10 and 100 µM of 5-FU to establish which formulation is the best one. Once we have chosen the best formulation, it will be used to investigate its effect on microfluidic platforms that simulate Colorectal cancer liver metastasis. In conclusion, these 3D tumor models could help to understand and chose the best treatment against CRC that, on one hand, improve the therapeutic efficacy selectively

targeting the cancer cells, and the other hand reduces the toxic effects of most chemotherapy drugs, thereby improving the quality of life for patients.

Then we investigated the metastatic process by designing a multi-organ microfluidic platform. Preliminary results of cancer cell migration and colonization towards the target organ were obtained using transwell inserts, accommodating 3D CRC µTs into the apical chamber and 3D HepG2 µTs – chosen since HepG2 cells retain "features characteristic of normal hepatocytes" (Arzumanian, Kiseleva et al. 2021) – into the basal chamber. From these promising results, we designed two potential devices – composed of two chambers separated, one to house the primary tumor (3D CRC µTs), and another to house the target organ (3D HepG2 µTs), respectively – to reproduce the metastatic process. The first series of experiments of cancer cell migration were carried out housing 3D CRC µTs in the primary tumor site of the first configuration of MET-on-a-chip device without 3D HepG2 µTs, then we added 3D HepG2 µTs in the target organ chamber of the second configuration of the device. The proposed MET-on-a-chip platforms allowed us to investigate the crucial bidirectional cross-talk between cancer cells and fibroblasts during cell invasion and migration in the primary tumor chamber. Even if the cancer cell migration from the primary tumor chamber towards the target organ chamber was not possible to monitor all time, however, we observed some cancer cells into the target organ chamber.

In conclusion, in Supplementary Chapter 5, it was shown the fabrication workflow and the comparison between different 3D Liver Tumor microtissues with a view to developing novel and potential models for drug/nutraceuticals testing.

In summary, we develop *in vitro* 3D CRC µTs that resemble the complex *in vivo* TME. However, we used fibroblasts derived from the different tissue not recapitulating faithfully the stromal compartment of colorectal cancer. For this reason, the next step is to consider the possibility to use primary intestinal fibroblasts to make these novel microtissues more similar to the *in vivo* microenvironment. Although other experiments need to be performed, the MET-on-a-chip devices open the way to reproduce the metastasis process and to resemble the *in vivo* condition in a more predictive way, aiming at using them for drug or nutraceuticals testing and high-throughput screening to improve the efficiency in translating new treatment options to clinical success. In addition, regarding the combination treatment with CT-NE-Curc and 5-FU, more tests will be needed to deepen the knowledge of this issue and to eventually test these combination treatments in MET-on-a-chip platforms to inhibit the cancer progression. In conclusion, Organ-on-a-chip technologies

demonstrate to be promising and powerful tools to reproduce human physiology and pathophysiology at the level of an organ/tissue or the whole organism offering new opportunities in multiple fields, while supporting replacement, reduction, and refinement of animal models and the paradigm of personalized medicine. In particular, the tumor-on-a-chip and metastasis-on-a-chip models are great and modern tools to simulate the crucial mechanisms underlying the cancer development and metastasis process to develop personalized treatments. Although these models still have a long way to go to implement them in daily clinical practice, currently, they have been obtaining many promising results in cancer research with the goal that one day they can be used in clinical applications so as to improve the success rate of the drug development process.

References

- Aceto, N., M. Toner, S. Maheswaran and D. A. Haber (2015). "En Route to Metastasis: Circulating Tumor Cell Clusters and Epithelial-to-Mesenchymal Transition." Trends in Cancer **1**(1): 44-52.
- Akhtar, R., S. Chandel, P. Sarotra and B. Medhi (2014). "Current status of pharmacological treatment of colorectal cancer." World Journal of Gastrointestinal Oncology **6**(6): 177-183.
- Albanese, A., A. K. Lam, E. A. Sykes, J. V. Rocheleau and W. C. W. Chan (2013). "Tumour-on-a-chip provides an optical window into nanoparticle tissue transport." Nature Communications **4**: 8.
- Albanese, A., A. K. Lam, E. A. Sykes, J. V. Rocheleau and W. C. W. Chan (2013). "Tumour-on-a-chip provides an optical window into nanoparticle tissue transport." Nature Communications **4**.
- Aleman, J. and A. Skardal (2019). "A multi-site metastasis-on-a-chip microphysiological system for assessing metastatic preference of cancer cells." Biotechnology and Bioengineering **116**(4): 936-944.
- Anand, P., A. B. Kunnumakkara, R. A. Newman and B. B. Aggarwal (2007). "Bioavailability of curcumin: Problems and promises." Molecular Pharmaceutics **4**(6): 807-818.
- Anggorowati, N., C. Ratna Kurniasari, K. Damayanti, T. Cahyanti, I. Widodo, A. Ghozali, M. M. Romi, D. C. R. Sari and N. Arfian (2017). "Histochemical and Immunohistochemical Study of α-SMA, Collagen, and PCNA in Epithelial Ovarian Neoplasm." Asian Pacific journal of cancer prevention : APJCP **18**(3): 667-671.
- Anguiano, M., C. Castilla, M. Maska, C. Ederra, R. Pelaez, X. Morales, G. Munoz-Arrieta, M. Mujika, M. Kozubek, A. Munoz-Barrutia, A. Rouzaut, S. Arana, J. M. Garcia-Aznar and C. Ortiz-de-Solorzano (2017). "Characterization of three-dimensional cancer cell migration in mixed collagen-Matrigel scaffolds using microfluidics and image analysis." Plos One **12**(2): 24.
- Arzumanian, V. A., O. I. Kiseleva and E. V. Poverennaya (2021). "The Curious Case of the HepG2 Cell Line: 40 Years of Expertise." International Journal of Molecular Sciences **22**(23).
- Ayres, C. E., B. S. Jha, H. Meredith, J. R. Bowman, G. L. Bowlin, S. C. Henderson and D. G. Simpson (2008). "Measuring fiber alignment in electrospun scaffolds: a user's guide to the 2D fast Fourier transform approach." Journal of Biomaterials Science-Polymer Edition **19**(5): 603-621.
- Ayuso, J. M., M. Virumbrates-Munoz, P. H. McMinn, S. Rehman, I. Gomez, M. R. Karim, R. Trusttchel, K. B. Wisinski, D. J. Beebe and M. C. Skala (2019). "Tumor-on-a-chip: a microfluidic model to study cell response to environmental gradients." Lab on a Chip **19**(20): 3461-3471.
- Begley, C. G. and L. M. Ellis (2012). "Raise standards for preclinical cancer research." Nature **483**(7391): 531-533.
- Bell, C. C., B. Chouhan, L. C. Andersson, H. Andersson, J. W. Dear, D. P. Williams and M. Soderberg (2020). "Functionality of primary hepatic non-parenchymal cells in a 3D spheroid model and contribution to acetaminophen hepatotoxicity." Archives of Toxicology **94**(4): 1251-1263.
- Benson, A. B., T. Bekaii-Saab, E. Chan, Y. J. Chen, M. A. Choti, H. S. Cooper, P. F. Engstrom, P. C. Enzinger, M. G. Fakih, M. J. Fenton, C. S. Fuchs, J. L. Grem, S. Hunt, A. Kamel, L. A. Leong, E. Lin, K. S. May, M. F. Mulcahy, K. Murphy, E. Rohren, D. P. Ryan, L. Saltz, S. Sharma, D. Shibata, J. M. Skibber, W. Small, C. T. Sofocleous, A. P. Venook, C. G. Willett, K. M. Gregory and D. A. Freedman-Cass (2013). "Metastatic Colon Cancer, Version 3.2013." Journal of the National Comprehensive Cancer Network **11**(2): 141-152.
- Bersini, S., J. S. Jeon, G. Dubini, C. Arrigoni, S. Chung, J. L. Charest, M. Moretti and R. D. Kamm (2014). "A microfluidic 3D in vitro model for specificity of breast cancer metastasis to bone." Biomaterials **35**(8): 2454-2461.
- Bhatia, S. N. and D. E. Ingber (2014). "Microfluidic organs-on-chips." Nature Biotechnology **32**(8): 760-772.
- Bissell, M. J. and D. Radisky (2001). "Putting tumours in context." Nature Reviews Cancer **1**(1): 46-54.
- Brancato, V., V. Comunanza, G. Imparato, D. Cora, F. Urciuolo, A. Noghero, F. Bussolino and P. A. Netti (2017). "Bioengineered tumoral microtissues recapitulate desmoplastic reaction of pancreatic cancer." Acta Biomaterialia **49**: 152-166.

- Brancato, V., F. Gioiella, G. Imparato, D. Guarnieri, F. Urciuolo and P. A. Netti (2018). "3D breast cancer microtissue reveals the role of tumor microenvironment on the transport and efficacy of free-doxorubicin in vitro." Acta Biomaterialia **75**: 200-212.
- Brancato, V., F. Gioiella, M. Profeta, G. Imparato, D. Guarnieri, F. Urciuolo, P. Melone and P. A. Netti (2017). "3D tumor microtissues as an in vitro testing platform for microenvironmentally-triggered drug delivery systems." Acta Biomaterialia **57**: 47-58.
- Buhrmann, C., P. Kraehe, C. Lueders, P. Shayan, A. Goel and M. Shakibaei (2014). "Curcumin Suppresses Crosstalk between Colon Cancer Stem Cells and Stromal Fibroblasts in the Tumor Microenvironment: Potential Role of EMT." Plos One **9**(9): 15.
- Carvalho, M. R., D. Barata, L. M. Teixeira, S. Giselbrecht, R. L. Reis, J. M. Oliveira, R. Truckenmuller and P. Habibovic (2019). "Colorectal tumor-on-a-chip system: A 3D tool for precision onco-nanomedicine." Science Advances **5**(5): 12.
- Cattin, S., L. Ramont and C. Ruegg (2018). "Characterization and In Vivo Validation of a Three-Dimensional Multi-Cellular Culture Model to Study Heterotypic Interactions in Colorectal Cancer Cell Growth, Invasion and Metastasis." Frontiers in Bioengineering and Biotechnology **6**: 14.
- Choi, Y., E. Hyun, J. Seo, C. Blundell, H. C. Kim, E. Lee, S. H. Lee, A. Moon, W. K. Moon and D. Huh (2015). "A microengineered pathophysiological model of early-stage breast cancer." Lab on a Chip **15**(16): 3350-3357.
- Chung, M., J. Ahn, K. Son, S. Kim and N. L. Jeon (2017). "Biomimetic Model of Tumor Microenvironment on Microfluidic Platform." Advanced Healthcare Materials **6**(15): 7.
- Corrado, B., V. De Gregorio, G. Imparato, C. Attanasio, F. Urciuolo and P. A. Netti (2019). "A three-dimensional microfluidized liver system to assess hepatic drug metabolism and hepatotoxicity." Biotechnology and Bioengineering **116**(5): 1152-1163.
- De Angelis, P. M., D. H. Svendsrud, K. L. Kravik and T. Stokke (2006). "Cellular response to 5-fluorouracil (5-FU) in 5-FU-resistant colon cancer cell lines during treatment and recovery." Molecular Cancer **5**: 25.
- de la Rosa, J. M. R., J. Wubetu, N. Tirelli and A. Tirella (2018). "Colorectal tumor 3D in vitro models: advantages of biofabrication for the recapitulation of early stages of tumour development." Biomedical Physics & Engineering Express **4**(4): 12.
- Despotovic, S. Z., D. N. Milkcvic, A. J. Krmpot, A. M. Pavlovic, V. D. Zivanovic, Z. Krivokapic, V. B. Pavlovic, S. Levic, G. Nikolic and M. D. Rabasovic (2020). "Altered organization of collagen fibers in the uninvolved human colon mucosa 10 cm and 20 cm away from the malignant tumor." Scientific Reports **10**(1): 11.
- Domansky, K., W. Inman, J. Serdy, A. Dash, M. H. M. Lim and L. G. Griffith (2010). "Perfused multiwell plate for 3D liver tissue engineering." Lab on a Chip **10**(1): 51-58.
- Driesen, R. B., P. Hilkens, N. Smisdom, T. Vangansewinkel, Y. Dillen, J. Ratajczak, E. Wolfs, P. Gervois, M. Ameloot, A. Bronckaers and I. Lambrichts (2020). "Dental Tissue and Stem Cells Revisited: New Insights From the Expression of Fibroblast Activation Protein-Alpha." Frontiers in Cell and Developmental Biology **7**: 10.
- Ehsan, S. M., K. M. Welch-Reardon, M. L. Waterman, C. C. W. Hughes and S. C. George (2014). "A three-dimensional in vitro model of tumor cell intravasation." Integrative Biology **6**(6): 603-610.
- Esch, E. W., A. Bahinski and D. Huh (2015). "Organs-on-chips at the frontiers of drug discovery." Nature Reviews Drug Discovery **14**(4): 248-260.
- Filgueiras, M. d. C., A. Morrot, P. M. Gomes Soares, M. L. Costa and C. Mermelstein (2013). "Effects of 5-Fluorouracil in Nuclear and Cellular Morphology, Proliferation, Cell Cycle, Apoptosis, Cytoskeletal and Caveolar Distribution in Primary Cultures of Smooth Muscle Cells." Plos One **8**(4).
- Fu, X., Y. N. He, M. Li, Z. Z. Huang and M. Najafi (2021). "Targeting of the tumor microenvironment by curcumin." Biofactors **47**(6): 914-932.
- Gentile, S. D., A. P. Kourouklis, H. Ryoo and G. H. Underhill (2020). "Integration of Hydrogel Microparticles With Three-Dimensional Liver Progenitor Cell Spheroids." Frontiers in Bioengineering and Biotechnology **8**: 10.

- Gialeli, C., A. D. Theocharis and N. K. Karamanos (2011). "Roles of matrix metalloproteinases in cancer progression and their pharmacological targeting." Febs Journal **278**(1): 16-27.
- Gioiella, F., F. Urciuolo, G. Imparato, V. Brancato and P. A. Netti (2016). "An Engineered Breast Cancer Model on a Chip to Replicate ECM-Activation In Vitro during Tumor Progression." Advanced Healthcare Materials **5**(23): 3074-3084.
- Gong, L. Q., Q. Yan, Y. Thang, X. N. Fang, B. L. Liu and X. Y. Guan (2019). "Cancer cell reprogramming: a promising therapy converting malignancy to benignity." Cancer Communications **39**(1): 13.
- Gorelik, R. and A. Gautreau (2014). "Quantitative and unbiased analysis of directional persistence in cell migration." Nature Protocols **9**(8): 1931-1943.
- Goulet, C. R., G. Bernard, S. Tremblay, S. Chabaud, S. Bolduc and F. Pouliot (2018). "Exosomes Induce Fibroblast Differentiation into Cancer-Associated Fibroblasts through TGF beta Signaling." Molecular Cancer Research **16**(7): 1196-1204.
- Han, C. C., T. Y. Liu and R. Yin (2020). "Biomarkers for cancer-associated fibroblasts." Biomarker Research **8**(1): 8.
- Hassell, B. A., G. Goyal, E. Lee, A. Sontheimer-Phelps, O. Levy, C. S. Chen and D. E. Ingber (2017). "Human Organ Chip Models Recapitulate Orthotopic Lung Cancer Growth, Therapeutic Responses, and Tumor Dormancy In Vitro." Cell Reports **21**(2): 508-516.
- Huh, D., B. D. Matthews, A. Mammoto, M. Montoya-Zavala, H. Y. Hsin and D. E. Ingber (2010). "Reconstituting Organ-Level Lung Functions on a Chip." Science **328**(5986): 1662-1668.
- Huo, K. G., E. D'Arcangelo and M. S. Tsao (2020). "Patient-derived cell line, xenograft and organoid models in lung cancer therapy." Translational Lung Cancer Research **9**(5): 2214-2232.
- Hurtado, P., I. Martinez-Pena and R. Pineiro (2020). "Dangerous Liaisons: Circulating Tumor Cells (CTCs) and Cancer-Associated Fibroblasts (CAFs)." Cancers **12**(10): 23.
- Ieda, T., H. Tazawa, H. Okabayashi, S. Yano, K. Shigeyasu, S. Kuroda, T. Ohara, K. Noma, H. Kishimoto, M. Nishizaki, S. Kagawa, Y. Shirakawa, T. Saitou, T. Imamura and T. Fujiwara (2019). "Visualization of epithelial-mesenchymal transition in an inflammatory microenvironment-colorectal cancer network." Scientific Reports **9**: 11.
- Imamura, Y., T. Mukohara, Y. Shimono, Y. Funakoshi, N. Chayahara, M. Toyoda, N. Kiyota, S. Takao, S. Kono, T. Nakatsura and H. Minami (2015). "Comparison of 2D-and 3D-culture models as drug-testing platforms in breast cancer." Oncology Reports **33**(4): 1837-1843.
- Imparato, G., F. Urciuolo and P. A. Netti (2022). "Organ on Chip Technology to Model Cancer Growth and Metastasis." Bioengineering-Basel **9**(1): 24.
- Jonsson, A., C. Hjalmarsson, P. Falk and M. L. Ivarsson (2018). "Stability of matrix metalloproteinase-9 as biological marker in colorectal cancer." Medical Oncology **35**(4): 6.
- Justus, C. R., N. Leffler, M. Ruiz-Echevarria and L. V. Yang (2014). "In vitro Cell Migration and Invasion Assays." Jove-Journal of Visualized Experiments(88).
- Khazali, A. S., A. M. Clark and A. Wells (2017). "A Pathway to Personalizing Therapy for Metastases Using Liver-on-a-Chip Platforms." Stem Cell Reviews and Reports **13**(3): 364-380.
- Khurana, R. K., A. Jain, A. Jain, T. Sharma, B. Singh and P. Kesharwani (2018). "Administration of antioxidants in cancer: debate of the decade." Drug Discovery Today **23**(4): 763-770.
- Kow, A. W. C. (2019). "Hepatic metastasis from colorectal cancer." Journal of Gastrointestinal Oncology **10**(6): 1274-1298.
- Langella, A., V. Calcagno, V. De Gregorio, F. Urciuolo, G. Imparato, R. Vecchione and P. A. Netti (2018). "In vitro study of intestinal epithelial interaction with engineered oil in water nanoemulsions conveying curcumin." Colloids and Surfaces B-Biointerfaces **164**: 232-239.
- Lee-Montiel, F. T., S. M. George, A. H. Gough, A. D. Sharma, J. F. Wu, R. DeBiasio, L. A. Vernetti and D. L. Taylor (2017). "Control of oxygen tension recapitulates zone-specific functions in human liver microphysiology systems." Experimental Biology and Medicine **242**(16): 1617-1632.
- Lee, S. J., J. H. Jeong, I. H. Lee, J. Lee, J. H. Jung, H. Y. Park, D. H. Lee and Y. S. Chae (2019). "Effect of High-dose Vitamin C Combined With Anti-cancer Treatment on Breast Cancer Cells." Anticancer Research **39**(2): 751-758.

- Liu, L., L. Liu, H. H. Yao, Z. Q. Zhu, Z. L. Ning and Q. Huang (2016). "Stromal Myofibroblasts Are Associated with Poor Prognosis in Solid Cancers: A Meta-Analysis of Published Studies." Plos One **11**(7).
- Liu, Q., H. F. Zhang, X. L. Jiang, C. Y. Qian, Z. Q. Liu and D. Y. Luo (2017). "Factors involved in cancer metastasis: a better understanding to "seed and soil" hypothesis." Molecular Cancer **16**: 19.
- Liu, Z. J., P. Y. Huang, S. K. Law, H. Y. Tian, W. N. Leung and C. S. Xu (2018). "Preventive Effect of Curcumin Against Chemotherapy-Induced Side-Effects." Frontiers in Pharmacology **9**: 9.
- Longley, D. B., D. P. Harkin and P. G. Johnston (2003). "5-Fluorouracil: Mechanisms of action and clinical strategies." Nature Reviews Cancer **3**(5): 330-338.
- Luo, J. J., C. D. Young, H. M. Zhou and X. J. Wang (2018). "Mouse Models for Studying Oral Cancer: Impact in the Era of Cancer Immunotherapy." Journal of Dental Research **97**(6): 683-690.
- Massague, J. and A. C. Obenauf (2016). "Metastatic colonization by circulating tumour cells." Nature **529**(7586): 298-306.
- Motoyama, W., K. Sayo, H. Mihara, S. Aoki and N. Kojima (2016). "Induction of hepatic tissues in multicellular spheroids composed of murine fetal hepatic cells and embedded hydrogel beads." Regenerative Therapy **3**: 7-10.
- Nwosu, Z. C., N. Battello, M. Rothley, W. Pioronska, B. Sitek, M. P. Ebert, U. Hofmann, J. Sleeman, S. Woelfl, C. Meyer, D. A. Megger and S. Dooley (2018). "Liver cancer cell lines distinctly mimic the metabolic gene expression pattern of the corresponding human tumours." Journal of Experimental & Clinical Cancer Research **37**.
- Olgen, S. (2018). "Overview on Anticancer Drug Design and Development." Current Medicinal Chemistry **25**(15): 1704-1719.
- Orang, A. V., J. Petersen, R. A. McKinnon and M. Z. Michael (2019). "Micromanaging aerobic respiration and glycolysis in cancer cells." Molecular Metabolism **23**: 98-126.
- Paget, S. (1889). "THE DISTRIBUTION OF SECONDARY GROWTHS IN CANCER OF THE BREAST." The Lancet **133**(3421): 571-573.
- Park, J. I., J. Lee, J. L. Kwon, H. B. Park, S. Y. Lee, J. Y. Kim, J. Sung, J. M. Kim, K. S. Song and K. H. Kim (2016). "Scaffold-Free Coculture Spheroids of Human Colonic Adenocarcinoma Cells and Normal Colonic Fibroblasts Promote Tumorigenicity in Nude Mice." Translational Oncology **9**(1): 79-88.
- Phillips, C. L., S. B. Combs and S. R. Pinnell (1994). "EFFECTS OF ASCORBIC-ACID ON PROLIFERATION AND COLLAGEN-SYNTHESIS IN RELATION TO THE DONOR AGE OF HUMAN DERMAL FIBROBLASTS." Journal of Investigative Dermatology **103**(2): 228-232.
- Picollet-D'hahan, N., A. Zuchowska, I. Lemeunier and S. Le Gac (2021). "Multiorgan-on-a-Chip: A Systemic Approach To Model and Decipher Inter-Organ Communication." Trends in Biotechnology **39**(8): 788-810.
- Pin, A. L., F. Houle and J. Huot (2011). "Recent Advances in Colorectal Cancer Research: The Microenvironment Impact." Cancer Microenvironment **4**(2): 127-131.
- Ribatti, D., R. Tamma and T. Annese (2020). "Epithelial-Mesenchymal Transition in Cancer: A Historical Overview." Translational Oncology **13**(6): 9.
- Ruiz-Espigares, J., D. Nieto, L. Moroni, G. Jimenez and J. A. Marchal (2021). "Evolution of Metastasis Study Models toward Metastasis-On-A-Chip: The Ultimate Model?" Small **17**(14): 18.
- Said, A. H., J. P. Raufman and G. F. Xie (2014). "The Role of Matrix Metalloproteinases in Colorectal Cancer." Cancers **6**(1): 366-375.
- Sara, J. D., J. Kaur, R. Khodadadi, M. Rehman, R. Lobo, S. Chakrabarti, J. Herrmann, A. Lerman and A. Grothey (2018). "5-fluorouracil and cardiotoxicity: a review." Therapeutic Advances in Medical Oncology **10**: 18.
- Scognamiglio, L. S. (2020). A novel bioengineered cystic fibrosis model. Ph.D, University of Naples "Federico II".
- Selmeczi, D., S. Mosler, P. H. Hagedorn, N. B. Larsen and H. Flyvbjerg (2005). "Cell motility as persistent random motion: Theories from experiments." Biophysical Journal **89**(2): 912-931.

- Shakibaei, M., P. Kraehe, B. Popper, P. Shayan, A. Goel and C. Buhrmann (2015). "Curcumin potentiates antitumor activity of 5-fluorouracil in a 3D alginate tumor microenvironment of colorectal cancer." Bmc Cancer **15**: 15.
- Shakibaei, M., A. Mobasheri, C. Lueders, F. Busch, P. Shayan and A. Goel (2013). "Curcumin Enhances the Effect of Chemotherapy against Colorectal Cancer Cells by Inhibition of NF-kappa B and Src Protein Kinase Signaling Pathways." Plos One **8**(2): 13.
- Sharifi, F., O. Yesil-Celiktas, A. Kazan, S. Maharjan, S. Saghazadeh, K. Firoozbakhsh, B. Firoozabadi and Y. S. Zhang (2020). "A hepatocellular carcinoma-bone metastasis-on-a-chip model for studying thymoquinone-loaded anticancer nanoparticles." Bio-Design and Manufacturing **3**(3): 189-202.
- Shen, T., Y. Li, S. Zhu, J. Yu, B. Zhang, X. Chen, Z. Zhang, Y. Ma, Y. Niu and Z. Shang (2020). "YAP1 plays a key role of the conversion of normal fibroblasts into cancer-associated fibroblasts that contribute to prostate cancer progression." Journal of Experimental & Clinical Cancer Research **39**(1).
- Shin, Y., S. Han, E. Chung and S. Chung (2014). "Intratumoral phenotypic heterogeneity as an encourager of cancer invasion." Integrative Biology **6**(7): 654-661.
- Shin, Y., H. Kim, S. Han, J. Won, H. E. Jeong, E. S. Lee, R. D. Kamm, J. H. Kim and S. Chung (2013). "Extracellular Matrix Heterogeneity Regulates Three-Dimensional Morphologies of Breast Adenocarcinoma Cell Invasion." Advanced Healthcare Materials **2**(6): 790-794.
- Skardal, A., M. Devarasetty, S. Forsythe, A. Atala and S. Soker (2016). "A Reductionist Metastasis-on-a-Chip Platform for In Vitro Tumor Progression Modeling and Drug Screening." Biotechnology and Bioengineering **113**(9): 2020-2032.
- Somarelli, J. A., A. M. Boddy, H. L. Gardner, S. B. DeWitt, J. Tuohy, K. Megquier, M. U. Sheth, S. D. Hsu, J. L. Thorne, C. A. London and W. C. Eward (2020). "Improving Cancer Drug Discovery by Studying Cancer across the Tree of Life." Molecular Biology and Evolution **37**(1): 11-17.
- Sontheimer-Phelps, A., B. A. Hassell and D. E. Ingber (2019). "Modelling cancer in microfluidic human organs-on-chips." Nature Reviews Cancer **19**(2): 65-81.
- Strelez, C., S. Chilakala, K. Ghaffarian, R. Lau, E. Spiller, N. Ung, D. Hixon, A. Y. Yoon, R. X. Sun, H. J. Lenz, J. E. Katz and S. M. Mumenthaler (2021). "Human colorectal cancer-on-chip model to study the microenvironmental influence on early metastatic spread." Iscience **24**(5): 23.
- Suetsugu, T., R. Mori, M. Futamura, M. Fukada, H. Tanaka, I. Yasufuku, Y. Sato, Y. Iwata, T. Imai, H. Imai, Y. Tanaka, N. Okumura, N. Matsuhashi, T. Takahashi and K. Yoshida (2021). "Mechanism of acquired 5FU resistance and strategy for overcoming 5FU resistance focusing on 5FU metabolism in colon cancer cell lines." Oncology Reports **45**(4): 8.
- Sung, K. E., N. Yang, C. Pehlke, P. J. Keely, K. W. Eliceiri, A. Friedl and D. J. Beebe (2011). "Transition to invasion in breast cancer: a microfluidic in vitro model enables examination of spatial and temporal effects." Integrative Biology **3**(4): 439-450.
- Taufalele, P. V., J. A. Vanderburgh, A. Munoz, M. R. Zanotelli and C. A. Reinhart-King (2019). "Fiber alignment drives changes in architectural and mechanical features in collagen matrices." Plos One **14**(5).
- Truong, D., J. Puleo, A. Llave, G. Mouneimne, R. D. Kamm and M. Nikkhah (2016). "Breast Cancer Cell Invasion into a Three Dimensional Tumor-Stroma Microenvironment." Scientific Reports **6**: 18.
- Tsai, H. F., A. Trubelja, A. Q. Shen and G. Bao (2017). "Tumour-on-a-chip: microfluidic models of tumour morphology, growth and microenvironment." Journal of the Royal Society Interface **14**(131): 20.
- Valderrama-Trevino, A. I., B. Barrera-Mera, J. C. Ceballos-Villalva and E. E. Montalvo-Jave (2017). "Hepatic Metastasis from Colorectal Cancer." Euroasian journal of hepato-gastroenterology **7**(2): 166-175.
- Vecchione, R., V. Quagliariello, D. Calabria, V. Calcagno, E. De Luca, R. V. Iaffaioli and P. A. Netti (2016). "Curcumin bioavailability from oil in water nano-emulsions: In vitro and in vivo study on the dimensional, compositional and interactional dependence." Journal of Controlled Release **233**: 88-100.

- Vernetti, L. A., N. Senutovitch, R. Boltz, R. DeBiasio, T. Y. Shun, A. Gough and D. L. Taylor (2016). "A human liver microphysiology platform for investigating physiology, drug safety, and disease models." Experimental Biology and Medicine **241**(1): 101-114.
- Vodenkova, S., T. Buchler, K. Cervena, V. Veskrnova, P. Vodicka and V. Vymetalkova (2020). "5-fluorouracil and other fluoropyrimidines in colorectal cancer: Past, present and future." Pharmacology & Therapeutics **206**: 19.
- Walker, G. M., J. Q. Sai, A. Richmond, M. Stremler, C. Y. Chung and J. P. Wikswo (2005). "Effects of flow and diffusion on chemotaxis studies in a microfabricated gradient generator." Lab on a Chip **5**(6): 611-618.
- Wang, Y. M., D. Wu, G. H. Wu, J. G. Wu, S. M. Lu, J. Lo, Y. He, C. Zhao, X. Zhao, H. B. Zhang and S. Q. Wang (2020). "Metastasis-on-a-chip mimicking the progression of kidney cancer in the liver for predicting treatment efficacy." Theranostics **10**(1): 300-311.
- Wei, Y. M., P. J. Yang, S. S. Cao and L. Zhao (2018). "The combination of curcumin and 5-fluorouracil in cancer therapy." Archives of Pharmacal Research **41**(1): 1-13.
- Winkler, J., A. Abisoye-Ogunniyan, K. J. Metcalf and Z. Werb (2020). "Concepts of extracellular matrix remodelling in tumour progression and metastasis." Nature Communications **11**(1): 19.
- Wu, F., J. Yang, J. Liu, Y. Wang, J. Mu, Q. Zeng, S. Deng and H. Zhou (2021). "Signaling pathways in cancer-associated fibroblasts and targeted therapy for cancer." Signal Transduction and Targeted Therapy **6**(1).
- Wu, J.-s., J. Jiang, B.-j. Chen, K. Wang, Y.-l. Tang and X.-h. Liang (2021). "Plasticity of cancer cell invasion: Patterns and mechanisms." Translational Oncology **14**(1).
- Wu, M. M. and M. A. Swartz (2014). "Modeling Tumor Microenvironments In Vitro." Journal of Biomechanical Engineering-Transactions of the Asme **136**(2): 7.
- Wu, Q., Z. P. Yang, Y. Z. Nie, Y. Q. Shi and D. M. Fan (2014). "Multi-drug resistance in cancer chemotherapeutics: Mechanisms and lab approaches." Cancer Letters **347**(2): 159-166.
- Xiang, L., B. He, Q. Liu, D. Hu, W. Liao, R. Li, X. Peng, Q. Wang and G. Zhao (2020). "Antitumor effects of curcumin on the proliferation, migration and apoptosis of human colorectal carcinoma HCT-116 cells." Oncology Reports **44**(5): 1997-2008.
- Xu, Q. Q. (2021). "Human Three-Dimensional Hepatic Models: Cell Type Variety and Corresponding Applications." Frontiers in Bioengineering and Biotechnology **9**: 21.
- Yamaguchi, H. and G. M. Taouk (2020). "A Potential Role of YAP/TAZ in the Interplay Between Metastasis and Metabolic Alterations." Frontiers in Oncology **10**.
- Yang, X. G., Y. L. Lin, Y. H. Shi, B. J. Li, W. R. Liu, W. Yin, Y. J. Dang, Y. W. Chu, J. Fan and R. He (2016). "FAP Promotes Immunosuppression by Cancer-Associated Fibroblasts in the Tumor Microenvironment via STAT3-CCL2 Signaling." Cancer Research **76**(14): 4124-4135.
- Yi, H. G., Y. H. Jeong, Y. Kim, Y. J. Choi, H. E. Moon, S. H. Park, K. S. Kang, M. Bae, J. Jang, H. Youn, S. H. Paek and D. W. Cho (2019). "A bioprinted human-glioblastoma-on-a-chip for the identification of patient-specific responses to chemoradiotherapy." Nature Biomedical Engineering **3**(7): 509-519.
- Yuan, Z. M., H. Q. Hu, Y. H. Zhu, W. Y. Zhang, Q. X. Fang, T. Y. Qiao, T. Y. Ma, M. Wang, R. Huang, Q. C. Tang, F. Gao, C. X. Zou, X. Gao, G. Y. Wang and X. S. Wang (2021). "Colorectal cancer cell intrinsic fibroblast activation protein alpha binds to Enolase1 and activates NF-kappa B pathway to promote metastasis." Cell Death & Disease **12**(6): 15.
- Zhao, B., X. Wei, W. Li, R. S. Udan, Q. Yang, J. Kim, J. Xie, T. Ikenoue, J. Yu, L. Li, P. Zheng, K. Ye, A. Chinnaiyan, G. Halder, Z.-C. Lai and K.-L. Guan (2007). "Inactivation of YAP oncoprotein by the Hippo pathway is involved in cell contact inhibition and tissue growth control." Genes & Development **21**(21): 2747-2761.